PERIDYNAMIC AND DISCRETE MULTIPHYSICS FOR MODELLING THE MECHANICAL AND FRACTURE PROPERTIES OF PAVEMENT MATERIALS

by

DANILO SANFILIPPO

A thesis submitted to the University of Birmingham for the degree of

DOCTOR OF PHILOSOPHY

School of Chemical Engineering
College of Engineering and Physical Sciences
University of Birmingham
August 2022

Abstract

Asphalt pavement experiences different degradation mechanisms under several solicitations. The asphalt mechanical and fracture properties of asphalt mixtures have been investigated using experiment and X-ray CT scan to improve the quality of design. These methods are limited by the number of samples required and high cost. The development of numerical methods provided a powerful tool to investigate the asphalt mixture performance at macro and micro scale, requiring lower number of sample and cost. A key challenge of the numerical method is the reliable modelling of the cracks under different conditions.

In this thesis, Peridynamics and Discrete Multiphysics model is used to simulate the mechanical properties and fracture characteristics of pavement materials. The simulations were carried out on the open-source software LAMMPS and visualised on Ovito. Initially, the capability of Peridynamics and Discrete Multiphysics was explored to assess micro-crack formation and propagation in asphalt mixture at low temperatures and under freezing conditions. The results showed the cracks form at the interface and propagate from one void to another along the direction of load. In addition, the water expansion increases the pressure within the voids which adversely has a detrimental effect on the asphalt mixture performance. Experimental studies on three different asphalt mixtures with voids content of 3%, 10%, and 14% were performed at low temperature and freeze-thaw cycle to establish a correlation between the asphalt mixtures' properties and the voids' topology. The asphalt mixtures were scanned using Computer Tomography scan to determine the internal structure that evolves during freezing cycles. Semi-circular bending test was used to determine mechanical properties at low temperatures. The results show that asphalt mixture with 3% void content has the lowest and steady degradation rate with the lowest water retention during all cycles. The asphalt mixtures with a

high void content have the highest concentration of water in the pores and decay faster during the initial cycles, but slower during the later cycles because there is less water inside the pores which are fully open and do not retain it. A 3D model was used to simulate the asphalts mechanical and fracture properties discussed in the previous chapter at -10 °C. In addition to the previous chapter, asphalt mixtures mechanical and fracture properties at 20 °C were simulated. The results showed that the asphalt mixture performance is reproduced with 23.08% error for the asphalt mixture at -10 °C and 6.9% for the asphalt mixture at 20 °C compared to the experiments. The damage at low and high temperatures such as cracking was reproduced like the real sample. In addition, higher stress occurs in the area where damage was formed.

Acknowledgments

Firstly, I would like to express my gratitude to my supervisors Dr. Alessio Alexiadis, Dr. Alvaro Garcia-Hernández and Dr. Bahman Ghiassi who have provided the assistance, advice, encouragement without which this research would not have been possible. Their guidance, knowledge and experience guided me through all research. In particular, I am grateful to Dr. Alessio Alexiadis, who gave me the opportunity to start this wonderful journey and especially supported me during my first year at University of Birmingham.

All the technicians of NTEC at University of Nottingham, for their help and guidance in the laboratory activities which contributed to the experiments' success.

To all my colleagues who warmly welcomed me at University, for their support and friendship during this journey.

The catholic communities met across the UK, for their lovely welcome in all the cities I met them, their prayers and thoughts have been really loved.

To all my friends in Italy and around the world, for the loyal friendship and support, encouraging me during the hardest time.

To my family, for the love and support they gave to me not only during this research period but since I moved to the UK.

At last, to Mercy, my biggest thank is for you. Her true Love for me is the only reason I am here at the end of this research.

Table of Contents

List of Figures

List of Tables

Chapter 1

Introduction

1.1. Problem definition

Every nation needs an efficient transportation structure to grow economically and socially. The durability of the road network is under pressure, especially infrastructures designed decades ago, planned for a different volume of traffic, or experiencing harsher climate conditions, from extreme temperatures to heavy rains fall. Asphalt roads are one of the most widely used transportation systems. As a heterogeneous material, asphalt mixture is composed of aggregates, bitumen, fillers, and voids. Only since the end of the 19th century, roads have been made with these materials, even though exist several references in the Bible about bitumen's ancient uses [1]. Bitumen has recently been used to produce asphalt mixture due to the late development of the required technologies for large scale [1].

A wide variety of asphalt mixtures are obtained by changing the ratios of different components [1]. Asphalt mixtures' properties are correlated by their aggregate and binder composition, gradation, distribution and orientation, void ratio, and temperature [2], [3]. Aggregates are stiff enough to resist traffic loads. Bitumen binds the aggregate together in the road surface layer while; it is viscoelastic at high temperatures and stiff at low temperatures [4].

During road life, asphalt mixture deteriorates due to cyclic loading and environmental conditions [5], [6]. Asphalt mixture undergoes several types of damage (Figure 1): fracture, cracking, ravelling, and rutting [7]. In general, damage starts at a small scale as microcracks grow and propagate until the damage is visible at a larger scale [8]. At low temperatures, asphalt mixture is brittle and freeze-thaw

cycles give rise to cracks that cause ravelling and premature pavement failure [9]. There are two types of cracks: adhesive (at the interface mastic-aggregate level) and cohesive (in the mastic) [10], [11]. Understanding the degradation mechanisms described above is crucial for the better design and maintenance of roads.

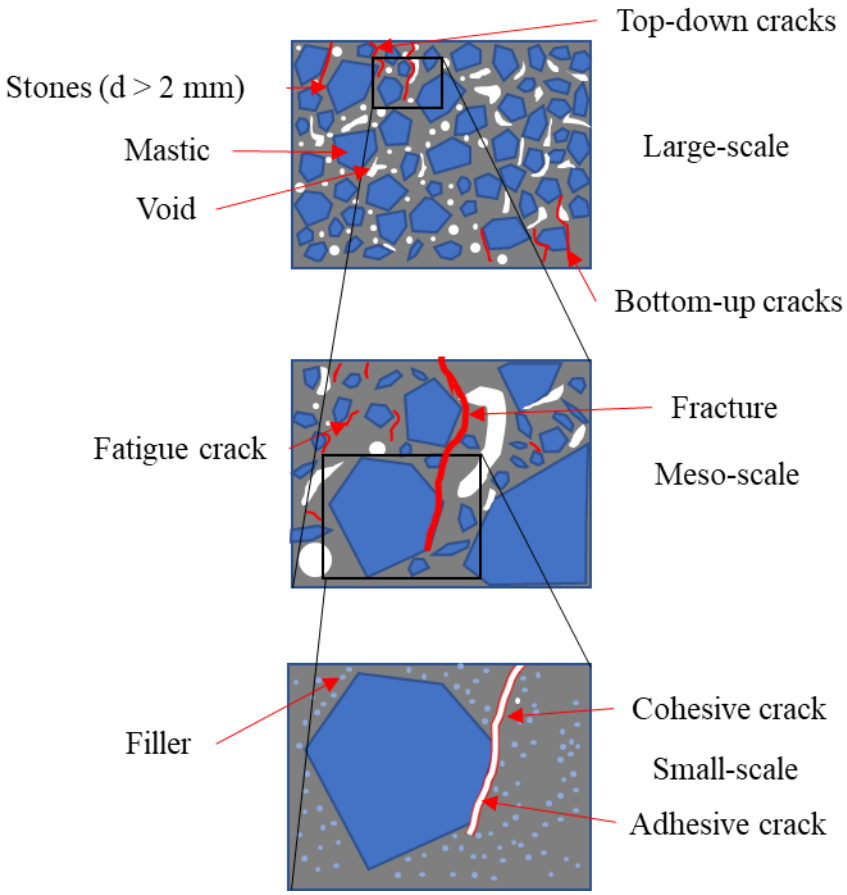

Figure 1: Type of cracks from larger to smaller scale

Many researchers have studied the impact of different gradation, void topology, and temperature on mechanical characteristics and damage using semi-circular bending tests (SCB) [6], [12], [13].

The SCB test is one of the popular methods to study the mechanical properties of asphalt mixture, such as fracture energy, fracture toughness and tensile strength [10], [14], [15]. Although asphalt

mixture’s performances were intensively studied, the literature lacks a comprehensive study on the role of void and aggregate properties along with temperature at a smaller scale [16]. In addition, the correlation between asphalt mixtures’ internal structures and their performances at low temperatures was not established [9].

Despite the SCB test can characterise asphalt mixture performance, it is incapable to assess asphalt mixture's internal structure and its influence on mechanical properties. Therefore, X-ray Computer Tomography (X-ray CT) scans are employed to provide data on void content and topology [9]. X-ray CT scan allows characterisation and quantification of voids percentage, tortuosity, void circularity, roundness, and aggregate topology [8]. In addition, X-ray CT scans can detect damage inside the asphalt mixture providing information about the fracture properties but cannot show the progress of damage of a sample and therefore, limiting the evaluation of deterioration mechanisms, unless the scans are taken at different times. However, numerical methods can provide a tool for understanding asphalt mixture degradation mechanisms and obtaining information from a wide range of conditions [17], [18]. Numerical methods, compared to experimental tests, provide a more flexible and cost-effective alternative to studying asphalt mixture behaviour. SCB tests and numerical simulations can also work in combination [18]. Sun et al. [19], for example, investigated the effect of porosity on crack performance at low temperatures using experiments and discrete element simulations. Xue et al [20] simulated the fracture behaviour of asphalt mixture concrete in 2D with no voids at low temperatures (this, however, makes the fracture not realistic) using the discrete element method. In recent years, asphalt mixture properties have been modelled using both mesh-based methods such as the Finite Element Method [21] and mesh-free methods such as Lattice Spring Model (LSM) [22] and Peridynamics (PD) [23]. Computational studies are usually required to carry out experiments under a variety of conditions such as loading rate and temperature, to obtain mechanical responses [5], [24]. Furthermore, three-dimensional dynamic fracture and multi-crack propagation are still

difficult to model. For instance, in FEM cracks or discontinuities tend to re-mesh making the cracking analysis not realistic [25]. Extended finite element method (XFEM) addresses this limitation by reducing remeshing in cracking analysis, but for heterogeneous material, it is still limited due to facial boundaries requiring more adjustment [26]. However, crack propagation and micromechanical behaviour can be modelled with novel mesh-free methods. The lattice spring model (LSM) is a mesh-free method proposed to represent the body as a lattice, where the nodes model the mass of the material, and the springs represent the mechanical properties [27]. Peridynamics (PD) [23], like LSM, discretises the material using spatial integral equations rather than partial differential equations. Peridynamic is a better method than FEM to model stationary discontinuities and a better method than LSM to model dynamic fracture [8], [28].

There are two categories of Peridynamics: bond-based [23] and state-based [29]. Bond-based Peridynamics models the material as elastic with a fixed Poisson ratio. The state-based Peridynamic has a variable Poisson ratio. The state-based Peridynamic linearly elastic models (LPS) [29] the material as elastic. The viscoelastic Peridynamic solid (VES) [30] models the material as viscoelastic. The elastoplastic Peridynamic solid (EPS) [31] models the material elastoplastic.

As a result, combining experiments with peridynamic computational studies can compensate for the individual limitations discussed and reduce the cost of developing more resistant materials. Using computational methods, this study provides a tool for optimising asphalt mixtures and predicting mechanical and fracture properties. To validate Peridynamic modelling, the mechanical responses of asphalt mixtures under various test conditions have been meticulously measured.

The overall goals of this thesis are to:

- Understand the role of the temperature, water, and internal structure of asphalt mixture on its mechanical and fracture behaviours.

- Develop a reliable procedure to simulate asphalt mixture or infrastructure material, in general, using Peridynamic and Peridynamic coupled with Lennard-Jones to reproduce the asphalt mixture performance. The advanced numerical model adds information which is unprovided by experiments such as local stress and damages

The following steps were required to achieve these goals:

- Determination of the asphalt mixture's mechanical and fracture properties under different conditions such as temperature and water infiltration.
- Determination of the mechanical and fracture properties of each component of the asphalt mixture under the different environmental conditions to obtain the input parameter for modelling.
- Creation of a digital asphalt mixture sample using a CT scan of real asphalt mixture.
- Elaboration of the CT scan to obtain all information regarding voids and aggregate such as content, size, and shapes. In addition, the cracks are monitored to assess the damage under the solicitation.
- Computational reproduction of the uniaxial compression test and the SCB test for the asphalt mixture.
- Investigation and comparison of the mechanical and fracture characteristics of the asphalt mixtures.

1.2. Thesis structure

This thesis is organised as follows:

Chapter 1: Introduction of the project, the research's goals, and objectives.

Chapter 2: Discussion of a Literature review on the several types of asphalt components and mixtures. The properties of the different components of asphalt mixture are presented. The asphalt mixture's mechanical and fracture properties are discussed, providing information regarding how the asphalt mixture behaves under different conditions such as temperature and loading, with a brief review of cracks and damage. Then, the semi-circular bending test is discussed, showing the parameters that this test can provide, followed by a discussion of the CT scan explaining how this examination is conducted and which information provides, elaborating these images with different software, eventually the asphalt mixture numerical micromechanical model's review is presented as well as their development and application in infrastructure materials. This chapter also goes over the theory and background of Peridynamic modelling.

Chapter 3: Discussion of the methodology used in this work. The chapter focuses on materials tested, CT scans of asphalt mixtures and simulation using Peridynamics (PD) which is the method used to simulate the asphalt mixture's mechanical properties.

Chapter 4: Demonstrates the application of Peridynamic and Discrete Multiphysics on digital asphalt mixture at low temperatures and under freezing conditions reproducing the mechanical and fracture performance of real asphalt mixture. CT scans of various asphalt mixtures are used to recreate the digital asphalt mixture in a 2D format. All simulations are performed at a low temperature, in dry conditions, with freezing water. Water is modelled by combining peridynamic and repulsive forces.

Chapter 5: Assesses the influence of the freeze-thaw cycles on the mechanical properties of asphalt mixture and the topological properties of voids, by CT scanning three types of asphalt mixture before and after each freeze-thaw cycle.

Chapter 6: Evaluates, experimentally and computationally, the effect of temperature, aggregate and void characteristics on the mechanical properties and fracture resistance of asphalt mixture. Three

distinct types of asphalt mixture are created and X-rayed to determine the voids and aggregates' internal structure.

The CT scans are used to recreate the realistic structure of the asphalt mixtures that are tested and simulated in 3-D using the peridynamic model at low and high temperatures.

Chapter 7: Examines the research's findings, discusses the conclusions, as well as making recommendations for future research.

Publication arising from this thesis

The following articles have been published as part of this research

Journal paper

D. Sanfilippo, B. Ghiassi, A. Alexiadis, A.G. Hernandez, Combined peridynamics and discrete multiphysics to study the effects of air voids and freeze-thaw on the mechanical properties of asphalt, Materials (Basel). 14 (2021).

D. Sanfilippo, A. Garcia-Hernández, A. Alexiadis, B. Ghiassi, Effect of freeze–thaw cycles on the void topologies and mechanical properties of asphalt, Constr. Build. Mater. 344 (2022) 128085.

Chapter 2

2. Literature review

2.1. Introduction

Asphalt mixtures are heterogeneous materials made of aggregates, bitumen, filler, and voids with complex microstructural, resulting in a wide range of properties. The aggregate is the skeleton of the asphalt mixture and be responsible for the bearing capacity and the load transfer within it; the bitumen, covering the surface of the aggregate, acts as an adhesive of the skeleton, allowing the mix to hold up tensile and shear stresses [2], [3].

2.2. Asphalt mixture component

The individual components of asphalt mixture are introduced in the following subsections describing the chemical complexity and the viscoelasticity of the liquid bitumen, followed by component aggregates.

2.2.1. Bitumen

Bitumen is a hydrocarbon product manufactured from crude oil after distillation, followed by a post-process such as air blowing and blending. In addition, it contains other chemicals such as sulphur, nitrogen, oxygen, and metals [1], [32], [33]. Bitumen's density ranges between 1,010 Kg/m^3 and 1,040 Kg/m^3 at room temperature [1]. The thermal properties vary slightly. For instance, the volumetric thermal expansion coefficient ranges between 55 x 10^{-5} K^{-1} and 63 x 10^{-5} K^{-1} [1]. In addition, below the glass transition temperature (from -40 °C to 5 °C), the thermal expansion

decreases depending on the bitumen source [34]. Bitumen has a relatively small contact angle, therefore can cover dry surfaces [35]. Bitumen has been used in the pavement to improve its performance. Asphalt mixture aggregates are held together by bitumen which acts as an adhesive**.**

The binding performance of bitumen depends on the rheological properties at high temperatures and adhesion properties at low temperatures [11]. In general, bitumen content in asphalt mixtures varies between 4% and 7% [36]. The content influences the properties of mixtures. Bitumen is a viscoelastic material, and its mechanical properties are influenced by temperature, loading rate and time of application. The viscosity and young modulus both increase by lowering the temperature [1] where above the glass transition temperature bitumen is liquid and below the glass transition temperature it is brittle and elastic.

2.2.2. Aggregate

Aggregate is the principal component in asphalt mixture with 94% in weight (wt) which depends on asphalt mixture's performance. Aggregates are solid materials different per grain size, hardness, mineral composition, and shape.

There are two classifications for aggregates based on their sources and sizes. According to EN 13043 [37], there are three types of aggregate: natural, manufactured and recycled. Natural aggregates come from mineral sources subjected to a mechanical process, manufactured are artificially originated and recycled are regenerated from previous constructions. Another classification depends on the size: coarse aggregate is above 2.36 mm, fine aggregate below 2.36 mm, and filler aggregate below 0.063 mm [1]. Experiments have shown better asphalt mixture performance with coarse aggregate [38]. However, asphalt mixture with larger aggregates contains more void due to less compaction [39]. The asphalt mixture's skeleton is constituted by aggregates larger than 2.36 mm, while the mastic is a

combination of filler, aggregate smaller than 2.36 mm, and bitumen [40]. Mastic adds stiffness and stability to the mixture while improving the compaction of the aggregate and controlling void content. The purpose of the filler is to minimize the amount of bitumen used to fill voids in a coarse and fine aggregate mixture, improving asphalt mixture stability and stiffness [41]. Furthermore, when compared to pure bitumen, the mixture of bitumen and filler has a higher viscosity [42].

The primary function of aggregates is to provide load-bearing support while providing grip and abrasion resistance on the asphalt mixture surface [43]. In addition, by choosing different sizes and amounts of aggregate, the number of void content changes and, in literature, this is between 4% and 25% [44]. Asphalt mixture properties are greatly influenced by the volume and distribution of air voids. The aggregate properties, bitumen content, and the size and distribution of air voids depend on the compaction process [45]. The void content and distribution are primarily determined by the coarse-fine aggregate ratio [19]. Other mesostructured factors that affect asphalt mixture performance include bitumen content, aggregate type, and gradation [46].

The aggregate has different shapes and bearing capacities with two indexes: flakiness index following EN 933-3 [47] and shape index following EN 933-4 [48]. The flakiness index is the percentage of aggregate with a thickness smaller than one-half of the longest size. The shape index is a classification of each aggregate into the mixture based on the length-to-thickness ratio measured with a measuring gauge, see Figure 2.

Figure 2: Aggregate shapes. Modified from [1]

2.3. Asphalt mixture types

The literature provides a wide range of asphalt mixtures that are manufactured by choosing different typologies and proportions of aggregate and bitumen. According to the gradation, there are two types of asphalt mixture: continuously graded and gap graded. Continuously graded are made with equal amounts of each aggregate size and this produces an aggregate skeleton with stone-on-stone contact throughout the mixture. The gap graded is made with only a certain aggregate size and results in higher air content compared with the continuously graded.

The main types of asphalt mixture are presented as follows [1]:

- Asphalt concrete
- Dense asphalt
- Porous asphalt
- Hot rolled asphalt

- Stone mastic asphalt
- Mastic asphalt

2.3.1. Asphalt concrete

Asphalt concrete is manufactured following the marshal method according to the standard BS EN 13108-1:2006 [49]. This type of asphalt mixture is a continuous grade with low bitumen; Figure 3 shown below is a typical grade. The asphalt concrete mixtures are built using the concrete principle which means that the grain skeleton is dense with few voids content.

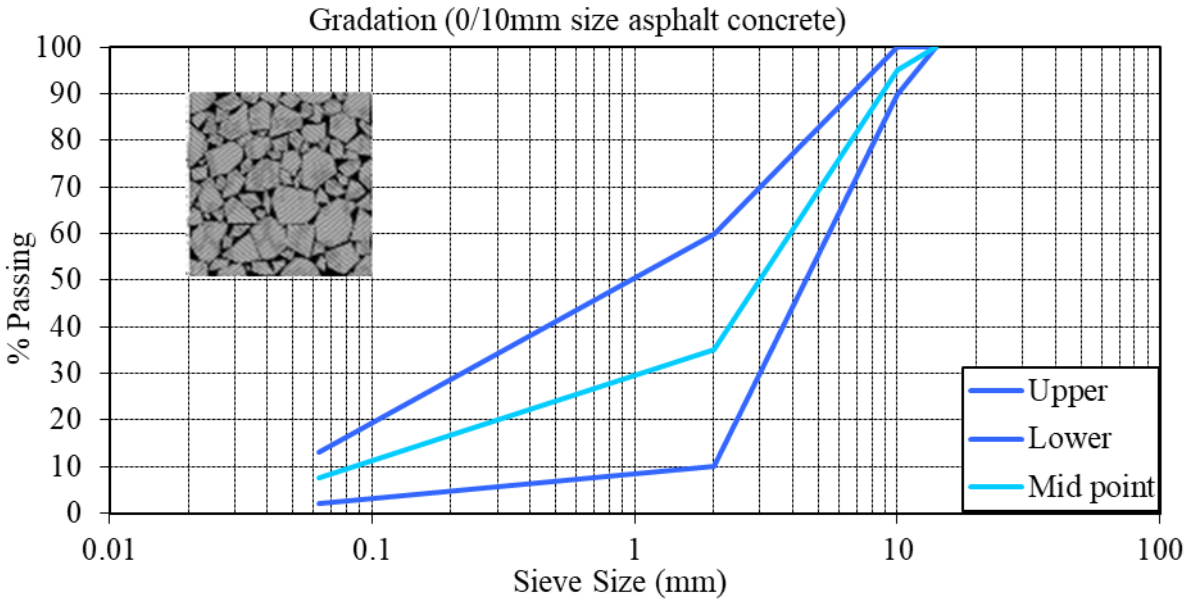

Figure 3: Asphalt concrete

2.3.2. Dense asphalt

Dense asphalt is a densely packed mixture of mineral aggregates that has a strong resistance to deformation [50]. The density of the resulting asphalt mixture can be used to classify it. A nearly

optimal grain-size distribution curve achieves high density, resulting in a low air void content. This mixture is commonly used in road construction [51]. Due to the low voids content, resulting in advantageous excellent resistance to the disintegrating forces of entering water [1]. Water causes harm inside an asphalt mixture, not just when it freezes. It affects the thermodynamic potential of adhesion between mineral aggregate and bitumen, resulting in gradual adhesion loss [2]. Furthermore, water movement in voids promotes the start of early fatigue cracks [50]. A low void content is advantageous for age resistance, i.e. loss of volatiles and oxidation by air [1]. Finally, dense wearing courses protect the bottom asphalt mixture layer from water penetration as well as oxidation [52].

2.3.3. Porous asphalt

The porous asphalt is a gap graded, mostly of a single size coated in a thick bitumen, achieving a good interlock. The mixture has two advantages: relatively low durability compared with the dense asphalt and improved plastic deformation [1]. An open-graded asphalt or porous asphalt is created by widening the gap in the grain-size distribution, see Figure 4. The high enclosed air void content allows the porous asphalt to drain water from the surface faster and reduces wheel noise [3].

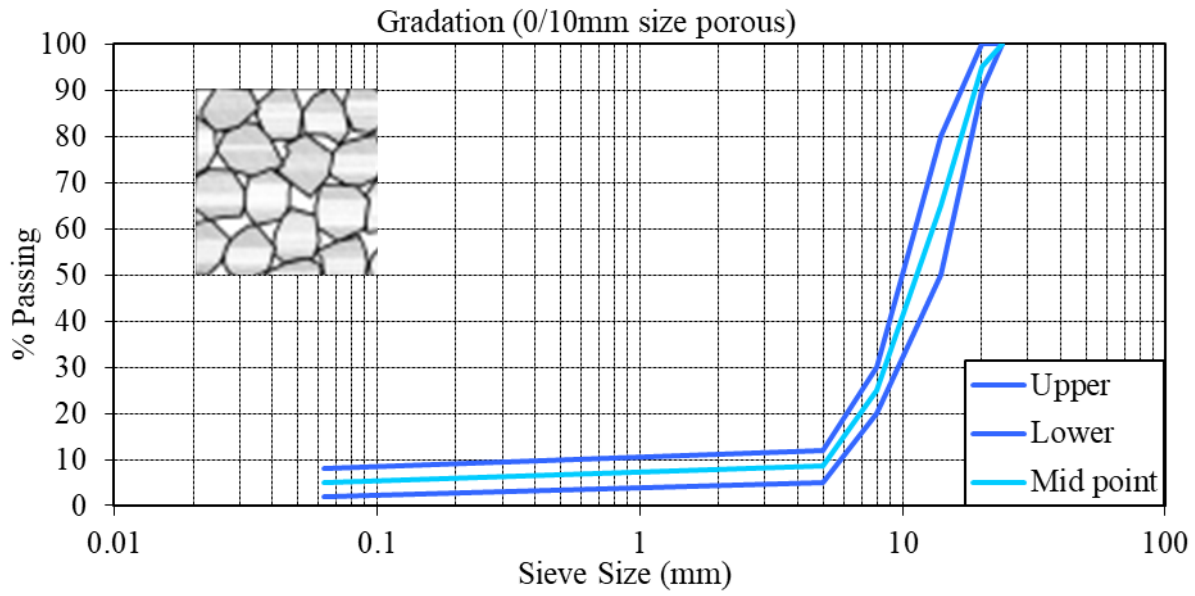

Figure 4: Porous asphalt

2.3.4. Hot rolled asphalt

Hot rolled is defined as a gap-graded with a small portion of medium aggregate size and compared to asphalt concrete, it consists of higher levels of sand, filler, and bitumen. The contact among aggregate is not frequent and the load is transmitted through the mastic which is made by bitumen and filler. It is characterised by a long lifespan. Figure 5 below, shows a typical grade following the standard BS EN 13108-4:2006 [49].

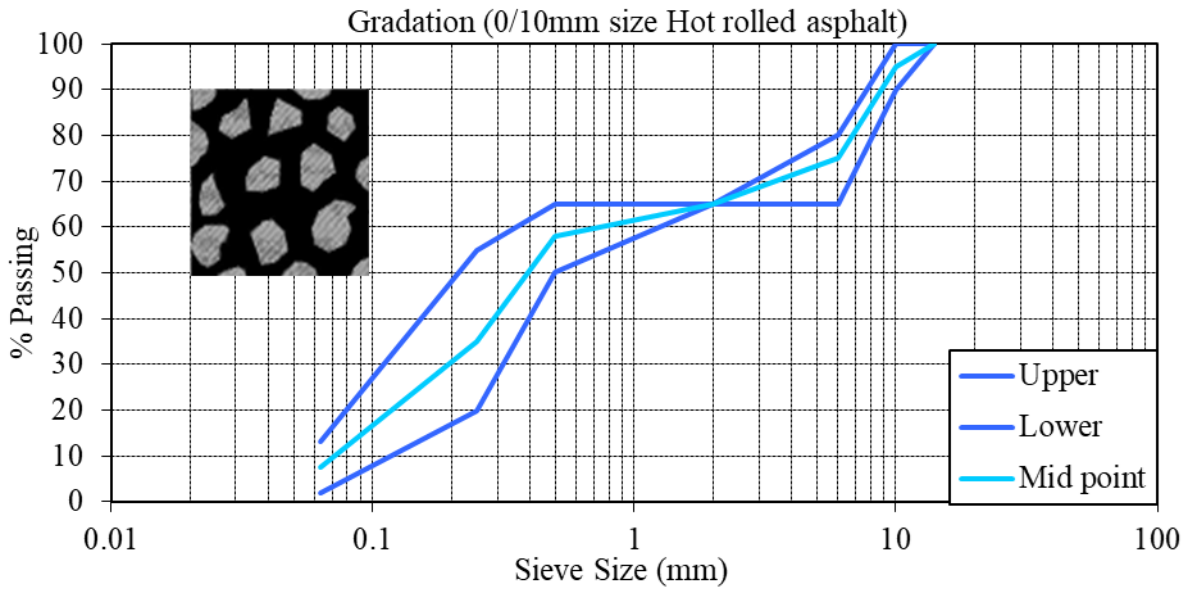

Figure 5: Hot rolled asphalt

2.3.5. Stone mastic asphalt

Stone mastic asphalt, characterised by high rutting resistance, is a dense gap-graded asphalt with high aggregate and mastic content [53]. The high performances are reached due to the skeleton's ability to a carry heavy load. When the stones are in contact, they transmit the stress from one to the other. Furthermore, this asphalt mixture has the best noise reduction and drainage capacity [53]. The cracks are limited by the amount of mastic that decreases the void content. Figure 6 shows a typical aggregate grading curve following BS EN 13108-5:2006 [49]. The mixture is applied when high stability and low noise are required [1].

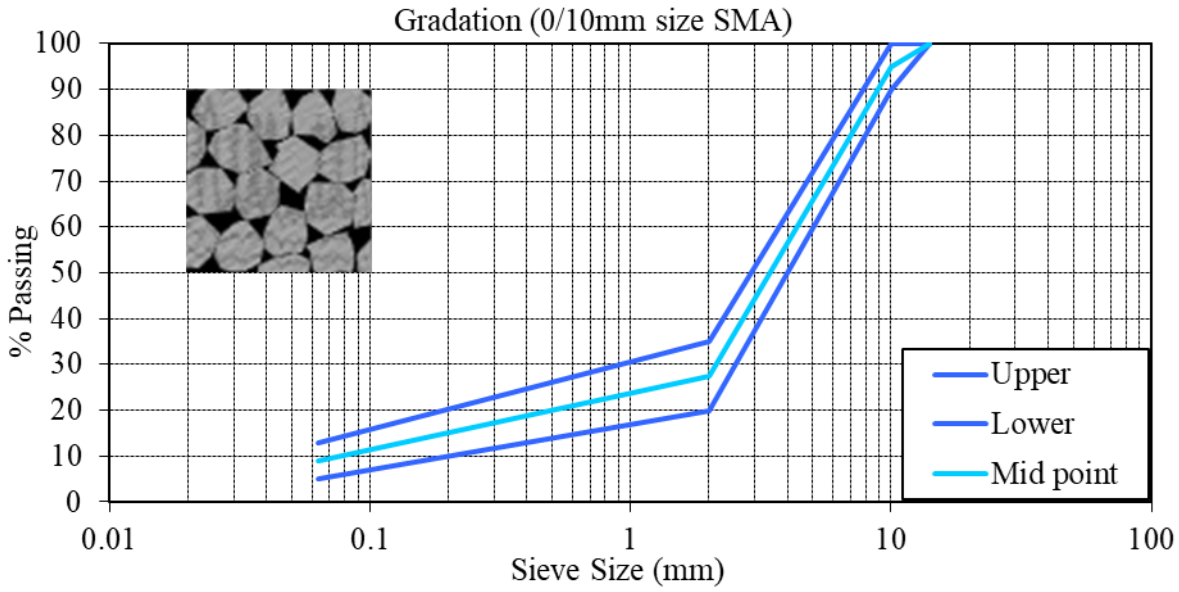

Figure 6: Stone mastic asphalt

2.3.6. Mastic asphalt

Mastic asphalt is made of bitumen and fine material whereas the latter is characterised by an extensive surface area. The fine material element contributes to the impermeability of the mastic asphalt, resulting in high binder content. Because of the high binder concentration, the material is only used for specialised applications such as waterproofing bridge decks [1].

2.4. Review of mechanical properties of asphalt

The design of asphalt mixture is based on its mechanical properties and its fracture behaviour. Asphalt mixture behaves as a viscoelastic material; it exhibits time and temperature dependency along with a response determined by past solicitations [54]. The viscoelastic responses depend on the properties of its component (bitumen and aggregate). Bitumen influences the viscoelastic properties, while aggregate influences elastic and plastic properties of the mixture [1]. When a load is applied, elastic materials deform with reversibility, while viscoelastic materials deform irreversibly. Asphalt

mixture’s response is considered linear viscoelastic in the absence of damage [55]. This implies that the deformation is directly proportional to the applied load which is not necessarily true for other types of viscoelastic materials.

Asphalt at low temperatures is elastic, while at high temperatures it behaves as a viscoelastic material with a time-temperature dependence on strain and stress [56]. Even at normal service temperatures, asphalt can have some unique characteristics as a viscous liquid. Asphalt "flows" at high temperatures, leading to ruts, while it fractures at low temperatures. Also, the stress rate influences asphalt. For instance, at a small load rate, the asphalt is fewer stiffs and remains permanently deformed at a high load rate which is stiffer and prone to fail. At any given strain rate of loading, the material relaxes rapidly enough to prevent stress from developing in the test sample above a particular temperature. Therefore, in a linear viscoelastic area, the stress is associated with the strain which is solely determined by time rather than the rate of stress [57].

There are different experimental tests to characterise the asphalt under these conditions like monotonic loading of both stress-controlled or strain-controlled tests, repeated load tests, creep, and relaxation [58]. The creep test is used to determine the linear properties of the material [59]. The test consists of applying a constant strain or stress on a sample, recording both stress and strain against time.

The linear response of a material follows Hooke’s law [20] which represents the strain/stress characteristics (e.g. stiffness) identifying critical stresses and strains and revealing its mechanisms of failure. The stiffness of asphalt is a crucial value affected by many factors including stress state, temperature, moisture, strain rate, and damage condition [1].

The stiffness or Young modulus of a material expresses the ability to resist deformation under tension or compression and relates stress to strain [60].

The young modulus is expressed as

$$[D] = \frac{\{\sigma\}}{\{\varepsilon\}} \tag{1}$$

where, σ is the stress tensor, ε is the strain tensor and D is the stiffness matrix defined as

$$[D] = \frac{E}{(1+\upsilon)(1-2\upsilon)}\begin{bmatrix} 1-\upsilon & 0 & 0 & 0 & 0 & 0 \\ 0 & 1-\upsilon & 0 & 0 & 0 & 0 \\ 0 & 0 & 1-\upsilon & 0 & 0 & 0 \\ 0 & 0 & 0 & \frac{1}{2}-\upsilon & 0 & 0 \\ 0 & 0 & 0 & 0 & \frac{1}{2}-\upsilon & 0 \\ 0 & 0 & 0 & 0 & 0 & \frac{1}{2}-\upsilon \end{bmatrix} \tag{2}$$

Where υ is the Poisson ratio.

Equation (1) for an elastic material establishes that stress and strain are constant, and the material relaxes instantly after the stress is removed, see Figure 7 (a).

As previously discussed, under the viscoelastic regime, the stiffness is directly influenced by the shift of temperatures and loading conditions. For instance, the material under constant stress increases the strain and after the stress is removed the strain return slowly to zero value, see Figure 7 (b).

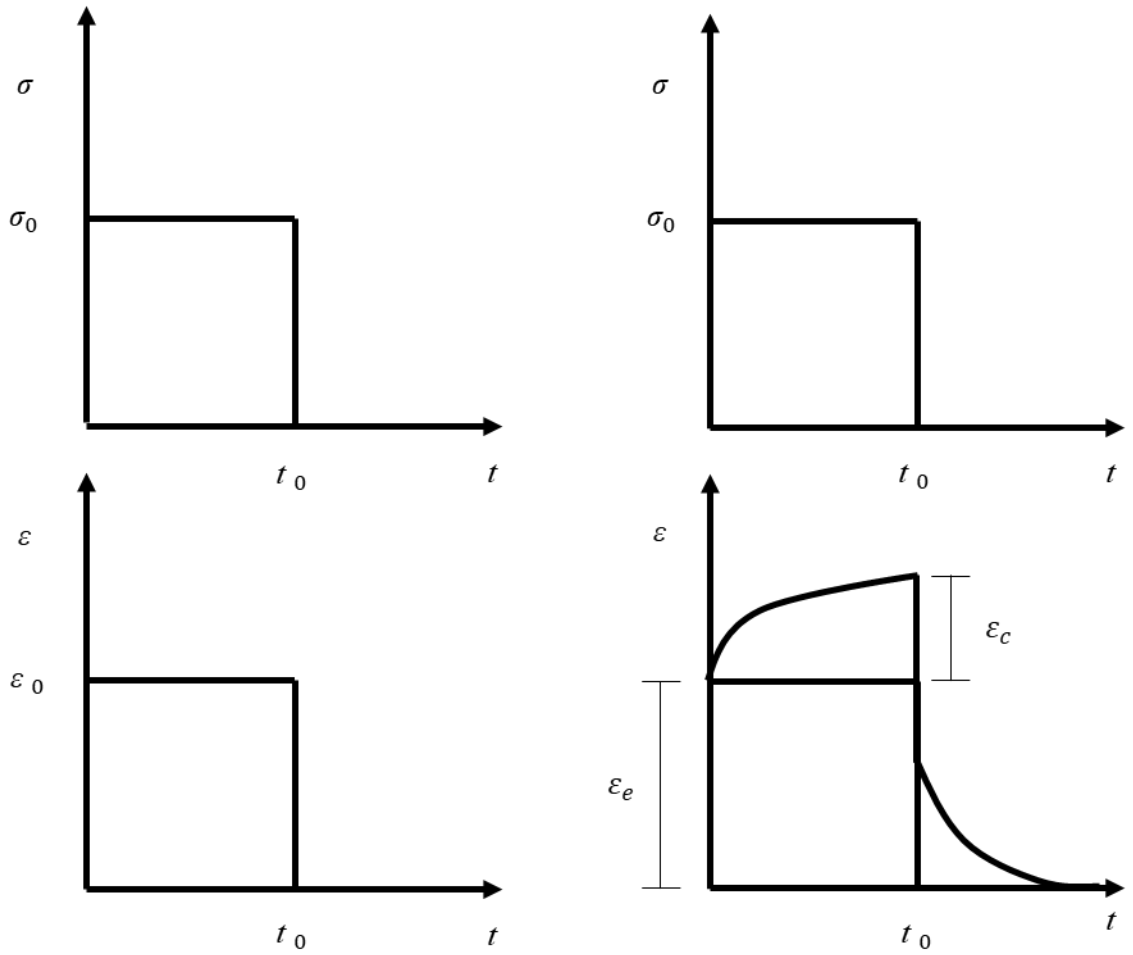

(a) (b)

Figure 7: Creep test of elastic (a) and viscoelastic material (b)

The creep test under constant stress is described by:

$$\sigma\ (t) = \sigma_0 \tag{3}$$

$$\varepsilon(t) = \varepsilon_e + \varepsilon_c(t) \tag{4}$$

where σ_0 is a constant stress, and ε_e is the elastic strain totally recoverable and $\varepsilon_c(t)$ is the strain that vary with time and recoverable gradually after the stress is revealed.

In case of a constant uniaxial strain, the equation (1) assumes a more general form as

$$\sigma\ (t) = E(t)\varepsilon_0 \tag{5}$$

$E(t)$ is the relaxation modulus.

Asphalt mixture and mastic are linear viscoelastic materials, in an undamaged state. To be linear, the material must satisfy two conditions: superposition and proportionality principles. The proportionality principle implies that solicitation and response are proportional. The superposition principle consists of the additivities of the stress and strain at time t which means that the effect of two separate solicitations acting at the same time *t* is equal to the sum of each solicitation at different time *t* [61].

For example, a material undergoes two different stresses: $\sigma(\varepsilon_1)$ and $\sigma(\varepsilon_2)$ and two strains: ε_1 and ε_2.

The superposition is mathematically expressed as

$$\sigma[\varepsilon_1(t)] + \sigma[\varepsilon_2(t)] = \sigma[\varepsilon_1(t) + \varepsilon_2(t)] \tag{6}$$

Considering also that the stress and strain are proportional, if the stress is multiplied by a constant β

$$\beta_1\,\sigma[\varepsilon_1(t)] + \beta_2\,\sigma[\varepsilon_2(t)] = \sigma[\beta_1\,\varepsilon_1(t) + \beta_2\,\varepsilon_2(t)] \tag{7}$$

Considering the viscoelastic material are history dependent the equation (5) became the followed integral

$$\sigma(t) = \int_0^t E\,(t-\xi\,)\frac{d\varepsilon}{d\xi}\,d\xi \tag{8}$$

where σ is the stress, ε is the strain, t is the time, ξ is an integral variable, and the relaxation modulus $E(t)$ can be expressed as Prony series through the generalised Maxwell model [62].

$$E(t) = E_e + \sum_{i=1}^{N} E_i e^{\frac{-t}{\tau_i}} \tag{9}$$

where E_e is the equilibrium modulus; E_i the discrete relaxation spectrum and τ_i relaxation time, N is the number of elements in the maxwell model.

The parameters E_e, E_i and τ_i in the equation (9) can be described using the storage modulus data from the complex modulus.

$$E\,(\omega) = E'(\omega) + iE''(\omega) \tag{10}$$

The $E'(\omega)$ is the storage modulus and $E''(\omega)$ is the loss modulus which are the real and imaginary part of the complex modulus $E(\omega)$ in the frequency domain represented in

$$E'(\omega) = E_e + \sum_{i=1}^{N} E_i \frac{\omega^2 {\tau_i}^2}{1 + \omega^2 {\tau_i}^2} \quad (11)$$

$$E''(\omega) = \sum_{i=1}^{N} E_i \frac{\omega \tau_i}{1 + \omega^2 {\tau_i}^2} \quad (12)$$

where ω is the angular frequency; i is the imaginary unit.

The time-temperature superposition principle can be applied to the linear viscoelastic domain to obtain the reduced angular frequency ω_r and reduced time t_r. The master curves of linear viscoelastic materials functions for asphalt mixtures and mastic are created using this value, by shifting the data measured at different temperatures along a logarithmic time or frequency axis [61].

$$\omega_r = \omega \, \alpha_r \quad (13)$$

$$t_r = \frac{t}{\alpha_r} \quad (14)$$

The Williams Landel-Ferry (WLF) equation (15) provides the horizontal shift factor of test results α_r, also called time-temperature shift factor

$$\log \alpha_r = -\frac{C_1 (T - t_r)}{C_2 + (T - t_r)} \quad (15)$$

where C_1 and C_2 are the model parameters; and T is the physical temperature and t_r is the reference temperature.

2.5. Deterioration of asphalt

Pavement's resistance to damage is influenced by many factors, including environmental conditions, loading history, material quality, structural design, and type of maintenance [63]. Defects drastically shorten pavement lifespan and increase maintenance and repair costs [64]. In this thesis, two main deterioration factors are investigated: mechanical and environmental.

The mechanical factors are consequences of loading conditions such as tension, compression shear mode and load rate and cycling solicitation, whereas the environmental factors are a consequence of temperature fluctuation, water and ice exposition. Furthermore, these factors can happen simultaneously. This thesis investigates three main damage mechanisms: cracking, rutting and freeze-thaw cycle.

Asphalt mixture deteriorates due to cracking and rutting occurring at low and high temperatures. Both mechanisms interest the aggregate mastic interface. The interface between mastic and aggregate has complex physics and chemical properties. Different studies have highlighted the interface's vulnerability to different loading and environmental solicitation [65], [66], [67]. Several factors influence the adhesion between aggregate and mastic. These can be separated into internal and external factors [11], [68]. Internal factors are the characteristic of the single asphalt mixture component like the shape and size of aggregate and the chemical properties of mastic and aggregate. These internal factors influence the bonding between mastic and aggregate which is the ability of mastic to adhere to the aggregate. For example, aggregate with a smooth surface adheres less to mastic compared with a rough one, due to the limited surface area in contact with mastic. External factors are the loading and environmental conditions such as temperature, moisture, compression, tension, and shear stress [69].

Moisture is one of the causes of premature failure affecting the interface which leads to other damages such as ravelling, rutting, and cracking [7]. In asphalt mixture, ravelling is the result of friction between vehicle tires and asphalt layers on asphalt pavement causing loss of aggregates from the asphalt [70]. Rutting is a depression of asphalt surface along the wheel path due to strain accumulation [71]. Cracking is a fracture which occurs within the asphalt pavement after the stress exceeds the bearing capacity of the material [72]. In [7] experiments in dry and wet conditions were conducted to study the impact of water at the interface. Researchers do not agree on the physics behind adhesion with several theories presented in an attempt the explaining this. Among these adopted theories there are mechanical theory, chemical theory [73], weak boundary theory, molecular orientation theory [74], electrostatic theory, surface free energy theory.

2.5.1. Cracking

Cracking is one of the most important problems in pavement systems, and it may be caused by either excessive traffic or temperature [75]. At intermediate temperatures, fatigue and durability cracking occur in asphalt pavement are caused mainly by cycling load and poor gradation asphalt mixtures. At low temperatures, asphalt pavement is brittle and thermal cracks are caused by thermal distress in cold regions [76]. Cracking significantly reduces the ride quality which is further decreased due to water ingress from the surface into the underlying soil layers [5]. This reduces pavement life and requires more frequent pavement repair and maintenance. As a result, crack resistance is a critical quality of any long-lasting asphalt mixture. Crack resistance is affected by the following factors: design and construction quality of the mixture, ageing of the asphalt binder, and moisture damage [77].

The fracture mechanism of asphalt mixtures has been extensively studied in the last decades [72], [78], [79]. Different theories have been presented such as elastic theory, strength theory, and fracture mechanics theory [80]. These theories viewed the asphalt mixture as an ideal material (homogenous, isotropic, and continuous) that fractures when the yield stress or strain is exceeded. For example, Chehab et al [80] proposed a model including elastic, viscous and plastic components of asphalt mixture for investigating loading rate, stress, and temperature. The model predicts fracture behaviour with the help of digital images.

The main theory in engineering applications for crack representation has been proposed by Griffith [81] based on global energy equilibrium to resolve the problem of crack initiation in a brittle material. According to the Griffith theory, there are two stages of cracking [82]: initiation and propagation. As shown in Figure 10, the crack initiation stage is the first step in crack development. Therefore, studying crack initiation is essential in forecasting material failure.

In a 3D material body, when the stress locally exceeds the ultimate bearing capacity of the material, cracks occur resulting in a fracture with a two-dimensional matching surface [15], see Figure 8.

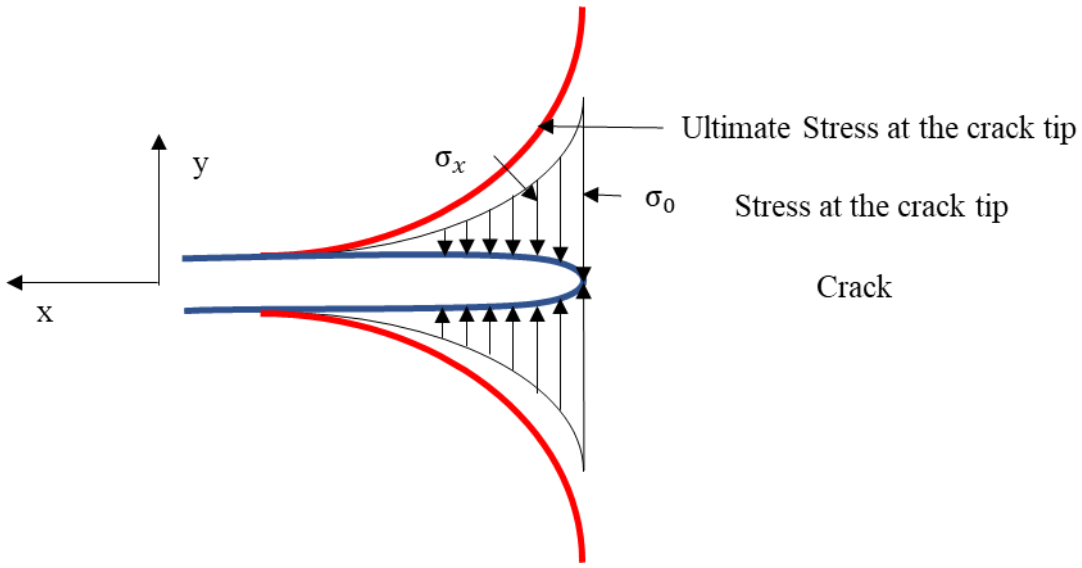

Figure 8: Stress at the crack tip

Crack frequently begins at the micro-scale, where the high stress and the large plastic deformation weaken the area around the crack tips. Once the stress reaches the local bearing capacity, the crack begins to coalesce into a macro crack and eventually becomes a fracture [81], see Figure 10. Cracks can propagate within one material (cohesive) or at the interfaces between materials (adhesive) [83]. The cohesive and adhesive cracks release different surface energy respectively. Cohesive crack is typical of viscous material and is time-temperature dependent [72]. The adhesive crack occurs at interfaces and low temperatures [84], see Figure 9.

(a) (b)

Figure 9: Adhesive crack (a), Cohesive crack (b)

Researchers have developed fatigue crack initiation criteria that can be used for asphalt mixture materials to implement the use of Griffith’s theory. For example, Luo et al. [85] employed Griffith's theory when performing tensile fatigue test on asphalt mixtures with scattered cracks to create the fatigue crack initiation criteria. Gao et al. [86] applied Griffith's theory to establish the appropriate crack initiation condition for asphalt binders under fatigue shear load. The crack initiation criterion is employed to compute the surface energy of asphalt binders. In asphalt mixture materials, fatigue

fracture initiation can be studied using these models which provide descriptions of physical mechanisms. In terms of the crack start criteria of asphalt mixture materials, the expressions differ when comparing under tension, compression, and shear loading.

Experiments such as Semi-circular bending (SCB) test, Indirect tensile (IDT) , Brazilian test, provide a different parameter to assess fracture mechanism, including fracture toughness, fracture energy, tensile strength, flexibility index, critical value of the J-integral, and cracking resistance index [20]. These tests and parameters limit the evaluation of asphalt mixtures at macroscopic scale, while for a better understanding of cracking phenomena it is required information at smaller scale.

For instance, Wu [84] investigated asphalt mixture fracture behaviour at low temperatures and determined its fracture toughness. When studying the fracture process of asphalt mixtures, there are several issues to consider such as [87] asphalts mixture with the same grade that have different fracture properties due to larger aggregate inside the projected crack path.

The fast-reducing temperature causes cracks in the pavement due to the tensile stress in the structural layer. At low temperatures, asphalt mixture physically hardens, and performance under stress relaxation is reduced, while thermal tensile stress and external loading stress are increased [88]. Teng et al [88] showed through numerical analysis the crack appears at the interface and mastic at high temperatures and only at the interface between aggregate and mastic at low temperatures.

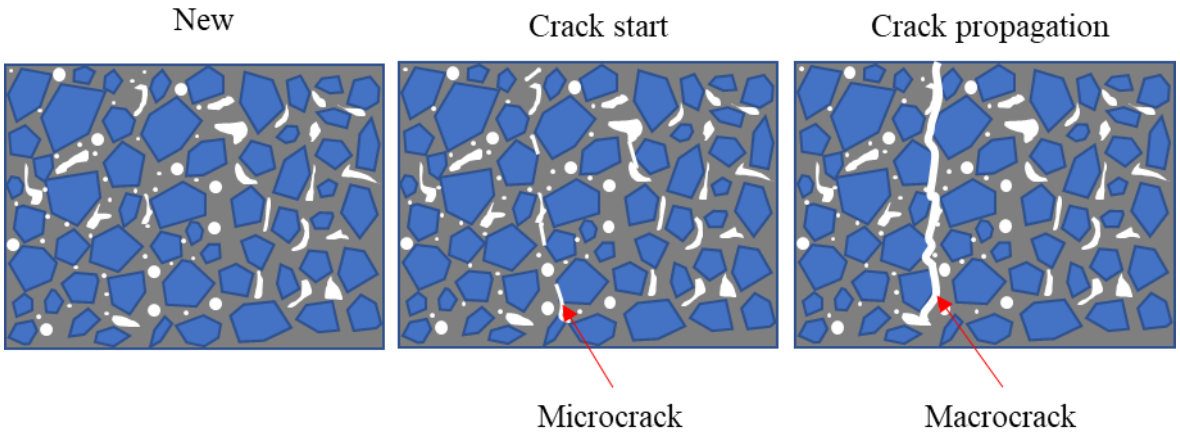

Figure 10: Cracking

2.5.2. Freeze-thaw cycle

Water ingress and extreme temperature fluctuations [89] in cold regions cause asphalt mixture to degrade more rapidly, resulting in thermal stress [84], lower adhesion at the interface's aggregate-bitumen [90], and lower binder cohesion [91]. The freezing water in the pores increases the pressure during expansion. The expansion of water under freeze-thaw cycles can also increase the number of air voids in asphalt mixture which increases asphalt mixture permeability and, as a consequence, the risk of freeze-thaw damage [89], [92], see Figure 11.

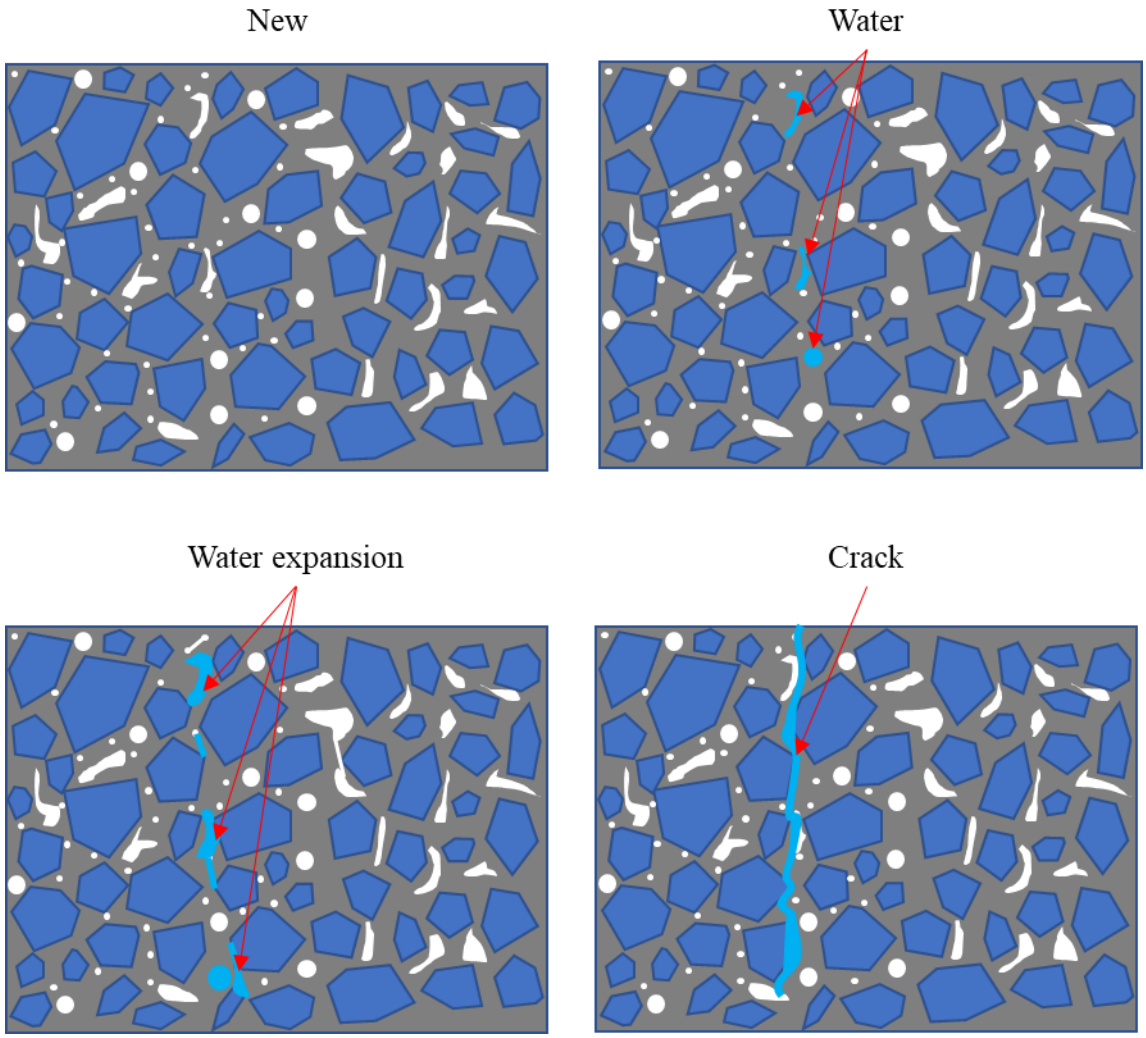

Figure 11: Freeze-thaw cycle

When expanding water compresses a brittle mix, it increases the stress that accumulates rapidly enough to form a crack. During melting, water permeates through the cracks, causing further damage to the structure with additional freeze-thaw cycles, reducing the stiffness modulus [93], strain energy [93], fracture toughness [94], and critical stress [94] of asphalt mixture. Sol-Sánchez et al [91] investigated the long-term asphalt mixture properties for dense and open mixtures during freeze-thaw cycles, demonstrating that void impacts performance. This study [91] investigated the influence of long-term moisture influences for dense and open asphalt mixtures. Two trends are identified for both mixtures: a strong decrease in mechanical performance within the first cycles, higher for the open asphalt mixture, and the slowest decrease of performances in the latter cycles, higher for the dense asphalt mixture. Therefore, dense asphalt mixture has a higher reduction of stiffness after 30 freeze-thaw cycles in a cold region and heavy rainfall areas. The authors correlate the finding with the water retained suggesting the open asphalt mixture is more appropriate for heavy rainfall areas.

During the expansion of water, cracks are created, forming and modifying new voids, as well as altering the interior void structure [95].

Considering the material complexity, it is essential to use visual inspection and standard experimental tests, as well as mathematical and numerical models to understand how the damage evolves.

Xu et al. [96] for example, utilised X-ray CT technology to assess the internal structure changes under freeze-thaw cycles for three different asphalt mixtures. The contribution of X-ray CT scans, in [96], was fundamental to understanding the different mechanisms of the internal structure evolution under the freeze-thaw cycle. Analysing the different images after each cycle, the authors observed three mechanisms of internal structure changes: 1) expansion of existing void, 2) coalescing of two or more voids, and 3) creation of new voids. Furthermore, the three asphalt mixtures behave differently under freeze-thaw cycles. The authors attribute the different internal structure changes to the aggregate gradation. In addition, in [9], the void topologies and their modifications using CT scans are related

to the loss of asphalt mixture characteristics to provide information for better asphalt mixture design and address the loss of fracture resistance. Fractures and deterioration of the asphalt mixture are caused by voids that change in size and shape.

2.6. Experimental test

Having a basic understanding of asphalt mixture mechanical and fracture properties is essential when designing a pavement and evaluating its performance [97], [98]. There is a variety of tests proposed in the literature for asphalt mixture, including the semi-circular bending test, three-point bending, indirect tensile test, Brazilian test, and disc-compact test. These tests provide information on the mixture's strength and relative brittleness [99].

The semi-circular bend (SCB) method is one of the most widely used tests to investigate asphalt mixture performance. The SCB test is also a means of understanding fracture mechanisms due to its simplicity and good availability of theoretical basis [100], [101]. The SCB test follows the EN12697-44: 2010 [102] standard which specifies the sample geometry, the support, and the loading conditions but does not specify such variables as temperature or water. Stress, strain, fracture toughness, and fracture energy are all factors included in the outcome.

For the test, a semi-circular sample of asphalt mixture with a notch in the middle is placed on two roll supports. The monotonic load is delivered at a constant rate from the top of the sample downward until the sample fails. In a three-point bending mode, this load causes stress in the lowest portion of the specimen [103], see Figure 12.

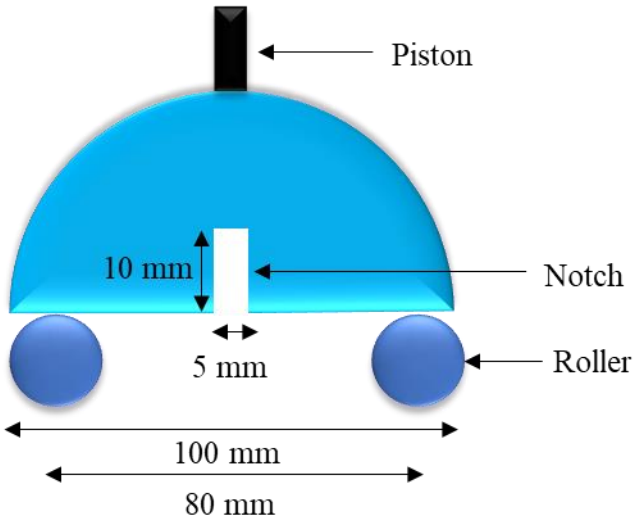

Figure 12: Semi-circular bending sample

The specimen becomes stressed under load which can cause a crack to propagate along the load direction, particularly at low temperatures when the asphalt mixture is elastic. The stress and strain values are recorded, and a graph is drawn to provide the stiffness value discussed in the above section as well as all the other information calculated from it and discussed in the following part.

An asphalt mixture's fracture resistance is evaluated using two parameters: fracture toughness and fracture energy [104]. The fracture toughness of asphalt mixture is one of the key fracture characteristics that can be used to analyse its fracture performance under various tests and settings [14]. The fracture toughness index is a key parameter in determining fracture resistance capacity since it represents the stress limit after which the fracture propagates through the material and is considered one of the most important parameters for materials containing a crack [12], [13]. According to traditional fracture mechanics, each mode of loading has a fracture toughness value per material, such as tension, shear, and tear. Several testing methods have been developed to determine this parameter [27].

According to the standard used, it is possible to calculate the fracture toughness when the failure occurs with the equation.

$$K = \sigma_{max}\, f\left(\frac{a}{w}\right) \tag{16}$$

where σ_{max} is the maximum stress at failure calculated as

$$\sigma_{max} = \frac{4.263\, P_{max}}{D\, t} \tag{17}$$

where P_{max} is the maximum load at failure, D is the diameter of the asphalt mixture sample and t is the thickness of the asphalt mixture sample.

$f\left(\frac{a}{w}\right)$ is a geometric function which is 5.956, for 9 < a_i < 11 mm and 70 < W_i < 75 mm. For other a_i and W_i values, the geometric value is different for different specimen geometries and can be calculated according to the formula presented as follow [49]

$$f\left(\frac{a_i}{W_i}\right) = -4.9965 + 155.58\left(\frac{a_i}{W_i}\right) - 799.94\left(\frac{a_i}{W_i}\right)^2 + 2141.9\left(\frac{a_i}{W_i}\right)^3 - 2709.1\left(\frac{a_i}{W_i}\right)^4 + 1398.6\left(\frac{a_i}{W_i}\right)^5 \tag{18}$$

Previous research [105] discovered fracture toughness dependencies on parameters such as sample thickness, loading condition, aggregate type and gradation, and support condition. The aggregate type has an impact on fracture toughness; for example, in [106], the reduction in fracture toughness with air void content is studied using two asphalt mixtures with the same amount of aggregate but different types (limestone and siliceous), with siliceous showing the greatest fracture toughness reduction. Additionally, asphalt mixture with more hardened bitumen has greater fracture toughness due to its superior resistance to fracture while large aggregates are also more resistant to fracture. Due to the repeatability of the test, it is possible to determine the influence of the mixture composition.

Asphalt mixture fracture performance can also be estimated using fracture energy and which is calculated as the area below the curve stress/strain and express the energy released during the fracture [102]. Equation (19) is used to calculates fracture energy

$$G_f = \frac{W_f}{A_{lig}} \tag{19}$$

G_f denotes the fracture energy (J/m^2), and W_f denotes the work of fracture (J), A_{lig} represents the ligament area (m^2).

$$A_{lig} = (r - a)\ x\ t \tag{20}$$

where r represents the specimen radius (m), t represents the specimen thickness (m), and a represents the notch length.

According to the SCB test standard [102], the ligament area in front of the cracking tip is defined as the product of the ligament length and the ligament width, where the width is 0.04 m, and the length is 0.05 m.

Researchers have shown that fracture energy, rather than fracture toughness defines both crack initiation and propagation [107]. It has been observed that the fracture energy is influenced by material properties and loading conditions [108], and specimen geometry [109]. The fracture toughness and fracture energy provide information about the asphalt mixture's ultimate properties. However, the propagation of cracks has not been studied. There has been little research in the literature on fracture growth and propagation.

Several techniques such as digital image analysis are used to analyse the fracture growth which required comparison with a gauge attached to the notch. This equipment measures the horizontal length of the notch and compares it with a photo of the opening. However, these photos only show the visible cracks on the surfaces. The following sections discuss other approaches to crack detection, such as X-ray CT scan and a numerical model.

The crack velocity is the length of the crack divided by the time it takes to propagate and is used by [110] to determine the fracture performances and given by

$$v = \frac{\Delta l}{\Delta t} \tag{21}$$

Where v = velocity of the crack, Δl = length of the crack, Δt = time

The fracture velocity has a positive correlation with the air voids content. Moreover, crack initiation occurred along the interfacial aggregate border, and aggregate gradation did no effect on crack velocity.

Despite these tests provide valuable results to evaluate asphalt's mixture mechanical and fracture properties, they are time consuming due to complexity of compaction, manufacturing process, test conduction and analysing the outcome. The literature lacks a reliable correlation between the topology of asphalt mixture component and asphalt performance under different condition. Therefore, understanding the correlation between the asphalt mixtures and its performances will improve the design of the pavement.

2.7. Review of X-ray CT scan

Asphalt mixture has a complex mechanical response and fracture behaviour due to its heterogeneous composition. According to the previous paragraph, experimental investigation helps in studying these characteristics, but it is limited by mechanical interaction among components and damages.

Researchers have used CT scans to investigate the effect of asphalt mixture and its evolution under different loads and environmental conditions [169], [111], [112], [113], [114]. The performance of asphalt mixture and its damage can also be predicted by using a microstructural model based on the actual microstructure. However, CT scans are expensive. To use computational methods (discussed in the next section), a digital sample is required which can be acquired in two ways: discrete element method using the random generation of asphalt mixture, and a realistic image based on asphalt mixture's tomography. Using discrete element software, the random generation creates a microstructural model of asphalt mixture and predicts its performance through virtual testing [113], [115], [116], [117], [118]. In general, this method has been used for a 2D model and with aggregate with an unrealistic shape.

The image processing technique involves acquiring tomographic images of asphalt mixture to obtain its structure. By using digital image processing (DIP), a three-dimensional model can be constructed, and image analysis, such as fractal analysis of cracked asphalt mixture, can be conducted [114], [119].

Comparing the reconstructed microstructures with random generation, the reconstructed microstructure provides a better representation of an actual microstructure [120].

The growing availability of hardware in combination with the development of software tools explains the recent growth and development of algorithms for analysing and interpreting huge data volumes. Coleri and Harvey [17], [121] examined the changes in aggregate distribution and void angles to identify rutting. They also looked at the effects of aggregate movement, porosity, and air-void angle on the density and shear rheology of asphalt pavements. Moreover, Taesun [122] study the damage distribution of asphalt concrete using the constitutive model of coupled thermo-viscoelastic, thermo-viscoplastic, and thermo-viscodamage.

Qualitative 3D representations can be useful for seeing pore morphologies or the network structure of the pores, or the location and extent of a fracture. However, a 3D quantitative analysis is essential for sample comparison and data analysis. In addition to evaluating aggregate packing [123], fatigue damage [124], and internal structure change under loading and freezing-thaw [125], CT scanning technology also contributes to research on other asphalt mixture characteristics performance.

2.7.1. Description of X-ray CT scan's

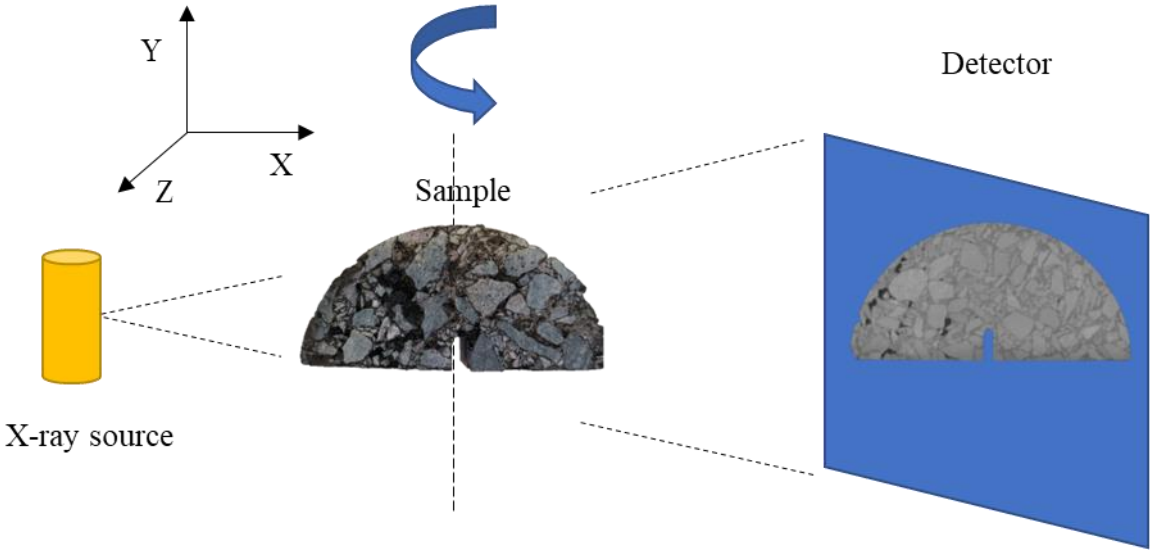

Figure 13: Schematic representation of a typical CT system

Figure 13 shows the schematic representation of the CT scan process. The sample is positioned on a rotation stage which is irradiated by an X-ray source that by passing through the sample reveals a planar detector. The resolution depends on the sample size and loading angle influence; thus, to obtain the best scan image quality and resolution, it may be necessary to section the sample. As a result, 2D projection images on the detector are formed by projecting the X-ray cone beam onto the sample. The sample is loaded sideways in this scenario to achieve the shortest material penetration distance as well as several angles to enhance contrast, positioned at any angle. To minimise surface artefacts, the sample's flat surface must be maintained parallel to the X-ray direction. With non-destructive testing, large cracks or faults are easily detected.

The X-ray CT scan settings require a bespoke setting based on the sample type and size. The scan's purpose determines the optimised parameters. During the CT scanning procedure, the sample does a full 360-degree rotation producing and recording between 500 and 4000 2D projection images. To reconstruct the volumetric dataset, the images obtained from the CT scan are converted into a 3D grid of volumetric pixels (voxels), where the brightness values correspond to the density of the material.

For instance, denser materials are brighter in CT scans. Figure 14 shows a CT image of an asphalt mixture sample with a close-up region showing particles, void spaces, and bitumen.

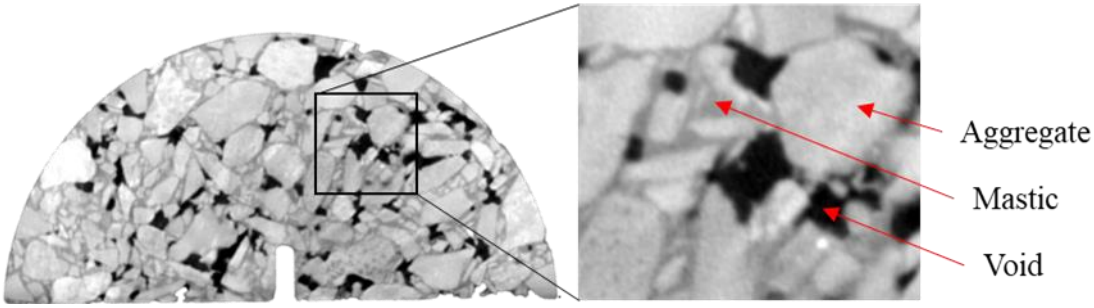

Figure 14: Asphalt mixture CT scan

In most cases, a CT result does not require additional work or further data processing. Observation of images individually is enough to see a different part of the samples.

2.7.2. Topology of void and crack

An important use of CT is to assess the damage and visualise the porosity. Analysis of porosity or damage information involves identifying pore spaces or voids in a material, as well as visualising and analysing the porosity spatial distribution from a qualitative and quantitative visualisation, Figure 15.

A CT scan is limited by the available resolution [169]. A CT scan on a small sample can obtain a better resolution, maximising the quality and allowing the observation of smaller components. However, a small sample of heterogeneous material may lose information at a larger scale such as macropore characteristics and gradation. Therefore, the resolution suggested by the technician is critical to observe porosity and damage characteristics.

The process of qualitatively inspecting porosity or damage in 2D slices is quite simple. For example, the CT scan provides an image stack. Placing the sample in an XYZ reference and moving along the axis allows us to observe the different components of asphalt mixture. Conversely, the 3D irregularity and complex structure of the cracks and voids in the asphalt pavement indicate that investigation in 2D can be inaccurate [126]. Considering that, different methods have been used to identify and reproduce 3D structure parameters. Lin et al. [127] used CT scanning images to build 3D models to evaluate voids in asphalt mixture using self-innovated software. Stereology [128] is a technique for determining porosity that is frequently used in 2D sections [126] and image analysis. Kim et al [46], employed CT slice pictures for this stereological procedure in their investigation. The CT virtual slicing method minimised errors and allowed a stereological comparison. The result revealed differences in porosity between slices, requiring a minimum of ten images to produce satisfactory results using the stereological approach.

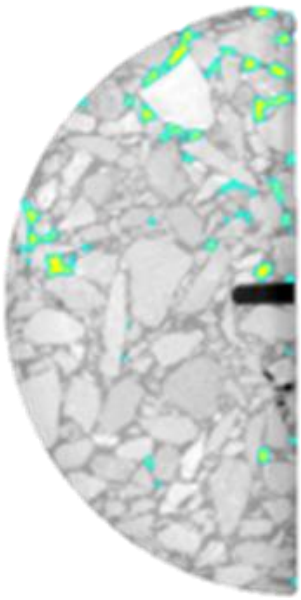

(a)

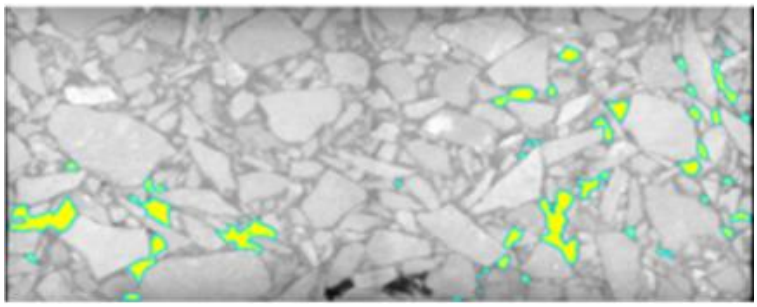

(b)

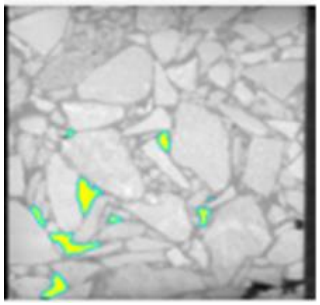

(c)

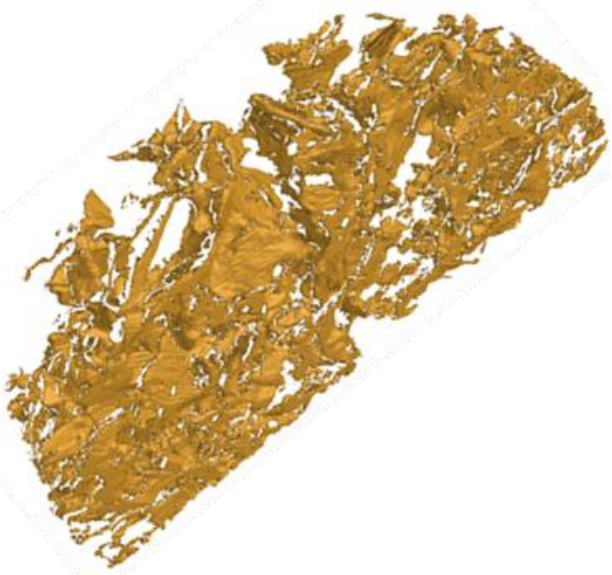

(d)

Figure 15: Asphalt mixture CT scan: pore analysis, top (a), front (b), left (c), perspective (d)

Quantitative analysis involves selecting pore spaces by image segmentation and delineating the margin between porosity and material using thresholding. After segmentation, a great deal of additional information is included beneath the visual representation of pore spaces in Figure 15. Quantitative analysis can determine the total volume, the surface area, the roundness, the circularity, the tortuosity, the Euler number, and the position and can project the area in all three axes and other parameters providing statistical analysis of the voids space [169].

2.7.3. Material detection

The CT images of asphalt mixture can be segmented into three parts based on the three components (voids, mastic, and aggregate) of asphalt mixture [111]. To correctly delineate and assign the sample it is necessary to use image segmentation. A limitation of a typical CT is that no differentiation is identified between different chemical species and ultimately, the unique brightness of each material is determined by the physical density. As a result, despite their chemical differences, different materials may result in similar grey values. In theory, it is possible to do the image segmentation between most materials using good resolution, although noisy data sets can interfere with the segmentation accuracy. The segmentation process is subjected to error due to the human choice of threshold, which could be wrongly selected or modified during analysis. A greyscale calibration can be used to determine CT density, allowing physical density measurements to be obtained directly from scan data. However, it requires greyscale recalibration after every scan-parameter change or variation in the CT system's intensity. To identify and separate each part of the asphalt mixture, an effective image segmentation process is necessary [8]. There are four steps in image segmentation: converting the image into greyscale (RGB to Gray), median filtering, contrast enhancement and threshold segmentation [129]. Grey-value calibration is usually required a reference object (phantoms) in the same scan along with the object being investigated. For example, Figure 16 shows

the separation of the different components such as aggregate, water, and air/voids. Due to its low attenuation coefficient for X-ray radiation, water identification has represented a challenge when analysing the presence within the material. As indicated in [111], the use of tracers in water in conjunction with photographs of saturated and dry asphalt concrete may be more effective for the investigation of water evaporation [130].

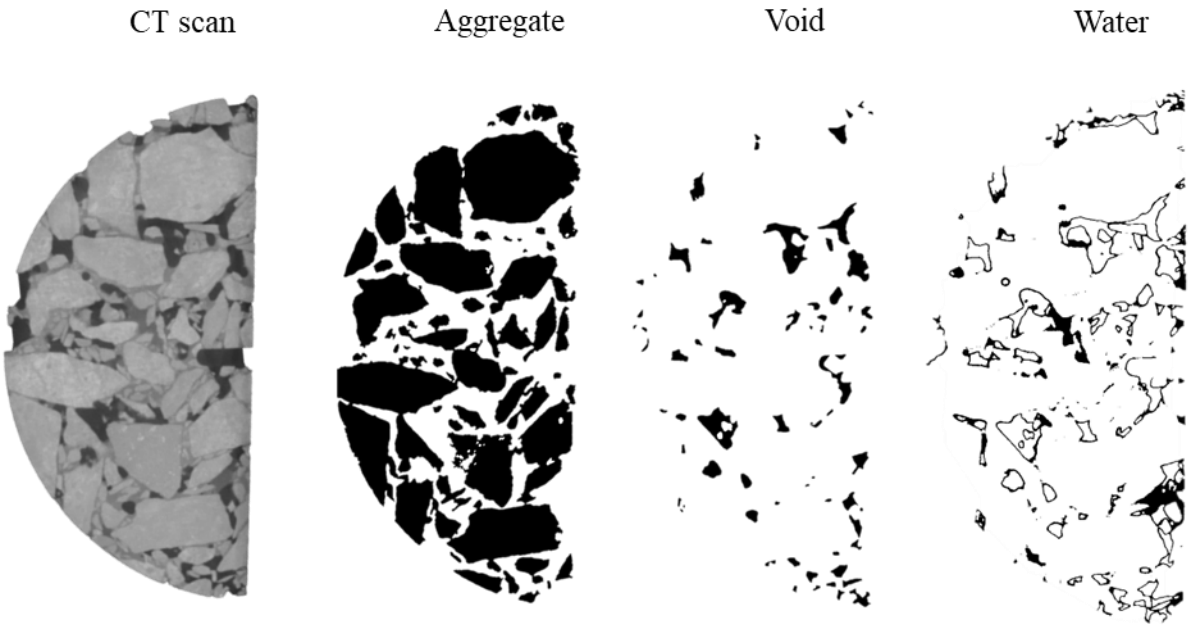

Figure 16: Asphalt mixture CT scan: components

2.7.4. Damage detection

Cracks are the most common observable structural damage in asphalt mixture [131]. Damage can also be caused by surface degradation, such as freeze-thaw damage, and internal swelling [112], [132]. X-ray CT has been used to detect asphalt mixture deterioration in the past, but the studies have been limited to experimental studies rather than in situ investigations. X-Ray CT is used for damage assessment and measuring crack tortuosity [111], in addition to deterioration under the freeze-thaw cycles as measured in [133]. With X-Ray CT, the interior breaking can now be visualised, as

illustrated in Figure 17 [134]. X-Ray CT can be used to detect the growth of the pores inside as well as their connection. X-ray CT scan helps find whether a that damage occurred inside or outside the object.

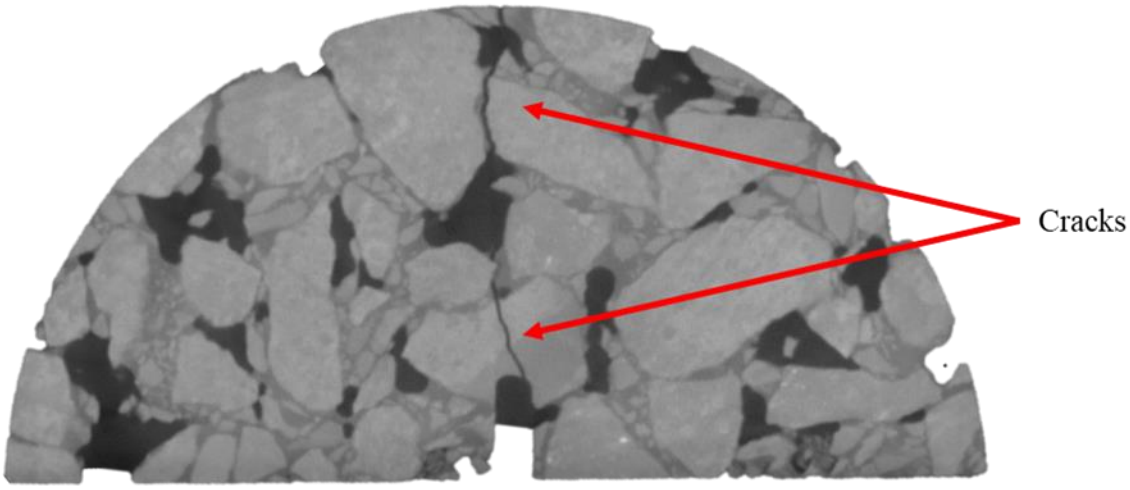

Figure 17: Asphalt mixture CT scan: Damage

2.7.5. Digital reconstruction of sample

Computational studies are frequently used for material properties forecast, analysing the structure properties, and learning how a material behaves. Simulating properties allows to adjust the degree of complexity and analyse one property independently, saving costs compared to experiments. However, simulations are often too computationally demanding or even impossible to run. Fortunately, both concerns are continually being addressed since CT provides enough detail to refine models using actual morphological inputs. In addition, computational resources have continually improved in recent years and will continue to provide a more efficient tool for analysis.

Mechanical simulation is one of the popular studies that used CT data and it is examined in more detail in the next chapters. Based on high-resolution CT images, micromechanical simulations of

structural mechanics can identify areas of potential failure and fracture formation around and between pores and aggregate [135]. Due to CT's resolution limitations, microscopic voids and small void connections and aggregate are undetectable in CT images, but bigger voids and the connection among them, such as in the asphalt mixture, can be evaluated.

2.8. Modelling

2.8.1. Numerical Modelling methods

The researcher [99], [100], [101] used various experimental tests to obtain a different range of mechanical and fracture characteristics of an asphalt mixture. These tests have pros and cons: the pro as in having a long-standing reputation of reliability, and the cons as they require expensive sampling and laboratory testing equipment as well as require a long time to complete. Due to the multiple mechanisms involved in fractures, such as microcracks, heterogeneities, grain boundaries, dislocations, and anisotropies, it is also difficult to analyse the mechanical and fracture properties using an experiment.

Computational models are efficient ways to solve the limitations of experiments. Asphalt mixture performances have also been determined via other studies aside from experiments and field tests. However, modelling the mechanical response and fracture behaviour of real materials is exceedingly complicated [20]. The interacting phases, the formation of micro and macro-cracks, and the propagation of cracks are all contributing factors in modelling asphalt mixtures [65], [66], [67].

Through studying different types of asphalt mixture and load conditions by computer models, researchers proposed characterisation equations to predict the behaviour of pavements in deformation. The following part summarises the main numerical model applied in the construction field highlighting the advantages and limitations. Numerical methods are divided into two categories:

discrete model and continuum model. These models include Discrete Element Methods (DEM) [20], Finite Element Methods (FEM) [88], Lattice Spring Model (LSM) [22] and Peridynamic (PD) [29] which will be introduced in the next section, see Figure 18.

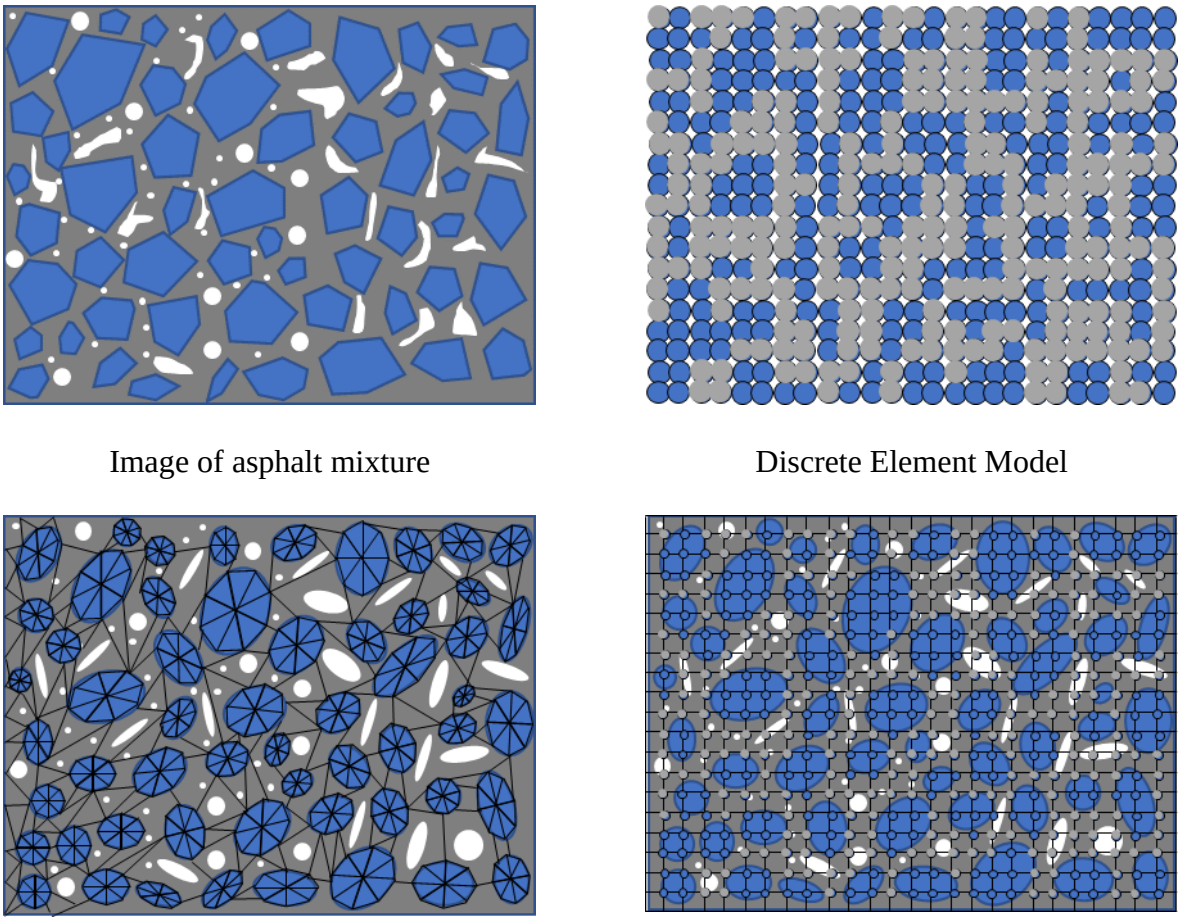

Figure 18: Simulation models: DEM, FEM (mesh based) and Peridynamic (mesh-free based)

To simulate the movements and interactions of stiff particle assemblies, Cunnall and Strack [136] developed a DEM representing bodies as discrete particles. The geometry and the mechanical interaction between particles can be represented in several ways. Buttlar et al. [24] use a polyhedron-based model to produce particle geometry, while [116] compute it using image-based models. Khateeb et al. [137] use DEM and image processing techniques to model the fracture resistance of

asphalt mixture. Nevertheless, rheological and fracture models of solids at different length scales can be difficult to implement in DEM. In addition, DEM's reliability depends on the accuracy of the input parameters (contact model) and the selected particle properties parameter chosen, which constituted a limitation on the effective application of the model [138].

The finite element method (FEM) is one of the most used numerical methods based on the partial differential equation of the classic continuum mechanism [88]. FEM, usually requires rigorous experiments under a variety of conditions, evaluating the material's macroscopic response, and fitting the mechanical responses with the continuum-based constitutive models. The finite element method is suitable for modelling structures with complicated geometries and diverse materials since it is robust in calculating stress fields. Each pavement component requires a bespoke modelling of the deformation behaviour [139]. The model provides a rigorous theoretical solution process to predict performance in a brief period and reduces computational expenditure. The results accuracy of the numerical techniques depends on the qualities and precision of the mechanical and fracture material used in these models which are frequently assumed rather than quantified.

FEM has the disadvantage of not explicitly examining the micromechanical behaviour of the mixture, making it difficult to correlate the tests result to the micromechanics of the material. The model is incapable of distinguishing dissimilarities at different scales and capturing specific fracture phenomena.

Mesh dependency is another common issue in FEM damage simulations [140], [141], [142]. The authors in [142] applied careful meshing around the crack tip avoiding the error in calculations. The FEM models the singular stress field of a crack by using a very fine mesh near the crack tip [143]. Special attention must be applied to eliminate mesh reliance when grids are refined. It can be alleviated to a part by giving different length scales. It is evident that in the FEM continuum classic model, a point is influenced by the nearest point. As a result, there is no internal length parameter

separating the various length scales. Furthermore, the classical continuum theory predicts no dispersion, despite opposite experimental evidence, leading to several investigations to address these weaknesses. The fracture must be predicted, and the assumptions make it impossible to investigate the damage. For instance, in [144], the authors studied the fracture performance using a 3D FEM model generated from CT scans of the asphalt mixture. Fracture behaviour was simulated by adding a conventional solid element where the phenomenon is predicted to occur. Despite this consideration, the simulated crack propagates as a straight line, contrary to observation during experiment [87] that indicates a twisty path propagation of cracks. In addition, in [16] the authors studied anti-cracking performance using a developed FEM model with polygonal random aggregate. The cohesive elements were added in aggregate, bitumen and interfaces. The cracks appear in the same location as the real asphalt mixture and propagate as a straight line as in [144]. As a result of this divergence between the simulation and experimental cracks, the fracture energy error between them was 22.9% for a 10 mm notch. The difficulties associated with modelling dynamic fracture processes are numerous; for instance, cohesive FEM or the XFEM need a damage criterion to determine when to branch the crack in addition to tracking stress around the crack tip.

The cohesive zone model, developed by Dugdale and Barenblatt [145], has grown popular among many other fracture criteria and has been adopted by Xu and Needleman [146] with the addition of cohesive zone features. Cohesive zone elements are placed between neighbouring in the mesh [147] to ensure crack traction across fracture surfaces after crack propagation, see Figure 19 (a). During the simulation, the fractures can take any course along the intersections of adjacent pieces. This technique removes all constraints associated with having a pre-determined crack path. Fracture paths, on the other hand, are very sensitive to mesh texture and alignment. Models of cohesive zones consist of discrete surface elements positioned between continuum regions. This results in the material reaction exhibiting both regular and cohesive zone elements, even though the cohesive zone elements are used

only to create fracture behaviour. As the mesh size decreases, the number of cohesive elements increases, while the size of the continuum area is the same. As result, as the mesh size decreases, the material properties soften. Mesh texture also produces anisotropy.

By utilizing the XFEM method introduced by Belytschko and Moes et al. [142], considerable progress has been made recently towards solving these problems. The XFEM can be used for crack growth and coalesces without remeshing [148] and through finite elements, cracks can pass anywhere with no restrictions on the direction of the new surface created by cracks, see Figure 19 (b) [149]. A priori information about how the solution behaves near discontinuities is incorporated into this method including damage models and branching criteria [150]. The approach reduces the additional degrees of freedom by only adding the nodes representing the elements that are divided by cracks. The elements that are adjacent to the crack tip are partly enriched and cannot be partitioned by unity, according to Zi et al. [150]. This leads to inaccurate solutions for the blending region. However, it is not known whether the method can be applied to situations involving fragmentation, multiple crack interactions, branching, and coalescence. XFEM was used in [151] with a heterogeneous model of SCB asphalt mixtures at -10 °C and 20 °C. Cracks occur realistically and the error is lower than observed in [16]. However, XFEM required a large cohesive element in the area of the predicted cracks. Other finite element techniques to model cracks and crack growth without remeshing includes the incorporation of discontinuities, a moving mesh, and an enrichment technique with minimal remeshing [152].

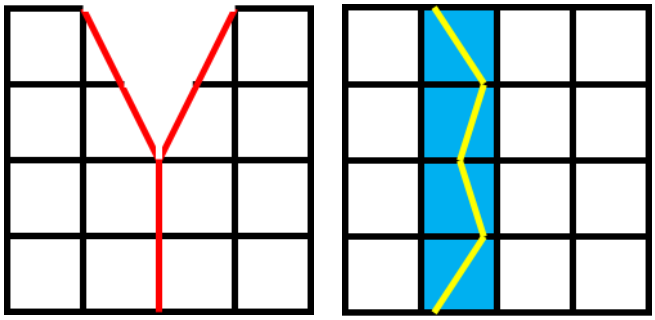

(a) (b)

Figure 19: Representation of crack propagation using FEM: (a) Cohesive zone model; (b) XFEM model

A classical continuum mechanic's equation of motion involves a differential equation that does not involve the derivatives associated with spatial displacement undefined in discontinuities [153]. Accordingly, classical continuum mechanics' solution forecast infinity in stress at the crack tips [153]. Therefore, the damage is treated separately by introducing an external criterion which is not part of the equations for the classical continuum mechanics. Additionally, the displacement field may be continuous before the damage is initiated but discontinues afterwards. Hence, in the context of the classical continuum mechanics model, the damage propagation and initiation required different treatments.

Simulation using the lattice spring model appears to be more effective than methods developed from classical continuum mechanics and overcomes the difficulties encountered in the methods [22]. Models of lattice springs represent materials consisting of discrete elements that interact through springs, or, more generally, rheological elements [154]. Lattice points can interact in either a short-range (local) with the nearest neighbours or via a long-range (nonlocal) by including far more neighbours [22]. In addition, there are several types of lattices such as triangular, square and honeycomb and they can be periodic or disordered [155]. These different lattices have directional

dependence upon elastic properties. Therefore, the interaction forces of one lattice differs from another type making it unclear to choose which is the best for specific problems.

2.8.2. Peridynamic

Silling [29] proposed the Peridynamic (PD) theory to resolve the restrictions and to accurately model and simulate dynamic fracture by using a meshless numerical approach based on the nonlocal continuum.

“Peridynamic” is derived from the Greek περί (peri) meaning “nearby,” and δύναμις (dynamics) meaning “force” [156]. Peridynamic uses the concept of the horizon to describe nonlocal interactions among material points within it [153]. The concept of Peridynamic extends to the continuum scale, so it can explain for example what happens physically at an atomic scale.

Peridynamic uses integral equations instead of differential equations. Peridynamic theory relies on nonlocal interactions between material points to explain internal forces, in which damage is a constitutive attribute model. Dissimilar materials have special properties at their interfaces, and damage can propagate where and when the conditions are favourable for it. This theory can replicate the micromechanics behaviour of materials and reproduce damage without the need for remeshing. Furthermore, the material failure incorporated into its constitutive relations does not require criteria for crack propagation or crack branching. Cracks are generated by an automatic bond-failure criterion that correlates with the energy release rate of the material and takes place spontaneously in this method. Many problems have been predicted using the peridynamic theory. Additionally, a new constitutive model is developed by Silling [30], [31] for viscoelastic and plastic materials. To link different length scales, peridynamic theory has been revealed to be a promising approach, with the benefit of being more realistic than the classic continuum theory since it considers material failure as

an inherent element of mechanical performance without relying on any external damage criteria [153].

This technique has been used to solve many static and quasistatic problems. Zaccariotto et al. [157] implement PD for static crack propagation problems. Shou et al [158] studied for polymethyl methacrylate (PMMA) specimens subjected to uniaxial compressive load the initiation, propagation, and coalescence of 3D pre-existing defects. Coupled formulations have been developed using PD to analyse thermal problems [159], diffusion [160] and porous flow [161].

In the peridynamic formulation, forces are integrated at a material point, linking deformation and force rather than strain and stress [29]. Hence it does not have the same types of numerical inconsistencies as classic continuum mechanics.

Peridynamic can be divided into two categories: (i) The Bond-based Peridynamic, in which force depending is limited to a single bond and hence has a fixed Poisson ratio of 0.25 in 3D and 0.33 in 2D and (ii) the State-based Peridynamic approach, which is developed to overcome the limitation of a fixed Poisson ratio, in which a particle's overall state within a material horizon determines the forces that bind two bonded elements, not just the single bond.

In this study, the simulations are based on the state Peridynamic models only, although the bond-based model is briefly discussed.

In the Peridynamic theory, see Figure 20, a non-deformed body, B_0, consists of a lattice made by particle P connected by bonds among them. For each particle is assigned a position x in the initial reference status for a non-deformed body, B_0 and for another particle P' a position x'.

Based on this reference configuration, the relative position vector of these two particles is defined by ε as follow

$$\varepsilon = x' - x \tag{22}$$

When a body is deformed, these particles have a different position in the body.

Therefore, the particle x assumes the new position y.

The relative displacement vector u of x is

$$u = y - x \tag{23}$$

In the same way, the particle P' displacement vector u' is

$$u' = y' - x' \tag{24}$$

The relative displacement η is identified as

$$\eta = u(x', t) - u(x, t) \tag{25}$$

The particles position in the deformed body are represented by the vector $\varepsilon + \eta$.

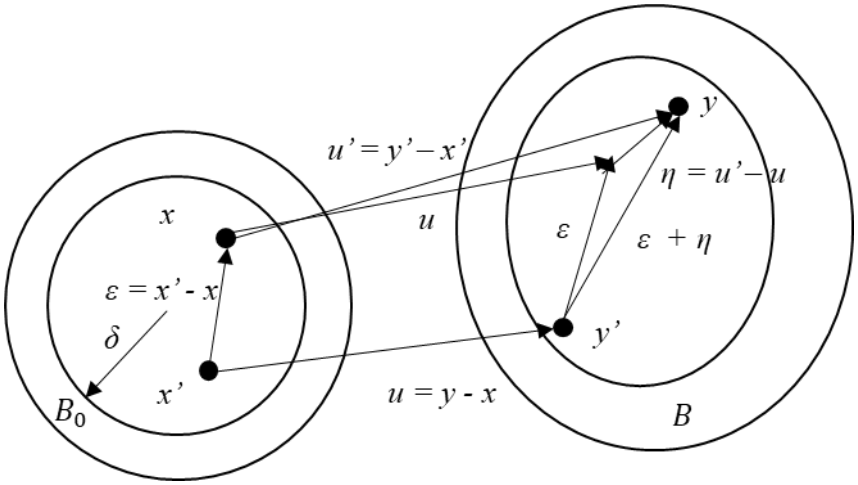

Figure 20: Deformation of the bond represented in [17, 18, 19, 20] and relation with the reference state ε, the deformation state η and the displacement state U

In addition, ε also represent the bond which need further descriptions.

Peridynamic posits that a bond that extends over a finite differs fundamentally from classical theory which relies on contact forces for its concept. According to the bond based Peridynamic theory, the force between two particles is unaffected by the states of the overall particles' and depends only on their own state. The force acting between particles is the pairwise force f depending only on the reference state of the body influenced only by η, ε described in (22) and (25).

$$f(\eta, \varepsilon) \tag{26}$$

In a horizon, particles x and x' are joined in a spring-like manner, corresponding to their mechanical properties. Particles x and x' are affected by the force:

$$f(\eta, \varepsilon) \;=\; f(\eta, \varepsilon)\, \frac{\varepsilon + \eta}{\|\varepsilon + \eta\|} \tag{27}$$

According to the latter equation, the vector of force between the particles is parallel to their current relative position.

Pairwise force describes the interaction among the material points which contains information associated with the constitutive properties' material. But the pairwise force must follow the linear and angular admissibility conditions which Silling examines in detail [29].

Therefore, the pairwise force f has these properties:

The first properties derived from conservation of linear momentum

$$f(-\eta, -\varepsilon) = f(\eta, \varepsilon) \ \forall \eta, \varepsilon \tag{28}$$

The second properties derived from conservation of angular momentum

$$(\varepsilon + \eta) \ x \ f(\eta, \varepsilon) = 0 \ \forall \eta, \varepsilon \tag{29}$$

Therefore, the response functions are nonlinear.

The f in the bond based peridynamic is not function of the time and it is not for plasticity or viscosity. The interaction between particles is given by the governing equations in Peridynamic defining the particle's acceleration at the time t and in the reference configuration at the position x is found from

$$\rho(x)\ddot{u}(x,t) = \int_{H_x} f(u(x',t) - u(x,t), x' - x)dV' + b(x,t) \tag{30}$$

where $\rho(x)$ is the density of the material at x, ü is the acceleration of x, H_x is the spherical neighbourhood of x containing all nodes x′ within the horizon δ, f is the pairwise force at time t, dV' is the infinitesimal volume; b is a body force density field.

The equation (27) and (30) describe the peridynamic model for a nonlinear micro-elastic material. The formulation does not allow rigid rotation because $\|\varepsilon + \eta\|$ is invariant under rotation of the body. Hence, these formulations are a simplification for many materials because result in fixed Poisson ratio of 0.25 for a 3D and 0.33 for 2D. Furthermore, in continuum mechanism the force is a stress tensor and the pairwise force function limits the use of peridynamic. In addition, this method does not include viscoelasticity or plasticity.

Therefore, introducing the concept of "force state," which is close to the idea of stress tensor, the method is improved in a new Peridynamic model called State based Peridynamic.

The state is defined with the convention used of the angle bracket $\langle\cdot\rangle$. As a generalization of a second-order tensor, vector states are operators whose images are vectors. An operator whose image is a scalar is also known as a scalar state. The governing equations in state based Peridynamic is like the bond based and given by (31)

$$\rho(x)\ddot{u}(x,t) = \int_{H_x} \left\{\underline{T}\,(x,t)\langle x' - x\rangle - \underline{T}(x',t)\langle x - x'\rangle\right\} dV' + b(x,t) \tag{31}$$

The force is defined differently with the state and is given by $\underline{T}\,(x,t)\langle x' - x\rangle$, the force vector state field at time t is the force vector per unit volume squared that particle x applied to the particle x' and called bond holding all interaction for all $\langle x' - x\rangle$.

The relative position vector state ε in the reference configuration of these two particles is given by

$$\underline{X}\,\langle x' - x\rangle = x' - x\ = \varepsilon \tag{32}$$

Where $\underline{X}$ stands for the reference state that maps all bonds in an undeformed body, B_0.

The relative displacement vector state $\underline{U}$ associating the bond by

$$\underline{U}\langle x' - x\rangle = u(x', t) - u(x, t) = \eta \tag{33}$$

The deformation state $\underline{Y}$, mapping all bonds into its deformed image, B, Figure 20, is given by

$$\underline{Y} = \underline{X} + \underline{U} = y' - y = \varepsilon + \eta \tag{34}$$

The equation (31) is integrated over the "horizon" (theoretically it can be infinite but, in practise it is finite). The horizon is a portion of material where the particles are interacting with each other, see Figure 21 .

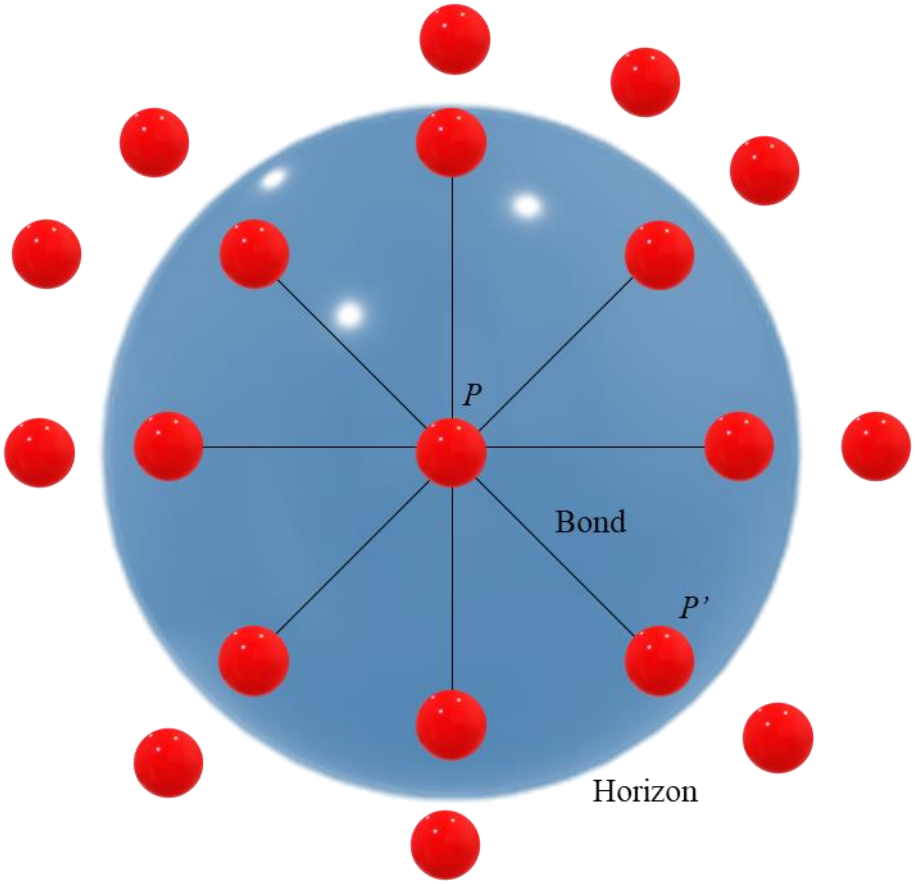

Figure 21: Schematic view of bonds within the horizon

The horizon is assumed to be a positive number unable to identified particle beyond this horizon as

$$|\varepsilon| > \delta \rightarrow f(\eta, \varepsilon) \ \forall \eta, \varepsilon \tag{35}$$

The choose of the horizon is linked with the intrinsic material length-scale. In many case the microstructure, boundary and loading condition led to impractical value of length-scale. In such cases, the user selects the horizon according to convenience, usually is chosen three time the lattice distance. Peridynamic solution converges to the classical elasticity solutions in the limit of the horizon going to zero.

The force scalar state for the linear elastic model is given by [29]-[31]

$$\underline{t} = \underline{t^i} + \underline{t^d} = \frac{3k\theta}{m} \underline{\omega}\, \underline{x} + \alpha \underline{\omega}\, \underline{e^d} \tag{36}$$

Where $\underline{t^i}$ and $\underline{t^d}$ are respectively the scalar volumetric and deviatoric state, *k* is the bulk modulus, $\underline{\omega}$ is the influence function called also scalar weighting function with argument the bond vector $\boldsymbol{\varepsilon}$ in the reference configuration [31], $\underline{x}$ is the reference position scalar state defined as $\underline{x}\langle\varepsilon\rangle = \|\varepsilon\|$, *m* is the weighted volume defined as $m = (\omega\, x) \cdot x$, θ is the scalar state volume dilatation of the neighbourhood *H* defined as $\theta = \frac{3}{m}(\underline{\omega}\, \underline{x})\underline{e}$, the extension scalar state $\underline{e}$ is defined as $\|\underline{Y}\| - \|\underline{X}\|$, therefore $\underline{e}$ is $\underline{e}^i - \underline{e}^d$ which $\underline{e}^i$ represents the spherical extension state as $\frac{\theta\|X\|}{3}$. $\underline{e^d}$ is the scalar deviator state part of the bond elongation defined as $\underline{e^d} = \underline{e} - \frac{\theta\|X\|}{3}$, and α is related to the shear modulus G as

$$\alpha = \frac{15\ G}{m} \tag{37}$$

The visco-elastic peridynamic model [30] describes the viscoelastic material according to a standard linear solid, schematised in Figure 22.

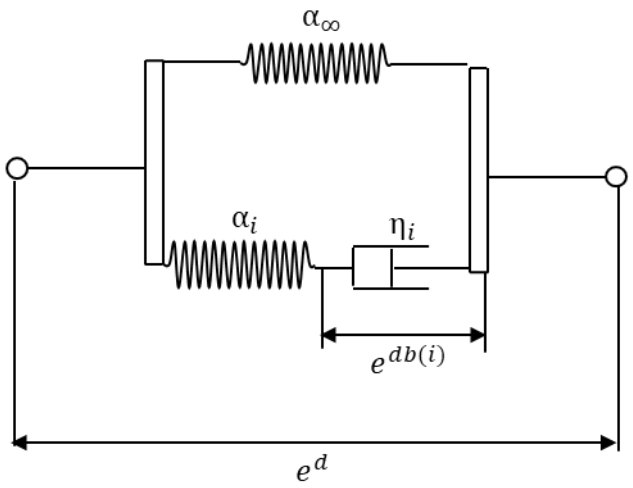

Figure 22: Standard linear solid model for visco-elastic peridynamic solid models

The scalar extension state $\underline{e}$ is divided into spherical part and deviatoric parts, standing respectively for the isotropic expansion and the deviatoric part. The latter part is made by elastic $\underline{e^{de}}$ and back extension $\underline{e^{db(i)}}$ parts

$$\underline{e^d} = \underline{e^{de}} + \underline{e^{db(i)}} \tag{38}$$

According to the last equation, the scalar force state $\underline{t}$ is given by

$$\underline{t} = \underline{t^i} + \underline{t^d} = \frac{3k\theta}{m}\underline{\omega}\,\underline{x} + (\alpha_\infty + \alpha_0)\underline{e^d} - \alpha_i\underline{\omega e^{db(i)}}) \tag{39}$$

The elastic parameter α is described as follows

$$\alpha = \alpha_\infty + \alpha_i \tag{40}$$

a_∞ is the elastic part and a_i is the relaxation moduli.

Normalising the relaxation moduli a_i as

$$\alpha_i = \alpha\, \lambda_i \tag{41}$$

Substituting (41) in (40) the elastic a_∞ is

$$\alpha_\infty = \alpha(1 - \lambda_i) \tag{42}$$

Where λ_i ranges between 0 and 1. When λ_i is close to 0, the model is elastic, and when it is close to 1 is viscoelastic [30].

The evolution equation of the scalar deviatoric force back extensions' dash poth is given by [30]

$$\underline{t^d}(t) = \underline{e_0^d}\left(\alpha_\infty + \alpha_i e^{\frac{-t}{\tau_i^b}}\right) \tag{43}$$

Where τ_i^b is a time constant.

The advantage method of Peridynamic for damage is the introduction of a breakage condition depending on the critical relative elongation, s_0, of bonds between material point at which they break.

The critical value s_0 for brittle materials derives from fracture energy for a particular material which is obtained from experiments.

Due to the sequential breaking points, Peridynamic crack form as surfaces between material points. The method does not require recording the cracks, unlike the continuum methods. In addition, no initiation crack criteria are required for damage such as branch, change direction, turn and coalesce. Additionally, Peridynamic can generate cracks spontaneously where none previously existed. For instance, in [162] its application is demonstrated for crack nucleation.

For elastic material, the energy stored within each body can be reversible at a critical energy release rate. Peridynamic relates the critical energy release with the damage. The energy can be associated with bonds and each of it has a micro potential $w(s)$ and defined as

$$f(\eta, \varepsilon) = \frac{dw}{d\eta}(\eta, \varepsilon)\ \forall \eta, \varepsilon \tag{44}$$

The micro potential is correlated to the strain energy which is the energy per unit volume in the body at a given point given by

$$W = \frac{1}{2}\int_{H_x} w\,(\eta, \varepsilon) dV' \tag{45}$$

The $\frac{1}{2}$ indicates the bond is shared between two particle and therefore energy.

The strain energy density measures the potential energy stored per unit volume when the material is deformed.

For an isotropic material, $c(\varepsilon)$ depends only on the bond length, $\varepsilon = |\varepsilon|$.

Bond failure is introduced to model fracture based on the bond's stretch, Figure 23, as defined by

$$s = \frac{\left\|\underline{Y}\langle x' - x\rangle\right\| - \left\|\underline{X}\langle x' - x\rangle\right\|}{\left\|\underline{X}\langle x' - x\rangle\right\|} = \frac{\|\eta + \varepsilon\| - \|\varepsilon\|}{\|\varepsilon\|} \tag{46}$$

This definition allows a breakage of bonds after it is stretcher over limit fixed.

$$f = cs \tag{47}$$

c is the spring constant.

$$\varphi(\boldsymbol{x}, t) = \frac{1 - \int_{H_x} \mu(\boldsymbol{x}, t, \varepsilon) dV_\varepsilon}{\int_{H_x} dV_\varepsilon} \tag{48}$$

where μ is the damage function which is history dependent and it takes a value of 0 or 1, i.e.

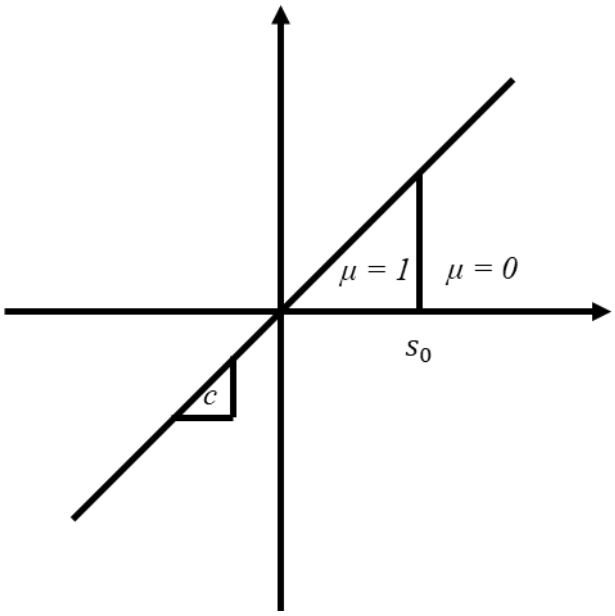

Figure 23: Bond related with the displacement

$$\mu(t,\varepsilon) = \begin{cases} 1 \; if \; s(t',\varepsilon) < s_0 \;\; \forall \, 0 \le t' \le t \\ 0 \qquad\qquad\qquad\qquad otherwise \end{cases} \tag{49}$$

Where 0 is the unbroken material and 1 is a complete bond breakage, see Figure 24.

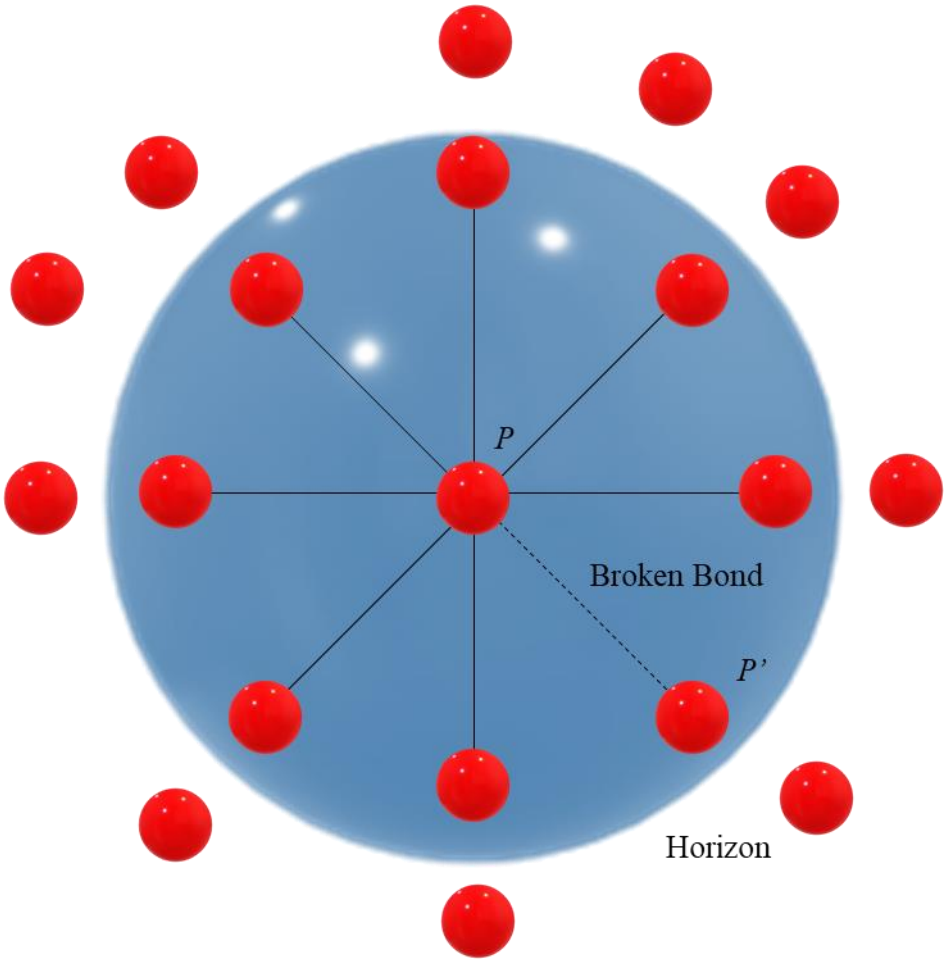

Figure 24: Schematic view of broken bond

Therefore, damage is calculated as the fraction between the number of broken bonds and the number of initial bonds.

The breaking of the bond reduces the load sustained and thus lowers the stiffness. The result may be the spread of damages to the entire body and the creation of a coalescing of broken bond across the surface.

The force state derives from the strain energy density as follow:

Substituting (46) in (47), we obtain

$$f = c\,\frac{\|\eta + \varepsilon\| - \|\varepsilon\|}{\|\varepsilon\|} \tag{50}$$

The strain energy density is rewritten as

$$w = c\,\frac{\eta^2}{2\,\varepsilon} = c\,\frac{s^2\varepsilon}{2} \tag{51}$$

And substituting in equation (45)

$$W = \frac{1}{2}\int_{H_x} w\,(\eta, \varepsilon)dV' = \frac{\pi\, c\, s^2\delta^2}{4} \tag{52}$$

Considering that in classic continuum theory

$$W = \frac{9\,k\,s^2}{2} \tag{53}$$

Combining (52) and (53) results

$$c = \frac{18\,k}{\pi\delta^4} \tag{54}$$

The critical stretch, s_0, is related with bond energy. Indeed, two halves of body completely broken needed a breakage of all bonds.

$$w(\varepsilon) = \int_0^{s0} f(s)\, \varepsilon ds \tag{55}$$

To evaluate the integral, it is used the spherical coordinates, see Figure 25. Considering equation (51), the work G_0 needed for the break of bonds per unit area is

$$G_0 = \int_0^{\delta} \int_0^{2\pi} \int_z^{\delta} \int_0^{\cos^{-1}\frac{z}{\varepsilon}} c\, \frac{s^2 \varepsilon}{2} \varepsilon^2 \sin\phi \, d\phi \, d\varepsilon \, d\theta \, dz \tag{56}$$

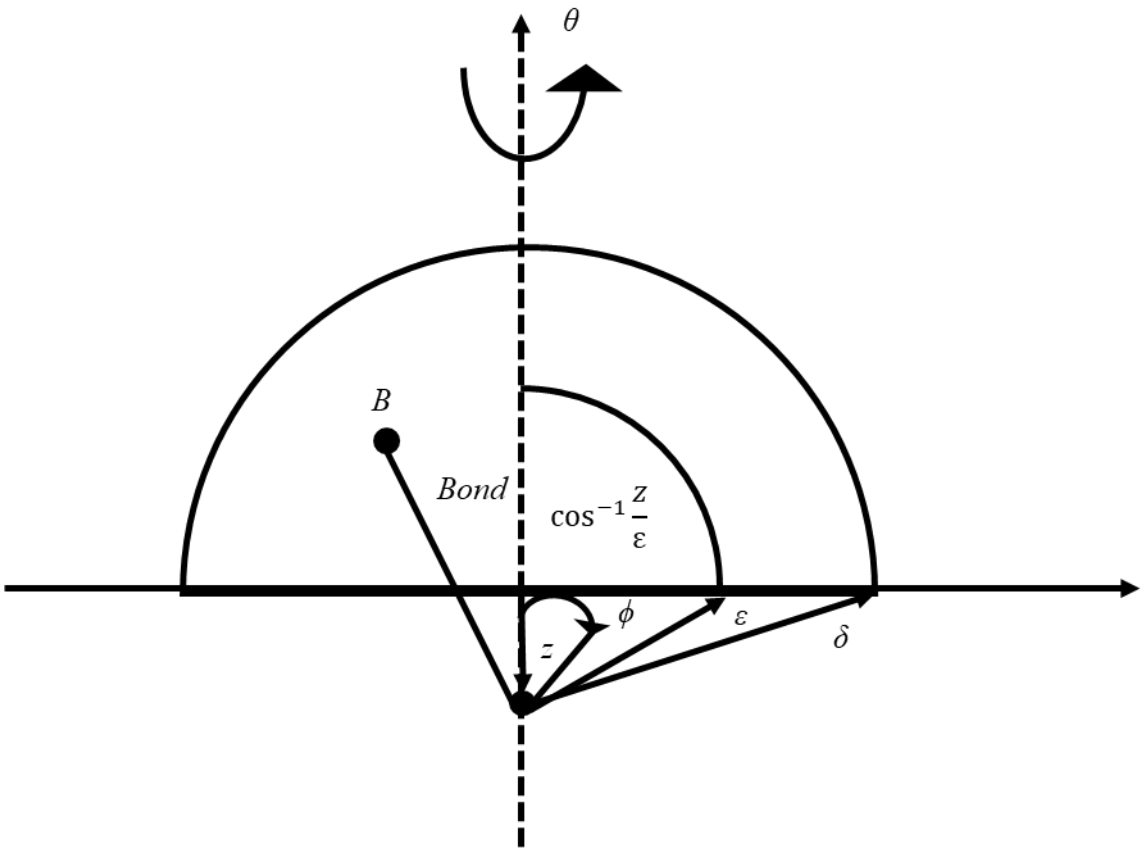

Figure 25: Energy of bond G_0

Solving the integral equation (56) for complete separation of the two halves of the body, the energy per unit fracture area is calculated as

$$G_0 = \frac{\pi\, c\, {s_0}^2 \delta^5}{10} \tag{57}$$

In brittle materials, the energy release rate can be measure, (57) can be used to determine s_0 under the assumptions that fracture surfaces are completely separated and the absence of additional dissipative mechanisms near the crack tip. Solving (57) for s_0 and using (54) leads to the critical value s_{00} is defined as [153]

$$s_{00} = \sqrt{\frac{5\pi\, G}{9\, K\, \delta}} \tag{58}$$

It is important to note that a bond is broken when s is greater than a critical value s_0, making the model history dependent. The value of s_0 varies during the simulations as the damage of the bonds is updating.

The damage criterion is better modelled by having the value be variable for materials like mastic since it is an independent parameter from other conditions, like compression. Therefore, the damage criterion is better modelled if the value is variable as follow

$$s_0(t) = s_{00} - \alpha s_{min}(t) \tag{59}$$

Where s_{00} is a constant and s_{min}, the current minimum stretch among all bonds connected to a given material point [153]

$$s_{min}(t) = min\left\{\frac{\left\|\underline{Y}\langle x' - x\rangle\right\|(t) - \left\|\underline{X}\langle x' - x\rangle\right\|}{\left\|\underline{X}\langle x' - x\rangle\right\|}\right\} = \frac{\|\eta + \varepsilon\|(t) - \|\varepsilon\|}{\|\varepsilon\|} \quad (60)$$

Damage is therefore modelled in terms of irreversible breakage of interactions in the constitutive model. Each material point's displacement, together with the distance between each material point, is calculated and monitored during the solution process. Compared to classical continuum-based methods, damage in the material is thus simulated in a better and more realistic manner. As a result of broken interactions aligning along cracks, the deformation may appear discontinuous across these cracks, while the integral equations remain valid.

2.9.2.1. Short range

Using the Peridynamic formulation, the particles are connected through bond forces via a predefined bond configuration within the horizon defined in Equation (31). Particles without bonds are therefore free particles that do not interact. Occasionally, the bodies may initially be positioned farther apart than the horizon, but eventually, come into contact. As part of the Peridynamics, short-range forces are employed to resolve contact forces [153].

To prevent penetration other than physical, repulsive forces are experienced between approaching bodies during the short-range contact approach. This approach determines the interaction between two points based on their positions relative to each other. Therefore, it is capable of handling large deformations as well as high-velocity impacts [153].

An approaching body makes contact when its relative distance from one of its materials points exceeds a predefined distance. The predefined contact distance of a model is normally chosen to be less than or equal [163] to the lattice of the whole model, to avoid contact turbulence. Therefore, short-range force is assigned between the particles and defined as follow

$$f(\eta, \varepsilon) = \frac{\eta + \varepsilon}{\|\eta + \varepsilon\|} \min\left\{0, \frac{c_s}{\delta}(\|\eta + \varepsilon\| - d_s)\right\} \quad (61)$$

where c_s is the stiffness.

The stiffness is 15 times the bulk modulus k of the impacting body [163]. The short-range force is only repulsive as defined in (61).

d_s is the contact distance that defined the condition if the contact forces are established among particles (62).

$$d_s = \min\{0.9\ \|\mathrm{x}' - \mathrm{x}\|, 1.35\ (r_s + r_s')\} \quad (62)$$

where r_s is defined as the particle's radius which is half of the lattice constant.

Chapter 3

Methodology

The literature review revealed that there was no computational study using Peridynamic to model the mechanical and fracture properties of asphalt mixtures. This chapter illustrates the research methodology and modelling concepts used to generate the framework. The methodology was structured into following five parts, (Figure 26): experimental test on asphalt mixtures and mastics, Computational Tomography (CT) of asphalt mixture samples and image elaboration, creations of digital asphalt mixtures, simulation using Peridynamics.

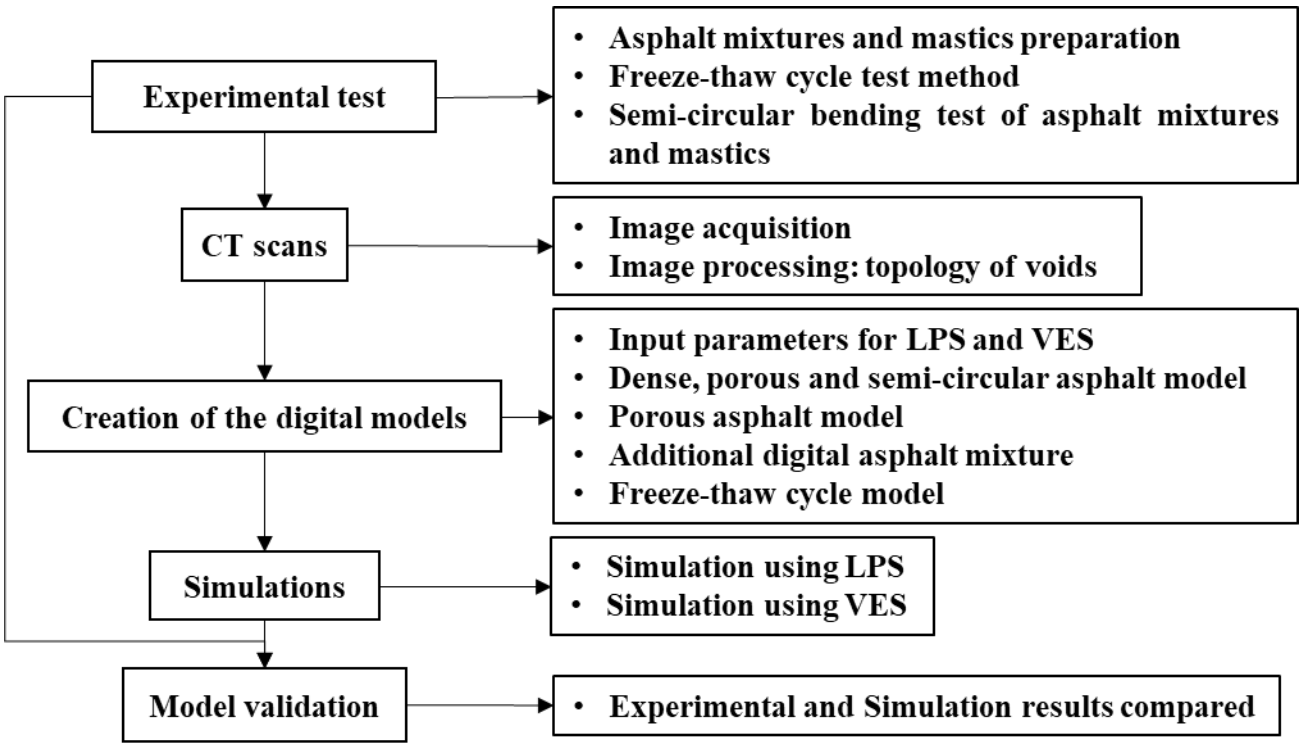

Figure 26: Methodology flow chart

3.1. Experimental test on asphalt mixture and mastic

To understand the influence of air void content, aggregate gradation, temperature and Freeze-Thaw cycles on the mechanical and fracture properties, different types of asphalt mixtures, namely: dense (3-5% void content) [91], semi-dense (10-13% void content) [164] and open (14-21% void content) [91] were manufactured. In 5.2, the methodology illustrates the asphalt mixture's preparation and testing. To obtain the input values for the peridynamic model simulations, mastics were manufactured with the same composition as the asphalt mixtures. In 6.3, the methodology illustrates the asphalt mixture and mastics' manufacturing procedure. The asphalt mixtures and mastics were evaluated at -10 °C and 20 °C to obtain their mechanical and fracture properties. For each type of asphalt mixtures and mastic, four samples [183] were tested at -10 °C and 20 °C. The temperature of -10 °C was the lowest available in the laboratory and lower enough to consider the asphalt mixture as elastic [56] and 20 °C is the highest suitable temperature for the test equipment. For higher temperatures the Hamburg wheel tracking test (50°C) is suggested. In 5.2.3, the methodology paragraph illustrates the semi-circular bending test procedure.

The asphalt mixtures were subjected up to 20 freeze-thaw cycles. According to the experimental result and topology of void analysis, further freezing cycle were not provide any changes on the asphalt performance and on the internal structure evolution. A similar observation to other studies [91], [96]. In 5.2.2, the methodology paragraph illustrates the freeze-thaw cycle procedure.

3.2. Computer Tomography of asphalt mixture and image elaboration

The asphalt mixtures were selected with the lowest air void content error according to [165] and scanned using a Phoenix v|tome|x L 300 micro-CT scanner. The utilised image resolution was selected to visualise the water content and to distinguish it from mastic. The procedures are discussed in Chapter 5 and 6. The images were elaborated using VG studio max [166] to separate the asphalt

mixture's components such as aggregate, mastic, water and voids and to identify cracks and internal structure changes. The CT images stack is automatically thresholded to convert to binary, where the black areas represent the voids and white areas represent the aggregate, see Figure 27.

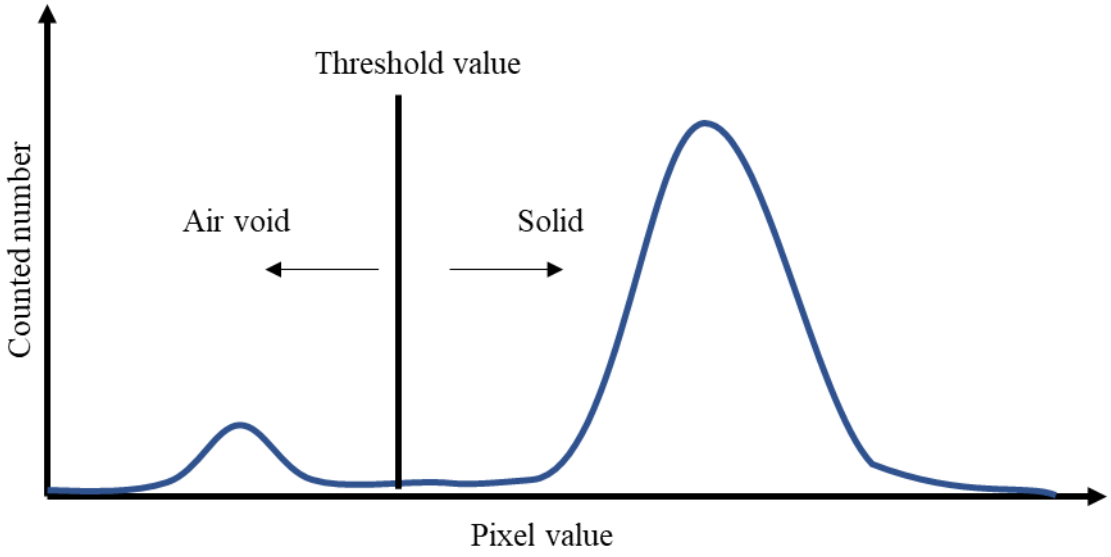

Figure 27: Histogram of pixel value

The stacked asphalt mixture' CT images and the individual identified, and isolated components were analysed with open-source ImageJ software (v1.8.0) [167] to determine the voids and aggregate topology and cracks. The topology of voids was calculated using Fiji's particle analyser plugin in ImageJ. The procedure is further described in Chapters 5 and 6.

3.3. Creation of the digital models

The asphalt mixture's component images for dense, porous and semi-circular asphalt mixture obtained with VG studio max [166] were processed using MATLAB. The MATLAB script converted the pixel in each image into coordinates. The images of the aggregate, void and water were uploaded to the script, which identifies the pixel position in the images assigning the type of material and coordinates. The results were compiled into a text file that includes all information needed by the

simulation software (LAMMPS) and the model used. Additional digital models were obtained with MATLAB filling partial voids with mastic or ice particle. In 6.3.3, the methodology describes the additional digital model production procedure.

The input parameters required for the simulations were calculated from the experimental results on mastic at -10 °C and 20 °C, the aggregate and interface values were obtained from the literature. In Chapter 6, the methodology describes the procedures to obtain the peridynamics input parameters.

3.4. Simulation

The compression test is conventionally used to obtain the stiffness and the strain at cold temperature. The semi-circular bending test is used to obtain both mechanical and fracture properties of asphalt mixture at cold and high temperature. The compression and the semi-circular bending test were simulated to assess the model's ability to replicate respectively the asphalt mixture bearing capacity. The compression and semi-circular bending tests were replicated by placing the digital sample in a simulation box. The compression test simulation was performed on a thin plate asphalt mixture model. The In Chapter 4, the methodology describes the model procedure and data analysis. The semi-circular bending test simulation was performed on a 3D digital asphalt mixture model. In Chapter 6, the methodology describes the model procedure and data analysis.

3.5. Model validation

The peridynamics model was validated by comparing the result of the experimental test on the bitumen beam at -10 °C with the simulation results (Chapter 4).

The developed digital asphalt mixtures were validated by calculating the relative error between the experimental and digital sample air void content (Chapter 6). The peridynamics models were validated by comparing the result of the experimental test on asphalt mixture at -10 °C and 20 °C.

Chapter 4

Combined peridynamics and discrete multi-physics to study the effects of air voids and freeze-thaw on the mechanical properties of asphalt

In this Chapter the Peridynamic and Discrete Multi-physics model is used to simulate the asphalt mixture performance under compression at low temperature and freezing condition. The process to obtain the digital sample from CT scan is provided. The simulation of bitumen at -10 °C is carried out as validation of the approach. The capabilities of the combined models to simulate asphalt mixture's mechanical and fracture properties are investigated.

This chapter has been published in *MDPI* as:

D. Sanfilippo, B. Ghiassi, A. Alexiadis, A.G. Hernandez, Combined peridynamics and discrete multiphysics to study the effects of air voids and freeze-thaw on the mechanical properties of asphalt, Materials (Basel). 14 (2021).

My contributions in this work were: Conceptualisation, Designed the work and performed the simulations, Methodology, Validation, Writing the original draft, Reviewing and Editing.

I would like to thank all the authors who have contributed to this work.

materials

MDPI

Article

Combined Peridynamics and Discrete Multiphysics to Study the Effects of Air Voids and Freeze-Thaw on the Mechanical Properties of Asphalt

Danilo Sanfilippo [1,2], Bahman Ghiassi [1,*], Alessio Alexiadis [2,*] and Alvaro Garcia Hernandez [1,*]

[1] Department of Civil Engineering, University of Nottingham, NG7 2RD, Nottingham, UK; danilo.sanfilippo@nottingham.ac.uk
[2] School of Chemical Engineering, University of Birmingham, B15 2TT, Birmingham, UK
* Correspondence: bahman.ghiassi@nottingham.ac.uk (B.G.); alvaro.garcia@nottingham.ac.uk (A.A.); A.Alexiadis@bham.ac.uk (A.G.H.)

Abstract: This paper demonstrates the use of peridynamics and discrete multiphysics to assess micro crack formation and propagation in asphalt at low temperatures and under freezing conditions. Three scenarios are investigated: (a) asphalt without air voids under compressive load, (b) asphalt with air voids and (c) voids filled with freezing water. The first two are computed with Peridynamics, the third with peridynamics combined with discrete multiphysics. The results show that the presence of voids changes the way cracks propagate in the material. In asphalt without voids, cracks tend to propagate at the interface between the mastic and the aggregate. In the presence of voids, they 'jump' from one void to the closest void. Water expansion is modelled by coupling Peridynamics with repulsive forces in the context of Discrete Multiphysics. Freezing water expands against the voids' internal surface, building tension in the material. A network of cracks forms in the asphalt, weakening its mechanical properties. The proposed methodology provides a computational tool for generating samples of 'digital asphalt' that can be tested to assess the asphalt properties under different operating conditions.

Keywords: asphalt; mathematical modelling; peridynamics; discrete multiphysics

Citation: Sanfilipo, D.; Bahman, G.; Alexiadis, A.; Hernandez Garcia, A. Combined Peridynamics and Discrete Multiphysics to Study the Effects of Air Voids and Freeze-thawon the Mechanical Proper-Ties of Asphalt. *Materials* **2021**, *14*, 1579. https://doi.org/10.3390/ma14071579

Academic Editors: Gilda Ferrotti and Francesco Canestrari

Received: 28 December 2020
Accepted: 16 March 2021
Published: 24 March 2021

1. Introduction

Asphalt, a heterogeneous mixture of aggregates, fillers and asphalt binder, is one of the most used infrastructure material. Asphalt's mechanical properties are influenced by the properties of its constituents, its internal structure and the loading and environmental conditions during its service life. Understanding the degradation of asphalt, such as rutting, ravelling, freezing, strength loss and fatigue cracking, is important for better design, manufacture and maintenance of roads.

One of the major sources of deterioration of asphalt is cracking. The fracture process can be divided into two different stages [1,2]: crack initiation and propagation. Crack initiation occurs when the mechanical stress is higher than a given limit, and micro-cracks occur in the mastic [3]. Under continuous load, these micro-cracks coalesce into macro-cracks, which initiate the propagation phase that ultimately, leads to failure [1]. The growth of microcracks damages asphalt irreversibly and increases maintenance costs [4], and this is influenced by different factors such as temperature, loading level and rate, fatigue and mixture composition.

Another cause of asphalt failure in cold regions is thermal cracking (at low temperatures), which may significantly reduce the durability of pavements [5,6]. This damage is especially severe when water is present in the asphalt pores due to its comparatively high thermal expansion. Under icing temperatures, the internal pore structure in an asphalt

mixture may change following a three-stage process [7]: (i) water expansion, which causes damage, and expansion of the exiting pores; at −10 °C, for instance, water undergoes 15% volume expansion [8]; (ii) cracking and merging of the pores and (iii) creation of new voids [9]. This phenomenon is especially intense in asphalts with a porosity between 6% and 13%, which retain part of the pore water. Asphalts with <6% voids have close pores that prevent water penetration, while asphalts with >13% voids have large pores that do not retain water [10–12].

There are many studies, both theoretical and experimental, on asphalt degradation (e.g., [3,4,13–16]), but only a few experimental works dedicated to low temperatures and freeze-thawcycles [5–7,17–19]. Furthermore, the experimental tests cannot show the evolution of the damage inside the asphalt's microstructure, which is critical for understanding the deterioration mechanisms. To the best of our knowledge, there are also no available numerical methods for predicting degradation of asphalt or monitoring the damage progression resulting from freeze-thawactions. The development of such modelling tools, the subject of this paper, allows estimation of asphalt's service life performance under cold environmental conditions. This is critical for optimising asphalt or developing novel materials with enhanced durability and long-term performance.

Recent advancements in computer technology allow performing realistic simulations of the performance of materials across scales. Novel mesh-free methods are more suited for this purpose as they allow simulation of crack propagation and branching without the need for mesh regeneration. One of the simplest mesh-free methods is the lattice spring model (LSM) that divides solids into computational particles linked together with springs [20–22]. Peridynamics (PD) [23] is a novel mesh-free method developed as an improvement of the LSM [24] to allow better simulation of the material damage response. The application of PD to the simulation of damage in construction materials is highly innovative and limited, and its asphalt application will be presented in this paper for the first time.

This paper aims to develop a computational tool that allows realistic simulation of the damage of asphalt under mechanical and freeze-thawloads. We present a PD model coupled with discrete multiphysics developed in the LAMMPS molecular dynamics simulation package. This requires developing realistic models considering the aggregates and binder, voids and water, both in liquid and solid forms. Optical and micro-CT images are used to develop models considering the internal microstructure of a range of asphalt materials. PD implemented in LAMMPS also allows considering the plastic [25] and viscoelastic [26] response of materials and is therefore suitable for simulation of the response of asphalt materials under higher temperatures. The state-based Peridynamics is used here to evaluate the mechanical response of intact asphalt before and after being subjected to a freeze-thawcycle. The internal damage in the asphalt due to freezing is simulated by coupling Peridynamics with repulsive forces obtained from expansion of liquid phases and their transformation into solid phase using Discrete Multiphysics (DMP) [27–29]. The model is then used to discuss the effect of the freezing of the water present in the voids on the asphalt's mechanical response.

2. Theory

2.1. Peridynamics

In Peridynamics, the material's body is defined as a lattice, and contrary to classical continuum mechanics, its behaviour is defined through a constitutive equation that links deformation and force rather than strain and stress. The original bond-based Peridynamic approach [23] was limited to materials with a Poisson ratio ¼ in 3D and ⅓ in 2D. State-based Peridynamics [30] was introduced to overcome these limitations. In state-based Peridynamics, the forces that connect two bonded elements depend on the overall state of all the particles located within a material horizon rather than the single bond. The acceleration of any particle at position x in the reference configuration at time t is found from:

$$\rho(\mathbf{x})\ddot{u}(\mathbf{x},t) = \int_{H_x} \{\underline{T}(\mathbf{x},t)\langle \mathbf{x}' - \mathbf{x}\rangle - \underline{T}(\mathbf{x}',t)\langle \mathbf{x} - \mathbf{x}'\rangle\} dV' + \mathbf{b}(\mathbf{x},t) \quad (1)$$

where $\rho(\mathbf{x})$ is the mass density at $\mathbf{x}$, $\mathbf{u}$ is the displacement vector field, H_x is a neighborhood of $\mathbf{x}$ with radius δ containing all the points $\mathbf{x}'$ within the horizon, $\underline{T}(\mathbf{x},t)\langle \mathbf{x}' - \mathbf{x}\rangle$ is the pairwise force state function at time t whose value is the force vector (per unit volume squared) acting between two particles within the horizon applied to the bond $\langle \mathbf{x}' - \mathbf{x}\rangle$, dV' is the infinitesimal volume, $\mathbf{b}$ is a body force density field. The relative position vector state of these two particles in the reference configuration $\boldsymbol{\varepsilon}$ is given by

$$\underline{\mathbf{X}}\langle \mathbf{x}' - \mathbf{x}\rangle = \mathbf{x}' - \mathbf{x} = \boldsymbol{\varepsilon} \quad (2)$$

where $\underline{\mathbf{X}}$ represents the reference state, mapping all bonds in a non-deformed body, B_0. The relative displacement vector state $\underline{\mathbf{U}}$ is associated with the bond by:

$$\underline{\mathbf{U}}\langle \mathbf{x}' - \mathbf{x}\rangle = u(\mathbf{x}',t) - u(\mathbf{x},t) = \boldsymbol{\eta} \quad (3)$$

The deformation state $\underline{\mathbf{Y}}$ expressed in Equation (4) maps all bonds into its deformed image, $\mathbf{B}$, Figure 1.

$$\underline{\mathbf{Y}} = \underline{\mathbf{X}} + \underline{\mathbf{U}} = \mathbf{y}' - \mathbf{y} = \boldsymbol{\varepsilon} + \boldsymbol{\eta} \quad (4)$$

Material behaviour is modelled by spring-like bonds between particles $\mathbf{x}$ and $\mathbf{x}'$ within the horizon. The force acting on particles $\mathbf{x}$ and $\mathbf{x}'$ is:

$$\underline{T}\langle \mathbf{x}' - \mathbf{x}\rangle = \underline{f}\langle \mathbf{x}' - \mathbf{x}\rangle \frac{\boldsymbol{\varepsilon} + \boldsymbol{\eta}}{\|\boldsymbol{\varepsilon} + \boldsymbol{\eta}\|} \quad (5)$$

where $\underline{f}$ is the scalar part of the force state named the force modulus state.

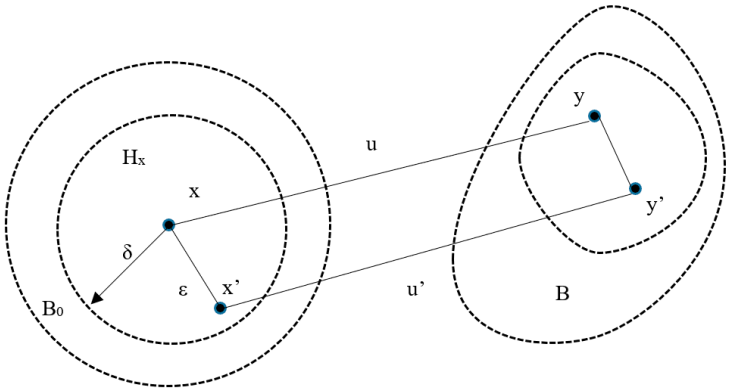

Figure 1. Deformation of the bond involved in (4) and in relation to the reference state $\boldsymbol{\varepsilon}$, the deformation state $\boldsymbol{\eta}$ and the displacement state $\underline{U}$.

The force scalar state is given by [25,31]:

$$\underline{f} = \frac{3K\theta}{m}\underline{\omega}\,\underline{x} + \alpha\underline{\omega}\,\underline{e^d} \quad (6)$$

where $\underline{\omega}$ is a scalar weighting function called the influence function whose argument is the bond vector $\boldsymbol{\varepsilon}$ in the reference configuration [31], $\underline{e}$ is the extension scalar state defined as $\underline{e} = \|\underline{\mathbf{Y}}\| - \|\underline{\mathbf{X}}\|$, $\underline{x}$ is the reference position scalar state defined as $\underline{x}\langle \boldsymbol{\varepsilon}\rangle = \|\boldsymbol{\varepsilon}\|$, m is the weighted volume defined as $m = (\underline{\omega x})\cdot\underline{x}$, θ is the scalar state volume dilatation of the neighbourhood H defined as $\theta = \frac{3}{m}(\underline{\omega}\,\underline{x})\underline{e}$, $\underline{e^d}$ is the scalar deviator state component of the bond elongation defined as $\underline{e^d} = \underline{e} - \frac{\theta\|X\|}{3}$, K is the bulk modulus and α is related to the shear modulus G as:

$$\alpha = \frac{15\,G}{m} \quad (7)$$

To model fracture, we introduce the notion of bond failure in relation to the bond's stretch s defined by:

$$s = \frac{\left\|\underline{\mathbf{Y}}\langle \mathbf{x}' - \mathbf{x}\rangle\right\| - \left\|\underline{\mathbf{X}}\langle \mathbf{x}' - \mathbf{x}\rangle\right\|}{\left\|\underline{\mathbf{X}}\langle \mathbf{x}' - \mathbf{x}\rangle\right\|} = \frac{\|\boldsymbol{\eta} + \boldsymbol{\varepsilon}\| - \|\boldsymbol{\varepsilon}\|}{\|\boldsymbol{\varepsilon}\|} \quad (8)$$

The breakage rule is that when s is larger than a critical value s_0, the bond breaks and is removed from the body. The critical value s_0 is defined as [32]:

$$s_0 = \sqrt{\frac{5\pi\, G_0}{9\, K\, \delta}} \quad (9)$$

where G_0 is the fracture energy. The value of s_0 is not constant, but varies during the simulations based on its damage defined as:

$$\varphi(\mathbf{x}, t) = \frac{1 - \int_{H_x} \mu(\mathbf{x}, t, \varepsilon) dV_\varepsilon}{\int_{H_x} dV_\varepsilon} \quad (10)$$

where μ is a history dependent damage function that takes on a value of 0 or 1, i.e.,:

$$\mu(t, \varepsilon) = \begin{cases} 1 \text{ if } s(t', \varepsilon) < s_0 \ \forall\, 0 \le t' \le t \\ 0 \qquad\qquad \text{otherwise} \end{cases} \quad (11)$$

For materials such as mastic, s_0 depends on s_{min}, the current minimum stretch among all bonds connected to a given material point [30]:

$$s_0(t) = s_{00} - \alpha s_{min}(t) \quad (12)$$

where s_{00} is a constant and:

$$s_{min}(t) = \min\left\{\frac{\left\|\underline{Y}\langle x' - x\rangle\right\|(t) - \left\|\underline{X}\langle x' - x\rangle\right\|}{\left\|\underline{X}\langle x' - x\rangle\right\|}\right\} = \frac{\|\eta + \varepsilon\|(t) - \|\varepsilon\|}{\|\varepsilon\|} \quad (13)$$

2.2. Modelling of Ice

To model ice, we take advantage of the flexibility of particle methods that can easily combine with other particle-based potentials in the context of discrete multiphysics. In this way, it is possible to extend the range of application of a single method by introducing potentials typical of other particle methods. This technique has been successfully used in several fields including fluid–structure interactions [33–35], solidification/dissolution [36,37], biological flows [38–40] and even machine learning [41,42]. In the case under investigation, we do not model water as a fluid. We are only interested in the pressure that expanding (i.e., freezing) water exerts on the asphalt structure. This can be achieved by a repulsion potential between water-water and water-asphalt particles. We use the positive (i.e., repulsive) branch of the Lennard Jones potential:

$$U_{LJ} = 4\varepsilon_{LJ}\left[\left(\frac{\sigma_{LJ}}{r}\right)^{12} - \left(\frac{\sigma_{LJ}}{r}\right)^{6}\right] \quad r < 2^{\frac{1}{6}}\sigma_{LJ} \quad (14)$$

where r is the distance between two particles, ε_{LJ} is an energy constant that determines the particle's rigidity and σ_{LJ} is the distance at which the inter-particle potential is zero. The condition $r < 2^{1/6}\sigma_{LJ}$ assures that only the repulsive part of the potential is used. Equation (14) comes from molecular dynamics, but here it provides a repulsive potential that avoids compenetration of water particles with mastic and aggregate particles (and among themselves) for distances smaller than σ_{LJ}. The value of ε_{LJ} for ice can be approximated as follows (for simplicity, in the following discussion, we will name ε_{LJ} and σ_{LJ} simply as ε and σ). We assume that under the hypothesis of small deformations $r \approx r_0$, the Lennard Jones potential approximates the Harmonic potential; see Figure 2. From the potentials in Equation (15), the forces are derived in Equation (16), Table 1.

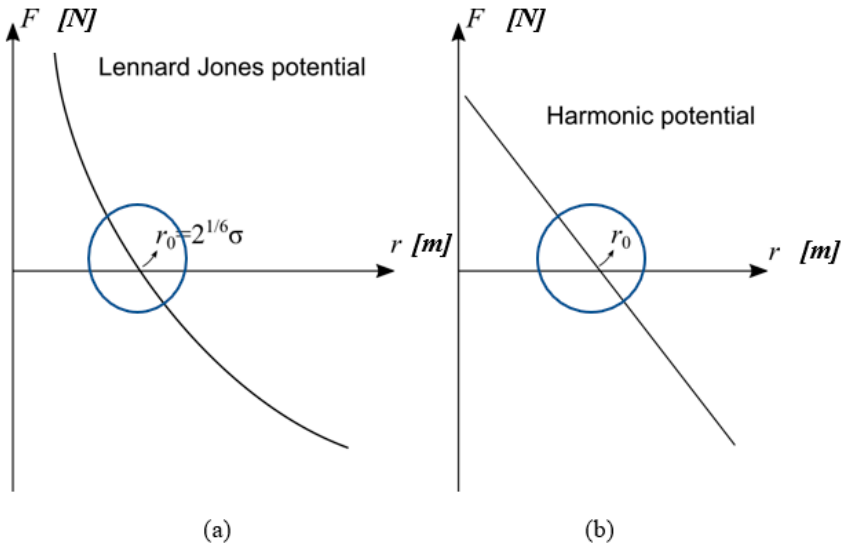

Figure 2. (**a**) Lennard Jones potential and (**b**) Harmonic potential.

Table 1. Lennard Jones and Harmonic potentials and forces.

Lennard Jones	Harmonic	
Potential: $E_{LJ} = 4\varepsilon\left[\left(\frac{\sigma}{r}\right)^{12} - \left(\frac{\sigma}{r}\right)^{6}\right] = \varepsilon\left[\left(\frac{r_0}{r}\right)^{12} - 2\left(\frac{r_0}{r}\right)^{6}\right]$	**Potential**: $E_H = \frac{1}{2}k\Delta r^2$	(15)
Force: $F_{LJ} = \frac{12\varepsilon}{r_0}\left[\left(\frac{r_0}{r}\right)^{13} - 2\left(\frac{r_0}{r}\right)^{7}\right]$	**Force**: $F_H = -k\Delta r$	(16)

Assuming that repulsive force between particles can be modelled as linear springs, the spring constant k is a function of the depth of the potential:

$$F_H \cong \frac{dF_{LJ}}{dr}\Delta r \rightarrow k \cong -\frac{dF_{LJ}}{dr}\Big|_{r_0} - \frac{dF_{LJ}}{dr} = \frac{12\varepsilon}{r_0^2}\left[13\left(\frac{r_0}{r}\right)^{14} - 7\left(\frac{r_0}{r}\right)^{8}\right] \quad (17)$$

$$k \cong -\frac{dF_{LJ}}{dr}\Big|_{r_0} = \frac{72\varepsilon}{r_0^2} \quad (18)$$

According to Kot et al. [43], the bulk modulus for a regular cubic lattice is:

$$K = \frac{5}{3}\frac{k}{r_0} \quad (19)$$

and, therefore,

$$\varepsilon \cong \frac{Kr_0^3}{120} \quad (20)$$

where ε is an energy constant, K is the bulk modulus and r_0 is the lattice constant at which the potential is zero (i.e., $r_0 = l$, the initial distance between water particles). Expansion is simulated by increasing the parameter σ_{LJ}. During the simulation, σ_{LJ} goes from $\sigma^0_{LJ} = l$ [m] at $t = 0$ to $\sigma^{END}_{LJ} = 1.05l$, corresponding to a 15% volume expansion of water at the end of the simulation.

3. Methodology

The real and artificial asphalt mixtures used in this study are presented and discussed in this section. Both imaging of the section and micro-CT scan results are used to generate the initial microstructure of the asphalt models to evaluate the accuracy of the techniques used. The digital microstructures are then modified to represent a range of void % and saturation degree in the asphalt microstructure. The details of the processes followed are also presented in this section.

The numerical models, after validation, were used to simulate compressive tests on asphalt before and after being subjected to a cycle of freeze-thaw. The damage progression under compressive loading and the freeze-thaw was evaluated and discussed with the aim of the numerical results obtained. The details of the numerical analyses and the input parameters used are also presented in this section.

3.1. Mixtures

The asphalt models used in the simulations were derived from samples of four types of asphalts: Dense Asphalt (DA), Porous Asphalt #1 (PA #1), Porous Asphalt #2 (PA #2) and Porous Asphalt #3 (PA #3), with target air voids of 5 10, 13 and 21%, respectively. The physical samples were prepared in the NTEC laboratories at the University of Nottingham, Nottingham, UK. CT-scanned and (as explained later) digitalised in a format readable by the software used to carry out the simulations.

The composition, aggregate gradation and binder contents in the samples are shown in Table 2. For all mixtures, crushed limestone aggregates with a maximum size of 20 mm and 50/70 pen bitumen were used. The standards BS EN 13043:2013 for DA, BS EN 13108-1 for PA and BS EN 12697–33 were followed to manufacture the materials [44]. The materials were mixed at 160 °C and roller compacted at 140 °C. Asphalt slabs of 300 × 300 × 50 mm^3 were produced. From the DA slab, a 35 × 35 × 55 mm^3 was cut. From the slabs made of PA #1, PA #2 and PA #3, cores of 100 mm diameter and 50 mm height were extracted.

Table 2. Asphalt mixture composition.

Size (mm)	Passing (%) DA	Passing (%) PA #1	Passing (%) PA #2	Passing (%) PA #3
20	0.9	0.0	20	10
14	15.8	0.0	25	38
10	21.3	35.1	26	35
6.3	14.2	19.3	7	0
Dust	47.8	45.6	22	17
Bitumen	4.7	4.5	4.2	3.3
Air void content	5.0	10.0	13	21

3.2. DA Model

The DA sample surface was photographed using a digital camera with resolution 1257 × 896 and the pictures converted in a black and white image with MATLAB R2020a (The Math Works, Inc., Natick, MA, USA) and over imposed on a square lattice with side $l = 10^{-4}$ m. Each node of the lattice corresponds to a Peridynamic particle: blue particles were created to represent mastic and red particles to represent aggregates, see Figure 3. According to the reference [45], aggregates greater than 1.18 mm can be considered part of the solid skeleton structure. Hence, mastic was defined as a mixture of aggregates ≤ 1.18 mm and bitumen. While we are aware that this is a simplification, we will assume that this value remains constant for the mixtures that we studied.

In DA, voids were not considered due to the difficulty of identifying them using digital photography. DA has 190,000 particles for the mastic and 300,000 for the aggregates.

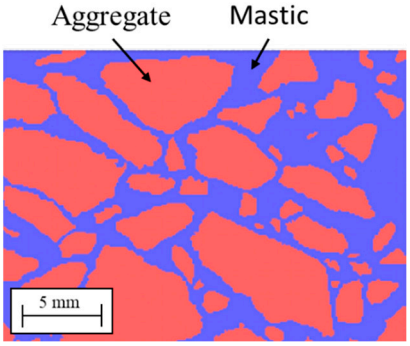

Figure 3. Asphalt (DA): blue particles represent the mortar; red particles represent the aggregate.

3.3. PA Models

A Phoenix v|tome|x L 300 micro CT scanner was used to scan PA asphalt samples under dry conditions; the X-ray tube was MXR320HP/11 (3.0 mm Be + 2 mm Al) from GE Sensing and Inspection Technology (Shanghai, China) operating with an acceleration voltage of 290 kV and a current of 1300 mA.

We carried out the X-ray CT scans in the micro-computed tomography Hounsfield facility at the University of Nottingham, Nottingham, UK. We mounted the samples on a rotational table at a distance of 906.84 mm from the X-ray source. The reconstruction of scans was performed using GE Datos|x reconstruction software with 2× resolution to obtain a spatial resolution of 45.2 mm; the scans had an isotropic resolution, meaning that the slice thickness was also 45.2 mm. The raw images were 16-bit images, and the voxel value represented the x-ray attenuation.

Then, ImageJ version 1.49 was used to process the images [46], convert them to 8-bit grayscale resolution and denoise the images to remove small clusters of voids and grains. The different material components such as aggregates, bitumen and air voids were extracted by segmenting the images based on grayscale thresholding using ImageJ version 1.49 (Rasband, W.S., ImageJ, U. S. National Institutes of Health, Bethesda, MD, USA).

The picture was over imposed on a square lattice with side $l = 4 \times 10^{-4}$ m using Matlab 2020a. As in the case of DA, each node of the lattice corresponds to a peridynamic particle: blue particles are assigned to mastic, and red particles are used to represent aggregates, see Figure 3. No computational particle was created in areas corresponding to the voids. Since the void fraction and aggregate size differed in the three samples, the number of particles was not the same. Sample PA #1 had 341,000 particles for the mortar and 367,000 for the aggregates; PA #2 148,000 particles for the mortar and 538,500 for the aggregates; PA #3 172,000 particles for the mortar and 455,000 particles for the aggregates.

3.4. Additional Asphalt Geometries

To generate new geometries of asphalt mixtures with a range of air void properties, using ImageJ, we assumed that the mixtures from Figure 4 were the reference. From each of these specimens, we produced five different materials. (i) Without air voids; (ii) with the 25% smallest air voids; (iii) with the 50% smallest air voids; (iv) with 75% of the smallest air voids and (v) with 100% of the air voids (equivalent to the reference sample). See an example in Figure 5. The air voids' geometries, including the average void area, diameter, perimeter, circularity and aspect ratio, were measured using the Particle Analysis function in ImageJ [45]. Finally, a suffix indicating the final void fraction was assigned to each generated sample. For example, PA #1/2.5% means that we started from PA #1 and filled all the voids so that the final void fraction was 2.5%. The aggregate gradation and binder contents are shown in Table 3. Increasing the amount of mastic, we add bitumen and dust smaller than 1.18 mm, keeping the skeleton structure constant.

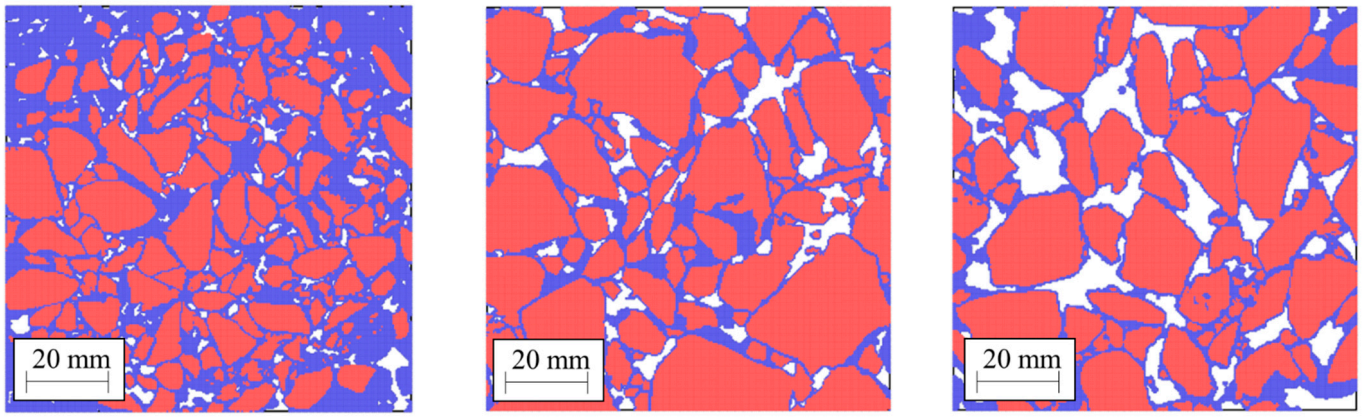

(**a**) (**b**) (**c**)

Figure 4. Samples (**a**) PA #1; (**b**) PA #2; (**c**) PA #3. Blue particles represent the mortar, red particles the aggregate.

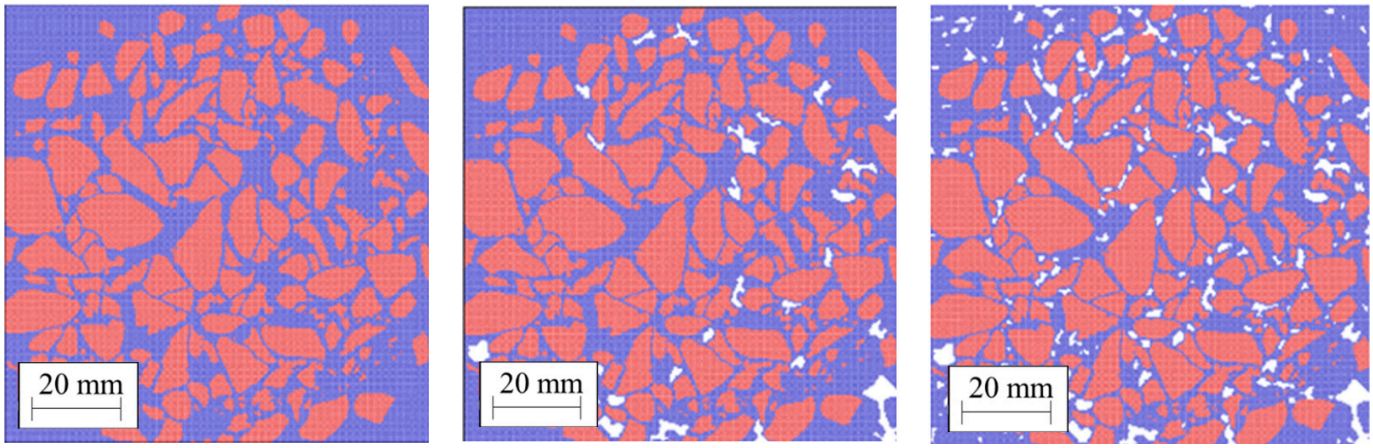

(**a**) (**b**) (**c**)

Figure 5. Examples of PA #1 with a range of air void contents. (**a**) 0%; (**b**) 5 %; and (**c**) 10 %.

Table 3. Asphalt mixture composition.

Size (mm)	Passing (%)											
	PA#1 7.5%	**PA#1 5%**	**PA #1 2.5%**	**PA #1 0%**	**PA#2 9.75%**	**PA#2 6.5%**	**PA#2 3.25%**	**PA #2 0%**	**PA#3 15.75%**	**PA#3 10.5%**	**PA#2 5.25%**	**PA #3 0%**
20	0.0	0.0	0.0	0.0	19.5	19.0	18.5	18.1	9.8	9.2	8.9	8.6
14	0.0	0.0	0.0	0.0	24.5	23.8	23.2	22.7	36.3	35.0	33.5	32.3
10	34.5	33.9	33.3	32.5	25.3	24.7	24.1	23.5	33.4	32.2	30.9	29.7
6.3	18.9	18.5	18.2	18.0	6.8	6.7	6.6	6.4	0.0	0.0	0.0	0.0
Dust above 1.18 mm [46]	30.0	29.4	28.8	28.4	8.8	8.6	8.4	8.3	6.7	6.4	6.2	6.0
Dust below 1.18 mm [46]	16.6	18.2	19.7	21.1	15.1	17.2	19.2	21.0	13.8	17.2	20.5	23.4
Bitumen	5.2	5.9	6.5	7.1	5.2	6.2	7.0	7.9	5.1	6.8	8.2	9.5
Air void content	7.5	5.0	2.5	0.0	9.75	6.5	3.25	0	15.75	10.5	5.25	0

Table 4 shows the topological properties of air voids in asphalt mixtures produced in this section. Similar results were presented in [12]. These results will be used below to evaluate the influence of freezing on the degradation of pavements.

Table 4. Topological properties of the voids calculated from the CT-scans.

Sample	Void Content [%]	Mean Void Diameter [mm]	Mean Void Area [mm²]	Mean Void Perimeter [mm]	Mean Void Aspect Ratio [—]	Mean Void Circularity [—]
PA #1/0%	0.00	0.00	0.00	0.00	0.00	0.00
PA #1/2.5%	2.50	1.19	1.11	2.80	1.87	0.72
PA #1/5%	5.00	1.47	1.70	3.63	1.99	0.67
PA #1/7.5%	7.50	1.67	2.19	4.27	2.03	0.65
PA #1/10%	10.00	1.82	2.60	4.82	2.03	0.64
PA #2/0%	0.00	0.00	0.00	0.00	0.00	0.00
PA #2/3.25%	3.25	2.22	3.87	7.83	2.41	0.54
PA #2/6.5%	6.50	3.29	8.50	10.05	2.41	0.51
PA #2/9.75%	9.75	3.82	11.46	11.60	2.38	0.49
PA #2/13%	13.00	3.42	9.18	13.48	2.40	0.48
PA #3/0%	0.00	0.00	0.00	0.00	0.00	0.00
PA #3/5.25%	5.25	3.73	10.92	20.75	2.29	0.48
PA #3/10.5%	10.50	4.79	18.01	23.80	2.11	0.49
PA 3/15.75%	15.75	5.57	24.35	23.95	2.16	0.47
PA #3/21%	21.00	6.06	28.83	19.36	2.11	0.51

3.5. Freeze-Thaw Simulation

We only used PA #2, which has a 13% air void content, to evaluate the effect of freeze-thaw on mechanical properties. For this purpose, we artificially filled some of the voids with ice, presented as yellow particles in Figure 6. To distinguish among samples, a suffix indicating the final ice content was assigned to each generated sample. For example, PA #2/0.65% means that we started from PA #2 and filled all the voids so that the final ice content was 0.65%. Figure 6 shows how this process was carried out. We started with the real PA #2 sample whose void fraction was 13%. Then, we gradually covered some of the voids (chosen randomly) with ice (yellow particles) until the ice content was 0.65%, Figure 6a, 1.3%, Figure 6b, 3.25%, Figure 6c, 6.5%, Figure 6d, 9.75%, Figure 6e and finally 13%, Figure 6f. The freeze-thaw simulation was performed following these steps:

- Water expands in the voids simulating ice formation, leading to cracking.
- After the water expansion is completed, the simulation is carried out for additional 10^6 time steps to relax the system with no external load.
- Water shrinks in the void, simulating ice melting.
- Water is removed.
- After the water is removed, the simulation is carried out for additional 10^6 time steps to relax the system with no external load.
- Finally, the sample is tested under simulated compression to assess mechanical response changes after the sample is subjected to a freeze-thawcycle.

3.6. Numerical Modelling Details and Input Parameters

The intrinsic properties of the mastic and aggregate were the same for all simulations. In this study, we focused on temperatures below −10 °C and, therefore, we used the Peridynamic model for brittle materials discussed before. The mechanical properties used in the simulations of bitumen and asphalt mixtures are reported in Table 5; they were obtained from [47] and [48]. The peridynamic parameters of the asphalt binder used for the simulations are listed in Table 6.

The calculation of the temperature profile inside the sample would require a non-isothermal model (the reader can refer to [37] for modelling heat transfer and phase transition with particle methods). During solidification, water remains at 0 °C because of the latent heat. The scenario we have in mind is when the water has permeated into the asphalt and freezes. We assume that the external temperature is sufficiently low; as a first approximation, the average temperature of the asphalt sample is close to −10 °C.

To simulate a uniaxial compressive test, each sample is placed into the simulation box between two rigid walls (boundary conditions). The simulations are carried out under plane stress conditions. For the model, this implies that we take a parallel slice with a thickness larger than the horizon and impose the stress along the *z* direction equal to zero. The physical parameters at the interface were set to the physical parameters of the mastic. The upper wall moves downward at a controlled velocity, and the lower wall is fixed. Uniaxial compression test simulation is carried out along the y-direction at a compression rate of 0.001 m/s; (we verified that quasi-static conditions were achieved at 0.001 m/s), the other directions were set to be free to expand or shrink. The time step used in all simulations was 10^{-8} s.

The Peridynamic stress was calculated from the total force per volume, acting through the first layer of particles in contact with the upper wall. The resultant force was obtained by multiplying the particle's volume and the average force density of the top layer. The simulations were carried out with the Peridynamics package [49] in LAMMPS/stable_7Aug2019-foss-2019a (http://lammps.sandia.gov) [50].

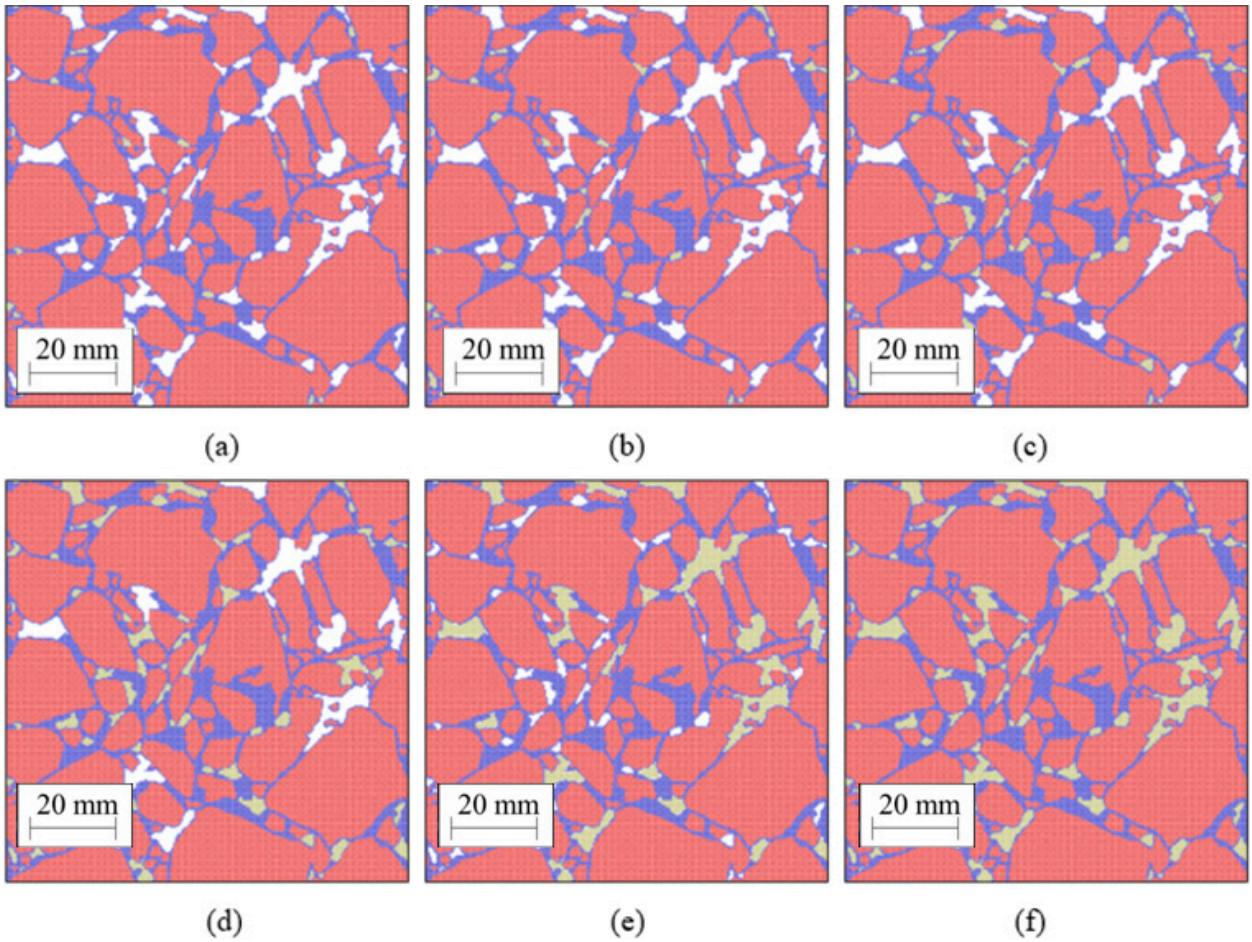

Figure 6. (**a**) PA #2/0.65% ice; (**b**) PA #2/1.3% ice; (**c**) PA #2/3.25% ice; (**d**) PA #2/6.5% ice; (**e**) PA #2/9.75% ice; (**f**) PA #2/13% ice Ice is represented by yellow particles.

Table 5. Mechanical properties of bitumen, mastic and aggregates at −10 °C used in the simulations.

Material	ϱ [kg m³]	*E* [GPa]	ν [-]	G_0 [kJ/m²]
Bitumen, PG64-22 at −18 °C [45]	1000	3.7	0.30	—
Mastic [48]	2200	18.2	0.25	270.00
Aggregates [48]	2500	56.8	0.15	0.25
Interface mastic/aggregates [48]	—	18.2	0.25	77.00

Table 6. Peridynamic parameters used in the simulations. s_{00} is defined by Equation (9).

Model	l [m]	s_{00} [—]	α [—]	N
Bitumen beams (3D)	1×10^{-3}	1.2×10^{-4}	0.30	3366
	5×10^{-4}	1.2×10^{-4}	0.30	23,331
	2×10^{-4}	1.2×10^{-4}	0.30	332,826
	1×10^{-4}	1.2×10^{-4}	0.30	2,580,651
Bitumen beams (Thin plate)	1×10^{-3}	2.0×10^{-4}	0.30	3927
	5×10^{-4}	2.0×10^{-4}	0.30	14,847
	2×10^{-4}	2.0×10^{-4}	0.30	76,806
	1×10^{-4}	2.0×10^{-4}	0.30	303,606
Mastic, DA	1×10^{-4}	6.4×10^{-3}	0.25	—
Aggregate, DA	1×10^{-4}	1.3×10^{-4}	0.25	—
Interface, DA	1×10^{-4}	3.4×10^{-3}	0.25	—
Mastic, PA	4×10^{-4}	3.2×10^{-3}	0.25	—
Aggregate, PA	4×10^{-4}	6.5×10^{-5}	0.25	—
Interface, PA	4×10^{-4}	1.7×10^{-3}	0.25	—

4. Model Validation

We modelled the tensile strength of bitumen beams tested in [45] to validate the accuracy of the modelling strategy and its parameters. For this purpose, we produced 3D and thin plate (i.e., pseudo 2D with the thickness slightly larger than the horizon simulated under the plane stress condition) models of the bitumen with different resolutions (number of particles used for development of the model) and checked the sensitivity of the results to these parameters.

The 3D specimen had dimensions of $1.0 \times 5.0 \times 0.5$ cm^3 simulated with four lattice resolutions in the range $l = 10^{-3} - 10^{-4}$ m; see Figure 7a–c. In addition, the thin plate specimen had dimensions of 1.0×5.0 cm^2 and a resolution of $l = 10^{-3} - 10^{-4}$ m, see Figure 7d.

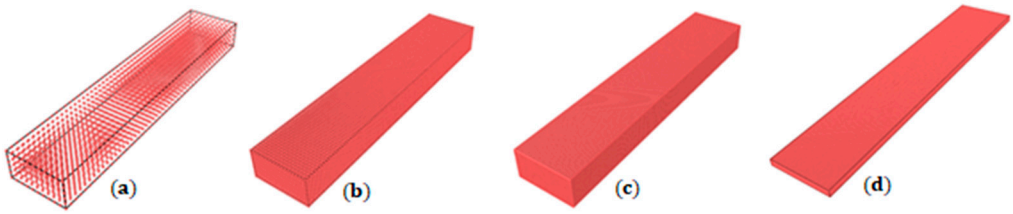

Figure 7. Geometries of bitumen for tensile tests. (**a**) 3D, l = 10^{-3} m; (**b**) 3D, l = 5×10^{-4} m; (**c**) 3D, l = 2×10^{-4} m; (**d**) example of a thin plate, l = 2×10^{-4} m.

The number of particles in the 3D samples was 3366, 23,331, 332,826 and 2,580,641, for l 10^{-3}, 5×10^{-4}, 2×10^{-4} and 10^{-4} m, respectively. The number of particles in the thin plates was 3927, 14,847, 76,806 and 303,606, for l 10^{-3}, 5×10^{-4}, 2×10^{-4} and 10^{-4} m, respectively. The simulations were conducted at the two strain rates, 30 and 140 mm × min^{-1}. The Peridynamic stress was calculated from the total force per volume, acting through the first layer of particles in contact with the upper wall.

Figure 8 shows the bitumen's beam's failure in a 3D simulation showing that breakage is visually comparable with an equivalent experiment from the literature [45].

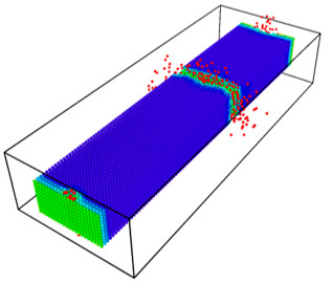

Figure 8. Broken bitumen sample in the simulation.

Figure 9a shows the tensile results of the 3D beam. Results are independent of the loading rate, and when the particle resolution is $l < 2 \times 10^{-4}$ m, simulations are very close to the experimental data. Figure 9b shows the 2D (thin plate) results. For $l < 2 \times 10^{-4}$ m, the results are independent of the particle resolution. However, contrary to the 3D results, they do not converge to the experimental data. In 2D, the greatest difference between the experiment and simulation is 10%. However, the 3D simulation at $l = 10^{-4}$ m has eight times as many particles as the 2D simulation at the same resolution, which makes the simulation 16 times slower. Therefore, we decided to accept the error and run the simulations for thin plates at lattice $l = 10^{-4}$ m.

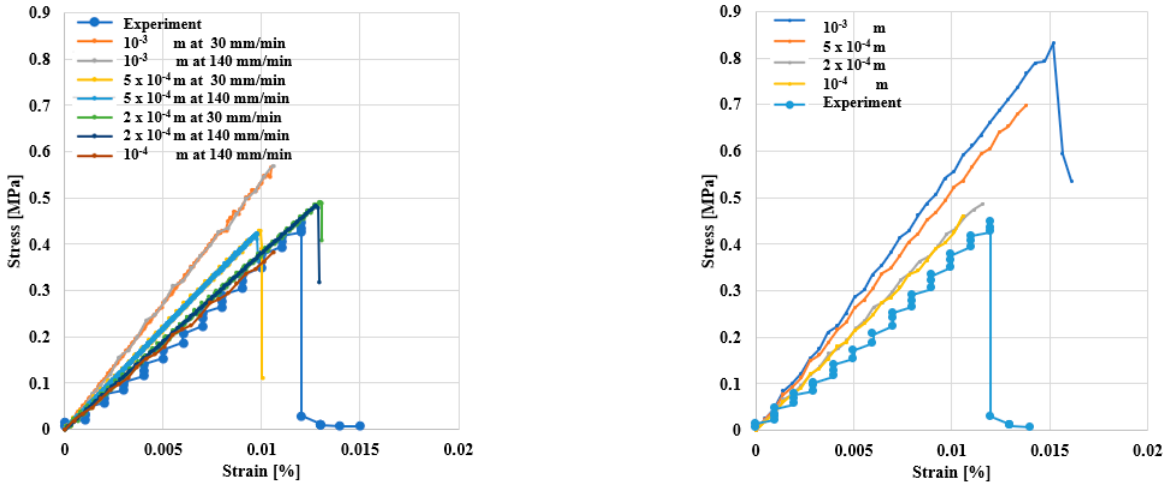

Figure 9. Stress/strain of bitumen beams at different resolutions and loading rate and comparison with other experiments [45]. (**a**) In 3D and (**b**) as a thin plate.

5. Results and Discussion

5.1. Compressive Response of DA Asphalt

The result for the uniaxial compression test for each sample is shown Figure 10a. The stress-strain curve follows an equivalent tendency to that of experimental curves reported in the literature for asphalt at low temperatures showing brittle behaviour [51]. As expected, the stress increases with the compression, undergoing a sudden fracture and leading to total failure of the samples.

The stress-strain curve and the percentage of broken Peridynamic bonds (damage) in the sample are compared in Figure 10a to illustrate the relationship between stress and damage. Two stages from the stress-strain curve can be distinguished during the failure process [52]. In Stage I (strain < 0.015%), there are no obvious cracks. Stage II occurs when the local strain reaches the critical value s_0. Some of the bonds begin to break, generating micro-cracks in the aggregate. As the strain increases further, micro-cracks propagate, weakening the material, and the load exceeds the ultimate strength of the sample; micro-

cracks evolve around the aggregates, resulting in large deformations and ultimately the destruction of the sample. Finally, Figure 10b shows that micro-cracks form mainly in the aggregate, especially at the interfaces, which can be considered the asphalt's weak part.

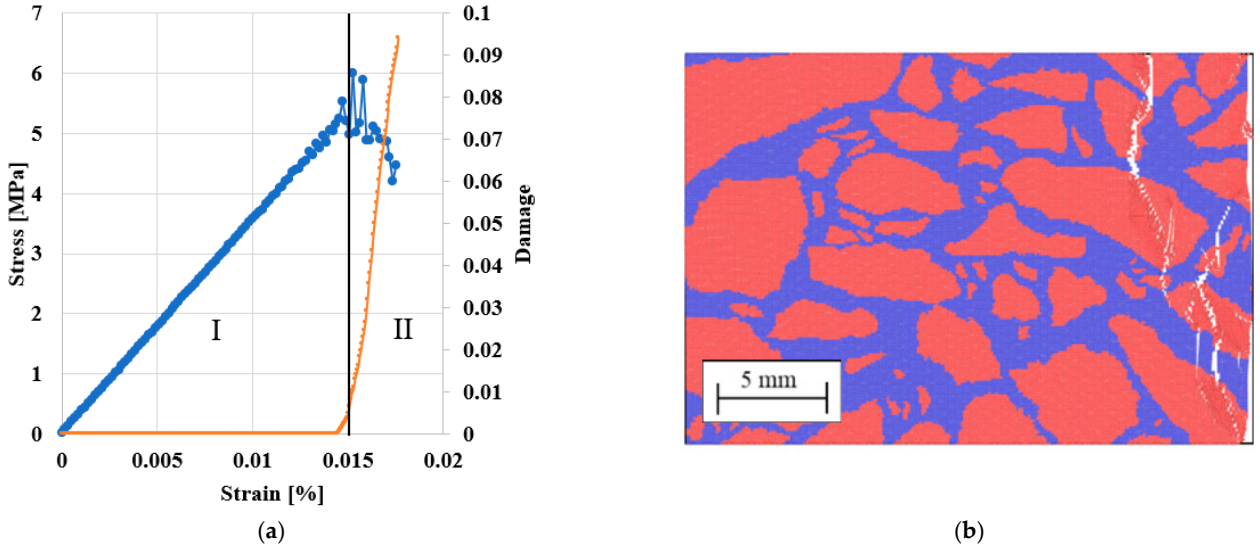

Figure 10. (**a**) Stress (blue curve) and the fraction of broken bond (damage, orange curve) versus strain. (**b**) Micro-crack formation in an asphalt specimen.

5.2. Compressive Response of PA Asphalt

Uniaxial compression tests of the PA test specimens mentioned above were also simulated to determine whether the peridynamics could capture the air voids' influence on the asphalt's compression strength. All the samples were subjected to the same load and boundary conditions as the DA samples. Figure 10 compares stress/strain curves for PA #1, PA #2 and PA #3, in the range of the air void contents studied.

According to Figure 11, the asphalt stiffness and the peak load decrease by increasing the number of voids and their size. The maximal stress decreased by 64% (PA #1), 77% (PA #2) and 91% (PA #3) compared to the same asphalt with no voids, and the weakening of the material led to early breakage. In real asphalt, this could mean that the weakening of the material due to air voids' presence leads to early breakage [2,30]. Hence, to produce durable asphalt, especially at lower temperatures, when the asphalt is prone to ravelling, it is advised that the content of mastic in the material is maximised.

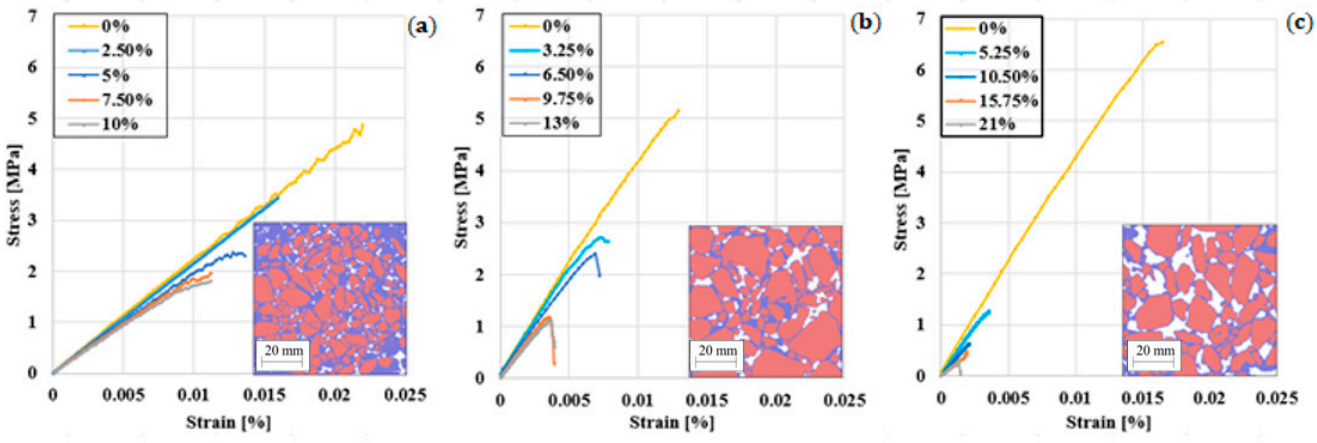

Figure 11. Stress/strain curves for PA #1 (**a**), PA #2 (**b**) and PA #3 (**c**) samples.

There are different types of asphalts that cover a wide range of compressive strengths depending on the bitumen, aggregate, fillers and voids. Our asphalt is in line with the compressive results for asphalts reported in the literature e.g. [53–55] at the same temperature. According to the sample and the void fraction, the model's values in Figure 10 are between 0.5 and 3.5 MPa. Reference [53] reports values between 1.5 and 1.9 MPa, reference [54] between 2 and 3 MPa and [55] between 1.7 and 2.2 MPa, which are in the same range as our simulations. The model's compressive results depend on the choice of parameters, and specifically G_0, the fracture energy reported in Table 5, used in the simulations. G_0 was taken from [48] and refers to weakly aggregated dolomite limestone [48], normally used to build road bases or binder courses. Hence, the compressive strength of asphalt will reflect the poor properties of these aggregates. Properties of additional aggregates can be found in reference [56].

Table 7 reports the Pearson's correlation between the mechanical and the topological properties of the samples. The max stress and the max deformations are, respectively, the maximal stress and deformation before the sample's failure, while for the equivalent Young's Modulus, the slope of the linear part of the stress/strain curve, see Figure 11.

As expected, a higher void content reduces the uniaxial compressive strength of the asphalt. Table 7 also shows that larger voids are more detrimental than smaller voids for the same void content. Moreover, given the same void size, samples with elongated and irregular shapes (i.e., high aspect ratio, low circularity) show, in general, lower ultimate strength and an equivalent Young's modulus than samples with circular-like voids. The reasons for this are still unclear and will be investigated in future research.

Table 7. Pearson correlations between the mechanical and the topological properties of the samples.

Properties	Void Content	Mean Void Diameter [mm]	Mean Void Area	Mean Void Aspect Ratio	Mean Void Circularity
Ultimate strength	−0.62	−0.64	−0.58	−0.52	−0.37
Ultimate strain	−0.77	−0.92	−0.82	−0.73	−0.41
Equivalent Young modulus	−0.26	0.02	0.09	−0.32	−0.57

To compare changes of strength between the different types of asphalt analysed due to changes in gradation and amount of mastic, we have defined the parameter β as:

$$\beta = \left(1 - \frac{\text{maximal strength of the asphalt sample}}{\text{maximal strength of asphalt with 0\% air voids}}\right) \times 100 \quad (21)$$

Finally, Figure 12 shows how β varies with the air voids fraction for PA #1, PA #2 and PA #3. It can be observed that small changes in the void fraction have a lower influence on the compressive strength of asphalt for densely packed mixtures. However, other types of mixtures, such as PA #3, could be extremely sensitive to changes in the amount of voids, for example, due to the lack of filler or changes in the source of dust, and extreme care should be taken during their design and manufacturing. This will be a point that we will analyse experimentally in future research.

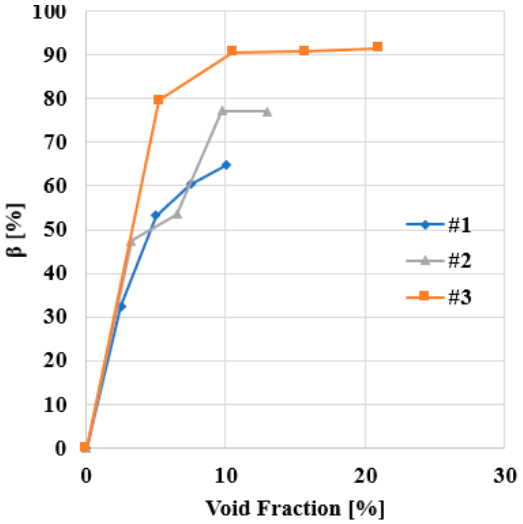

Figure 12. Changes of β with void %.

5.3. Effect of Freeze-thawon the Compressive Strength

Figure 13 shows the sample during the ice expansions. Breakage starts where ice expands and propagates at the bitumen-aggregate interface. This also creates new voids and increases the void fraction [7]. As expected, the freeze-thawcycle decreases the strength of asphalt [57–59]. To quantify this decrease and compare the simulations with experimental data, we define the reduction of the peak stress after freeze-thawas follows:

$$\gamma = \left(1 - \frac{\text{peak stress of the sample after freeze} - \text{thaw}}{\text{peak stress of the intact sample}}\right) \times 100 \quad (22)$$

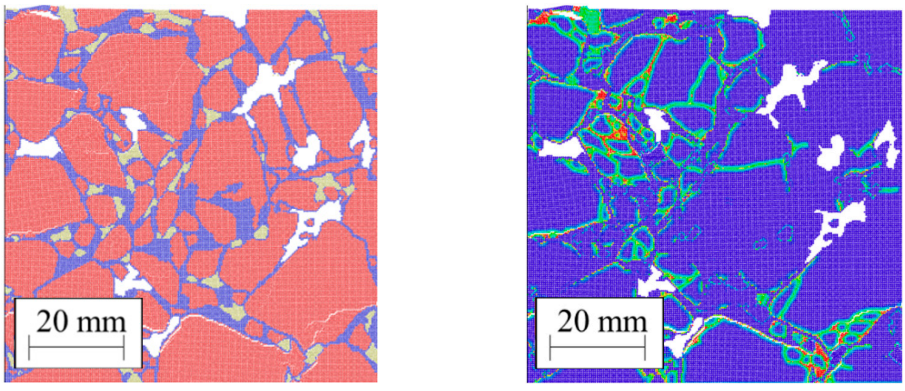

(**a**) (**b**)

Figure 13. Cracking propagation due to ice expansion: (**a**) geometry; (**b**) damage.

Figure 14 shows how γ varies with the ice fraction and confirms the ice's impact on fracture performance. During the ice expansion, cracks appear in the structure, and the stiffness of asphalt is compromised, leading to a reduction in the sample's peak stress and earlier failure.

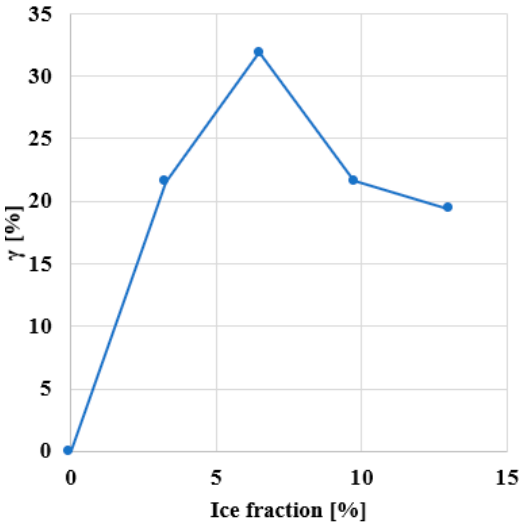

Figure 14. Reduction of peak stress with ice %.

These results compare with experimental data. For example, reference [9] has determined that for a porous asphalt mixture with approximately 20% air void content, the strength loss can be higher than 40%. Further, most of the strength is lost after the first cycle, as shown in Figure 13. In future research, this computational framework will be used to better understand the influence of air voids' geometrical properties on the resistance of the asphalt to freeze-thawcycles.

6. Conclusions

In this article, we have demonstrated the use of Peridynamics combined with Discrete Multiphysics to model crack formation and propagation in asphalt at low temperatures taking into account air voids and ice formation. Find below some of the conclusions:

- This paper demonstrates a way to understand how microcracks are formed in the asphalt under freezing conditions, a phenomenon that is extremely difficult to observe in experiments.
- The simulations show the model's reliability in obtaining a mechanical response comparable with experimental tension and compression tests of bitumen and asphalt, respectively.
- As expected, the higher the void fraction, the higher the loss of compressive strength of an asphalt mixture. Further, the size and shape of the voids affect the strength of the asphalt. Larger voids are more detrimental than smaller voids, especially if they have a high aspect ratio and low circularity.
- Using this model, we observed that the amount of mastic in densely packed mixtures does not have a strong influence on the compressive strength of asphalt. However, less densely packed mixtures, such as porous asphalt, are more sensitive to the amount of mastic in the asphalt.
- The model can also assess the effect of ice formation on the asphalt structure. Water particles are created in the voids, and their volume is increased with time to simulate solidification. The simulations show the formation of cracks produced by water expansion during solidification and the consequent loss in mechanical strength. To the best of our knowledge, water expansion in cavities has not been simulated to date.

This methodological study provides researchers in the field with a powerful new tool for understanding the behaviour of asphalt under scenarios that, so far, have not been accessible to computer simulation. The systematic study of asphalt mechanical properties changes due to the size, number and distribution of ice-filled voids will be done in future research.

Author Contributions: Conceptualisation, D.S., B.G., A.A., A.G.H.; methodology, All authors; software, D.S, B.G., A.A.; validation, D.S.; formal analysis, D.S.; investigation, D.S.; resources, All authors; data curation, D.S.; writing—original draft preparation, All authors; writing—review and editing, All authors; visualisation, All authors; supervision, B.G. A.A., A.G.H. All authors have read and agreed to the published version of the manuscript.

Funding: PhD fund lead to this study was provided by the Faculty of Engineering of the University of Notitngham and the School of Chemical Engineering of the University of Birmingham.

Institutional Review Board Statement: Not applicable.

Informed Consent Statement: Not applicable.

Data Availability Statement: The code used for the simulations is freely available under the GNU General Public License v3 and can be downloaded from the University of Birmingham repository http://edata.bham.ac.uk/568/.

Acknowledgments: The authors express their gratitude to the Universities of Nottingham, Birmingham and Highways England UK that funded this study.

Conflicts of Interest: The authors declare no conflict of interest.

References

1. Bobiński, J.; Tejchman, J. A coupled constitutive model for fracture in plain concrete based on continuum theory with non-local softening and eXtended Finite Element Method. *Finite Elements Anal. Des.* **2016**, *114*, 1–21.
2. Suchorzewski, J.; Tejchman, J.; Nitka, M. Discrete element method simulations of fracture in concrete under uniaxial compression based on its real internal structure. *Int. J. Damage Mech.* **2018**, *27*, 578–607.
3. Ling, M.; Zhang, Y.; Kaseer, F.; Martin, A.E.; Lytton, R.L. Investigation of fracture behavior of asphalt mixture composite using energy-based approach. *Compos. Part B Eng.* **2020**, *181*, 107324.
4. Kollmann, J.; Liu, P.; Lu, G.; Wang, D.; Oeser, M.; Leischner, S. Investigation of the microstructural fracture behaviour of asphalt mixtures using the finite element method. *Constr. Build. Mater.* **2019**, *227*, 117078.
5. Ozgan, E.; Serin, S. Investigation of certain engineering characteristics of asphalt concrete exposed to freeze-thawcycles. *Cold Reg. Sci. Technol.* **2013**, *85*, 131–136.
6. Tang, N.; Sun, C.; Huang, S.; Wu, S. Damage and corrosion of conductive asphalt concrete subjected to freeze-thawcycles and salt. *Mater. Res. Innov.* **2013**, *17*, 240–245.
7. Xu, H.; Guo, W.; Tan, Y. Internal structure evolution of asphalt mixtures during freeze-thawcycles. *Mater. Des.* **2015**, *86*, 436–446, doi:10.1016/j.matdes.2015.07.073.
8. Butkovich, T.R. Thermal Expansion of Ice. *J. Appl. Phys.* **1959**, *30*, 350, doi:10.1063/1.1735166.
9. Sol-Sánchez, M.; Moreno-Navarro, F.; García-Travé, G.; Rubio-Gámez, M.C. Laboratory study of the long-term climatic deterioration of asphalt mixtures. *Constr. Build. Mater.* **2015**, *88*, 32–40, doi:10.1016/j.conbuildmat.2015.03.090.
10. Xu, H.; Guo, W.; Tan, Y. Permeability of asphalt mixtures exposed to freeze-thawcycles. *Cold Reg. Sci. Technol.* **2016**, *123*, 99–106, doi:10.1016/j.conbuildmat.2020.118043.
11. Aboufoul, M.; Shokri, N.; Saleh, E.; Tuck, C.; Garcia, A. Dynamics of water evaporation from porous asphalt. *Constr. Build. Mater.* **2019**, *202*, 406–414, doi:10.1016/j.conbuildmat.2019.01.043.
12. Aboufoul, M.; Garcia, A. Factors affecting hydraulic conductivity of asphalt mixture. *Mater. Struct. Mater. Constr.* **2017**, *50*, 116, doi:10.1617/s11527-016-0982-6.
13. Hernandez-Fernandez, N.; Underwood, B.S.; Ossa-Lopez, A. Simulation of the asphalt concrete stiffness degradation using simplified viscoelastic continuum damage model. *Int. J. Fatigue* **2020**, *140*, 105850, doi:10.1016/j.ijfatigue.2020.105850.
14. Li, Y.; Jiang, W.; Shan, J.; Li, P.; Lu, R.; Lou, B. Characteristics of void distribution and aggregate degradation of asphalt mixture specimens compacted using field and laboratory methods. *Constr. Build. Mater.* **2020**, *270*, 121488, doi:10.1016/j.conbuildmat.2020.121488.
15. Canestrari, F.; Ingrassia, L.P. A review of top-down cracking in asphalt pavements: Causes, models, experimental tools and future challenges. *J. Traffic Transp. Eng. Engl. Ed.* **2020**, *7*, 541–572, doi:10.1016/j.jtte.2020.08.002.
16. Liu, H.; Zeiada, W.; Al-Khateeb, G.G.; Shanableh, A.; Samarai, M. Use of the multiple stress creep recovery (MSCR) test to characterize the rutting potential of asphalt binders: A literature review. *Constr. Build. Mater.* **2020**, *269*, 121320, doi:10.1016/j.conbuildmat.2020.121320.
17. Yan, K.; Ge, D.; You, L.; Wang, X. Laboratory investigation of the characteristics of SMA mixtures under freeze-thawcycles. *Cold Reg. Sci. Technol.* **2015**, *119*, 68–74.
18. Fan, Z.; Xu, H.; Xiao, J.; Tan, Y. Effects of freeze-thawcycles on fatigue performance of asphalt mixture and development of fatigue-freeze-thaw(FFT) uniform equation. *Constr. Build. Mater.* **2020**, *242*, 118043.
19. Cong, L.; Ren, M.; Shi, J.; Yang, F.; Guo, G. Experimental investigation on performance deterioration of asphalt mixture under freeze-thawcycles. *Int. J. Transp. Sci. Technol.* **2020**, *9*, 218–228, doi:10.1016/j.ijtst.2020.04.004.

20. Zhang, Z.N.; Chen, Y.X. Modeling nonlinear elastic solid with correlated lattice bond cell for dynamic fracture simulation. *Comput. Methods Appl. Mech. Eng.* **2014**, *279*, 325–347.
21. Zhao, G.F.; Fang, J.N.; Zhao, J. A 3D distinct lattice spring model for elasticity and dynamic failure. *Int. J. Numer. Anal. Methods Geomech.* **2011**, *35*, 859–885.
22. Jiang, C.; Zhao, G.F.; Khalili, N. On crack propagation in brittle material using the distinct lattice spring model. *Int. J. Solids Struct.* **2017**, *118-119*, 41–57, doi:10.1016/j.ijsolstr.2017.04.024.
23. Silling, S.A. Reformulation of elasticity theory for discontinuities and long-range forces. *J. Mech. Phys. Solids* **2000**, *48*, 175–209, doi:10.1016/s0022-5096(99)00029-0.
24. Pazdniakou, A.; Adler, P.M. Lattice Spring Models. *Transp. Porous Media* **2012**, *93*, 243–262, doi:10.1007/s11242-012-9955-6.
25. Mitchell, J.A. A Nonlocal, Ordinary, State-Based Plasticity Model for Peridynamics. Sandia Report, May, 1–34. Available online: http://www.ntis.gov/help/ordermethods.asp?loc=7-4-0#online (29 May 2020).
26. Mitchell, J.A. *Non-Local, Ordinary-State-Based Viscoelasticity Model for Peridynamics*; Sandia Report, SAND2011-8(October); Sandia National Laboratories: Albuquerque, NM, USA, 2011; 28p.
27. Alexiadis, A. The Discrete Multi-Hybrid System for the simulation of solid-liquid flows. *PLoS ONE* **2015**, *10*, e0124678.
28. Alexiadis, A. A smoothed particle hydrodynamics and coarse-grained molecular dynamics hybrid technique for modelling elastic particles and breakable capsules under various flow conditions. *Int. J. Numer. Methods Eng.* **2014**, *100*, 713–719.
29. Alexiadis, A. A new framework for modelling the dynamics and the breakage of capsules, vesicles and cells in fluid flow. *Procedia UTAM* **2015**, *16*, 80–88.
30. Silling, S.A.; Askari, E. A meshfree method based on the peridynamic model of solid mechanics. *Comput. Struct.* **2005**, *83*, 1526–1535, doi:10.1016/j.compstruc.2004.11.026.
31. Silling, S.A.; Epton, M.; Weckner, O.; Xu, J.; Askari, E. Peridynamic States and Constitutive Modeling. *J. Elast.* **2007**, *88*, 151–184, doi:10.1007/s10659-007-9125-1.
32. Ha, Y.D.; Bobaru, F. Studies of dynamic crack propagation and crack branching with peridynamics. *Int. J. Fract.* **2010**, *162*, 229–244, doi:10.1007/s10704-010-9442-4.
33. Ariane, M.; Wen, W.; Vigolo, D.; Brill, A.; Nash, G.B.; Barigou, M.; Alexiadis, A. Modelling and simulation of flow and agglomeration in deep veins valves using Discrete Multi Physics. *Comput. Biol. Med.* **2017**, *89*, 96–103.
34. Ariane, M.; Kassinos, S.; Velaga, S.; Alexiadis, A. Discrete multi-physics simulations of diffusive and convective mass transfer in boundary layers containing motile cilia in lungs. *Comput. Biol. Med.* **2018**, *95*, 34–42.
35. Schütt, M.; Stamatopoulos, K.; Batchelor, H.K.; Simmons, M.J.H.; Alexiadis, A. Modelling and simulation of the hydrodynamics and mixing profiles in the human proximal colon using. *Discret. Multiphys. Comput. Biol. Med.* **2020**, *121*, 103819.
36. Rahmat, A.; Barigou, M.; Alexiadis, A. Numerical simulation of dissolution of solid particles in fluid flow using the SPH method. *Int. J. Numer. Methods Heath Fluid Flow* **2019**, *30*, 290–307.
37. Alexiadis, A.; Ghraybeh, S.; Geng, Q. Natural convection and solidification of phase-change materials in circular pipes: A SPH approach. *Comput. Mater. Sci.* **2018**, *150*, 475–483.
38. Ariane, M.; Allouche, H.; Bussone, M.; Giacosa, F.; Bernard, F.; Barigou, M.; Alexiadis, A. Discrete multiphysics: A mesh-free approach to model biological valves including the formation of solid aggregates at the membrane surface and in the flow. *PLoS ONE* **2017**, *12*, e0174795.
39. Ariane, M.; Vigolo, D.; Brill, A.; Nash, G.B.; Barigou, M.; Alexiadis, A. Using Discrete Multi-Physics for studying the dynamics of emboli in flexible venous valves. *Comput. Fluids* **2018**, *166*, 57–63.
40. Rahmat, A.; Barigou, M.; Alexiadis, A. Deformation and rupture of compound cells under shear: A Discrete Multiphysics Study. *Phys. Fluids* **2019**, *31*, 051903.
41. Alexiadis, A. Deep Multiphysics and Particle–Neuron Duality: A Computational Framework Coupling (Discrete) Multiphysics and Deep Learning. *J. Appl. Sci.* **2019**, *9*, 5369.
42. Alexiadis, A. Deep Multiphysics: Coupling Discrete Multiphysics with Machine Learning to attain self-learning in-silico models replicating human physiology. *Artif. Intell. Med.* **2019**, *98*, 27–34.
43. Kot, M.; Nagahashi, H.; Szymczak, P. Elastic moduli of simple mass spring models. *Vis. Comput.* **2015**, *31*, 1339–1350, doi:10.1007/s00371-014-1015-5.
44. BS EN 12697-33. *Bituminous Mixtures, Test Methods for Hot Mix Asphalt: Specimen Prepared by Roller Compactor*; BSI: London, UK, 2003.
45. Guarin, A.; Roque, R.; Kim, S.; Sirin, O. Disruption factor of asphalt mixtures. *Int. J. Pavement Eng.* **2013**, *14*, 472–485, doi:10.1080/10298436.2012.727992.
46. Ferreira, T.; Rasband, W.S. "ImageJ User Guide—IJ 1.46", 2010—2012. Available online: https://imagej.nih.gov/ij/docs/guide/ (accessed on 16 July 2020)
47. Mirsayar, M.M. On the low temperature mixed mode fracture analysis of asphalt binder—Theories and experiments. *Eng. Fract. Mech.* **2017**, *186*, 181–194.
48. Kim, H.; Buttlar, W.G. Multi-scale fracture modeling of asphalt composite structures. *Compos. Sci. Technol.* **2009**, *69*, 2716–2723, doi:10.1016/j.compscitech.2009.08.014.
49. Parks, M.L.; Lehoucq, R.B.; Plimpton, S.J.; Silling, S.A. Implementing peridynamics within a molecular dynamics code. *Comput. Phys. Commun.* **2008**, *179*, 777–783.
50. Plimpton, S. Fast Parallel Algorithms for Short-Range Molecular Dynamics. *J. Comput. Phys.* **1995**, *117*, 1–19.

51. Kong, X.M.; Liu, Y.L.; Zhang, Y.R.; Zhang, Z.L.; Yan, P.Y.; Bai, Y. Influences of temperature on mechanical properties of cement asphalt mortars. *Mater. Struct.* **2014**, *47*, 285–292, doi:10.1617/s11527-013-0060-2.
52. Li, W.; Guo, L. Meso-fracture simulation of cracking process in concrete incorporating three-phase characteristics by peridynamic method. *Constr. Build. Mater.* **2018**, *161*, 665–675, doi:10.1016/j.conbuildmat.2017.12.002.
53. Cheng, Y.; Li, H.; Wang, W.; Li, L.; Wang, H. Laboratory evaluation on the performance degradation of styrene-butadiene-styrene-modified asphalt mixture reinforced with basalt fiber under freeze-thawcycles. *Polymers* **2020**, *12*, 1092, doi:10.3390/polym12051092.
54. Wang, F.; Liu, Z.; Wang, T.; Hu, S. Temperature stability of compressive strength of cement asphalt mortar. *ACI Mater. J.* 2010, 107, 27–30, doi:10.14359/51663461.
55. Si, W.; Ma, B.; Wang, H.; Hu, J. Analysis on splitting characteristics of asphalt mixture under freeze-thawcycles in cold plateau regions. *Transp. Sci. Eng.* **2013**, *37*, 805–808, doi:10.3963/j.issn.2095-3844.2013.04.032.
56. Li, X.; Braham, A.F.; Marasteanu, M.O.; Buttlar, W.G.; Williams, R.C. Effect of factors affecting fracture energy of asphalt concrete at low temperature. *Road Mater. Pavement Des.* **2008**, *9*, 397–416, doi:10.3166/RMPD.9HS.397-416.
57. Din, I.M.U.; Mir, M.S.; Farooq, M.A. Effect of Freeze-thawCycles on the Properties of Asphalt Pavements in Cold Regions: A Review. *Transp. Res. Procedia* **2020**, *48*, 3634–3641, doi:10.1016/j.trpro.2020.08.087.
58. Meng, Y.; Li, Z.-Y.; Mei, Y.-J.; Lu, Y.-F. Temperature Modification Coefficient of compressive modulus of asphalt mixture. *J. Tongji Univ. Nat. Sci. Ed.* **2008**, *2*, 182–186.
59. Tan, Y.; Zhao, L.; Lan, B.; Meng, L. Research on Freeze-thawDamage Model and Life Prediction of Asphalt Mixture. *J. Highw. Transp. Res. Dev.* **2011**, *6*, 1–7.

Chapter 5

Effect of freeze–thaw cycles on the void topologies and mechanical properties of asphalt

In this Chapter experiments on asphalt mixture with three different void content has been carried out to establish a correlation between asphalt mixture performance and internal structure at low temperature. Further investigation has been taken using X-ray CT scan to observe the evolution of voids under freezing condition and to obtain the topologies. The results are used in the Chapter 5.

This chapter has been published in *Construction and Building Materials* as:

D. Sanfilippo, A. Garcia-Hernández, A. Alexiadis, B. Ghiassi, Effect of freeze–thaw cycles on the void topologies and mechanical properties of asphalt, Constr. Build. Mater. 344 (2022) 128085.

My contributions in this work were: Conceptualisation, Designed the work and performed the simulations, Methodology, Validation, Writing the original draft, Reviewing and Editing.

I would like to thank all the authors who have contributed to this work.

Construction and Building Materials 344 (2022) 128085

Contents lists available at ScienceDirect

Construction and Building Materials

journal homepage: www.elsevier.com/locate/conbuildmat

Effect of freeze–thaw cycles on the void topologies and mechanical properties of asphalt

D. Sanfilippo [a], A. Garcia-Hernández [a,*], A. Alexiadis [b], B. Ghiassi [c]

[a] Nottingham Transportation Engineering Centre, Department of Civil Engineering, University of Nottingham, Nottingham NG7 2RD, United Kingdom
[b] School of Chemical Engineering, University of Birmingham B15 2TT, UK
[c] Department of Civil Engineering, University of Birmingham B15 2TT, UK

ARTICLE INFO

Keywords:
Asphalt
Freeze–thaw damage
Mechanical properties
Voids topology
Performance deterioration

ABSTRACT

Frost and thawing damage asphalt in cold climates. Water that enters the pores of asphalt at low temperatures may accelerate its degradation. Water can expand into pores, altering the void content and shape, thus affecting the asphalt's internal structure and fracture properties. We can develop more durable asphalt types if we understand how void topology changes with freeze–thaw cycles. The purpose of this study is to establish a correlation between the mechanical properties of asphalts and the topological properties of voids. To determine their internal structure, various asphalt types representing dense asphalt and asphalt with voids were made and X-rayed before and after each freeze–thaw cycle. We also obtained the mechanical properties of asphalt and correlated them with the void properties. It was found that dense asphalt has the lowest degradation rate in wet conditions characterised by non-connected gaps, which was approximately constant with freeze–thaw cycles; however, dense asphalt was least durable under dry conditions compared with asphalts with more voids. Due to its high water retention rate, asphalt with a 10% void content degraded at an accelerated rate during the initial cycles. As a result of bigger voids, asphalt with a higher pore content plateaued in later cycles due to reduced water retention. This study demonstrates that the internal void topology affects the mechanical properties of asphalt during freeze–thaw cycles. These results can be used to understand changes in asphalt mechanical losses resulting from freeze-thaw cycles and to validate numerical models to perform parametric studies of the asphalt's freeze–thaw degradation.

1. Introduction

Asphalt mixture is a heterogeneous material made of aggregates, mineral filler, and a bituminous binder. It is compacted at temperatures ranging between 135 °C and 155 °C; asphalt mixtures may also include voids, up to more than 20 % of the total asphalt's volume, depending on the gradation and compaction methodology. Asphalt is the most used material to build pavement surfaces. Asphalt undergoes different mechanical loads and environmental conditions during its lifetime, leading to crack and damage and reducing its lifespan [1,2]. In particular, the extreme environmental condition in cold regions with large temperature fluctuations [3] and the water permeation are some of the most harmful deterioration mechanisms that may affect asphalt, leading to thermal stress [4], loss of adhesion at the interface between aggregate and bitumen [5], and loss of cohesion of the binder [6].

The binder is a viscoelastic material at high temperatures, while the aggregates are elastic in all the ambient temperature ranges. Moreover, at low temperatures, the binder is an elastic and brittle material [7]. Several factors influence asphalt's mechanical properties, including its temperature, freeze–thaw cycles, air void content and internal void topology. In addition, the air voids content can increase due to the expansion of water under freeze–thaw actions, increasing asphalt's permeability and, consequently, the risk of freeze–thaw damage [3,8]. If water infiltrates the asphalt, it can freeze and expand, increasing the pressure in the pores, modifying the void content and shape, causing cracks and weakening the asphalt. Cracks may appear, creating new voids that alter the internal void structure [9]. Once the ice melts, water may permeate the cracks; and new freeze–thaw cycles may increase damage, following the same mechanism. Consequently, the stiffness modulus [10], strain energy [10], fracture toughness [11], critical stress [11], splitting strength [12], and maximum flexural tensile strain [12], of asphalt may reduce.

* Corresponding author.
E-mail address: alvaro.garcia@nottingham.ac.uk (A. Garcia-Hernández).

https://doi.org/10.1016/j.conbuildmat.2022.128085
Received 14 January 2022; Received in revised form 18 May 2022; Accepted 7 June 2022
Available online 24 June 2022

Table 1
Asphalt mixture composition.

Size (mm)	Target void content, %		
	3%	9.8%	14%
20	0	23.6	0
14	0	42.4	0
10	58.9	0	63.5
6.3	7.5	9.4	18.9
Dust	18.7	12.3	7.6
Filler	8.4	6.6	4.7
Bitumen	6.5	5.7	5.5
Air void content	3	9.8	14

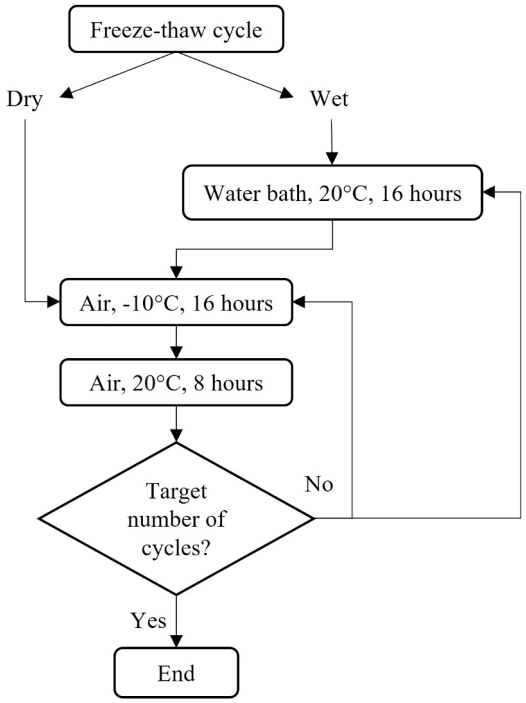

Fig. 1. Steps followed for the freeze–thaw tests of asphalt.

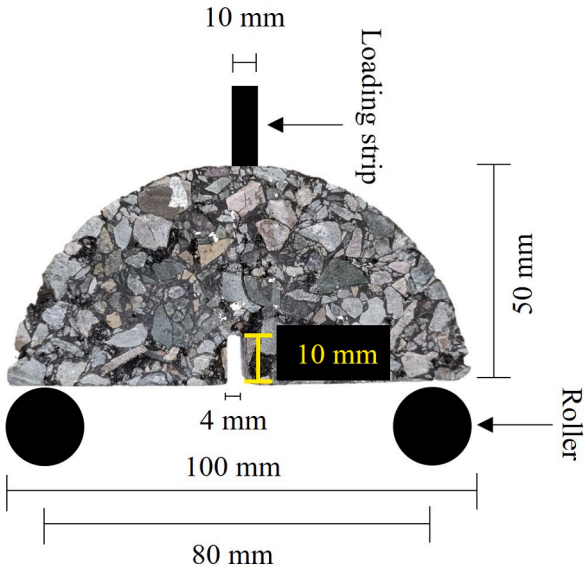

Fig. 2. Semi-circular bending test.

Previous researchers have investigated the influence on mechanical properties of freeze–thaw cycles on asphalt using semi-circular bending and 3-point bending tests at low temperatures. Semi-circular bending is one of the most popular tests to characterise the cracking resistance of asphalt and its mechanical properties such as fracture energy, tensile strength, critical strain energy release, and flexibility index [13]. Moreover, it is also used to characterise the fracture toughness to evaluate the crack resistance and propagation [14,15]. The most recent studies have focused on the long-term effect of freeze–thaw cycles on asphalts [1,6] and the influence of water saturation on fatigue performance [2].

The asphalt's internal structure evolution under freeze–thaw cycles has been previously evaluated using X-ray computed tomography [16,17,18]. This technology allows a micro-scale characterisation to quantify porosity, tortuosity, void circularity, and roundness [17,18]. For example, Özgan and Serin showed an increase of 40% in air void content after 24 days of freeze–thaw cycles [3]. Xu et al. investigated asphalt's internal structure changes under freeze–thaw conditioning using X-ray computed tomography (X-ray CT) technology [9]. Although previous researchers have investigated the influence of freeze–thaw cycles on asphalt degradation, the literature still lacks a comprehensive study on the role of the void's properties and its evolution under freeze–thaw cycles on asphalt performances. Consequently, the water retained in the asphalts varies, causing further modification and property losses. By establishing the correlation between topological changes of voids and mechanical properties losses under freeze–thaw cycles, we will be able to improve our design and prevent damage and failure.

Therefore, the current study seeks to establish a correlation between changes in the mechanical properties of asphalt and changes in the topological properties of voids due to freeze–thaw cycles. This was accomplished by quantifying the mechanical properties of asphalts in dry and wet conditions with a variety of void contents and changes in the internal structure caused by freeze–thaw cycles.

2. Materials and methods

2.1. Specimen preparation

Three asphalt mixture types were manufactured, following BS EN 12697–33 and BS EN 12697–35 [19,20]. Recipes have been selected to represent dense asphalt and a porous asphalt with voids higher and lower than the percolation threshold. All mixtures were compacted to refusal; therefore, the aggregate size and gradation were modified to produce the different air void contents.

Crushed granite aggregates with a maximum size of 20 mm and 60/40 pen bitumen were used for all mixtures. The aggregate gradation and binder contents of asphalts are shown in Table 1. The materials were mixed at 165 ℃ and roller compacted at 165 ℃. Sixteen asphalt slabs of 300 mm × 300 mm × 60 mm were produced with target air voids 3%, 9.8% and, 14%, respectively.

Cylindrical specimens with 100 mm diameter and 60 mm in height were extracted from slabs. The specimens were trimmed by 10 mm on the top and 10 mm on the bottom of the cores using a core saw. 80 cores of 100 mm diameter and 40 mm height were extracted, five cores per slab.

Moreover, two semi-circular specimens were obtained from each core by cutting them along their diameter. A vertical notch of 10 mm with a tolerance of ± 1 mm was introduced along the symmetrical axis with a thickness of 4 ± 0.5 mm to investigate fracture properties.

2.2. Freeze-thaw cycles test method

See the scheme of the tests to investigate the mechanical and cracking resistance properties of asphalts under freeze–thaw cycles in Fig. 1.

The samples were tested in dry and wet conditions. In wet

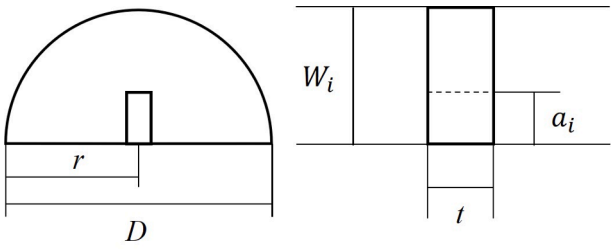

Fig. 3. Semi-circular asphalt specimen dimension.

conditions, the samples were submerged in water at 20 °C for 16 h and then wrapped in a transparent plastic film to keep the water in the samples. After, they were stored at −10 °C for 16 h and then at 20 °C for 8 h for the thawing part of the cycle. In dry conditions, the samples were kept in the air at −10 °C for 16 h and then at 20 °C for 8 h.

The specimens were subjected to up to 20 freeze–thaw cycles. Computed Tomography (CT) scans were taken before and after each cycle to evaluate the topology of void evolution. We CT scanned the same material in a range of cycles; hence, the statistical significance derived from the rate of change of the topological properties of the asphalts. The 3-point bending strength of the samples was measured at −10 °C using an INSTRON (a servo-hydraulic test apparatus) loading frame machine, according to BS EN 12697–44:2019 [21].

2.3. Semi-circular bending test

The semi-circular bending test was used to investigate the fracture properties of asphalt at −10 °C according to BS EN 12697–44 [21]. The parameters measured were peak load, F, young modulus, E fracture toughness, K_i, maximum stress to failure, σ, and fracture energy, G_f.

In this study, semi-circular bending test specimens were tested in a three-point bending load configuration supported by two rollers, with the distance between them 0.8 times the diameter of the semi-circular samples, see Fig. 2.

The load was applied monotonically on top of the specimen at a constant rate of 5 mm/min until material failure occurred and test results were recorded along with the deformation of the specimen (load vs displacement). The peak load at which the specimen fails was also determined.

The maximum stress at failure [21], σ_m, was calculated with:

$$\sigma_m = \frac{4.263xF}{Dxt} \tag{1}$$

where D, t and F are the specimen diameter, m, sample thickness, m of the semi-circular asphalt specimen, and peak load, N, on the sample, see Fig. 3.

The fracture toughness, which describes the material's resistance to fracture, K_i, is calculated as shown in reference [21]:

Table 2
Topology of voids after freeze–thaw cycles, in wet conditions.

Sample (target voids content)	Freeze-thaw Cycle	Air void content (%)	Mean void diameter (mm)	Mean void area (cm^2)	Void perimeter (mm)	Voids Aspect ratio (-)	Voids circularity (-)	Roundness (-)	Euler number	Tortuosity
3%	New	2.96	1.84	603	5.21	1.9	0.72	0.62	1182	0.92
	FT1	3.28	1.67	666	4.85	1.92	0.72	0.61	1358	0.91
	FT2	3.72	1.69	756	4.8	1.94	0.71	0.61	1269	1.30
	FT3	3.23	1.33	656	4.05	1.85	0.75	0.65	1924	1.25
	FT5	3.23	1.33	656	4.05	1.85	0.75	0.65	1967	1.44
	FT20	6.20	1.31	967	5.72	2.01	0.71	0.61	355	0.99
9.8%	New	9.47	4.74	1827	7.9	2.02	0.68	0.6	181	1.43
	FT1	11.48	4.44	2220	7.08	2.06	0.7	0.62	−779	1.69
	FT2	13.34	4.38	2585	7.26	2.13	0.71	0.61	−1304	1.62
	FT3	15.99	4.09	3090	6.76	2.09	0.74	0.63	−2005	1.47
	FT5	15.00	8.90	2900	8.12	2.52	0.64	0.56	−260	1.59
	FT20	14.10	11.62	2757	8.12	2.34	0.66	0.6	−358	1.23
14%	New	13.95	5.40	2927	10.5	2.13	0.59	0.56	−1851	1.58
	FT1	16.16	5.46	3396	10.2	2.09	0.61	0.57	−2248	1.52
	FT2	15.09	5.04	3145	9.53	2.08	0.62	0.58	−1605	1.57
	FT3	16.95	4.48	3539	8.59	2.01	0.66	0.61	−2340	1.47
	FT5	20.56	5.70	4328	10.04	1.99	0.68	0.62	3225	1.35
	FT20	19.78	9.37	4073	11.6	2.17	0.63	0.79	−1871	1.30

FT: freeze–thaw cycles.

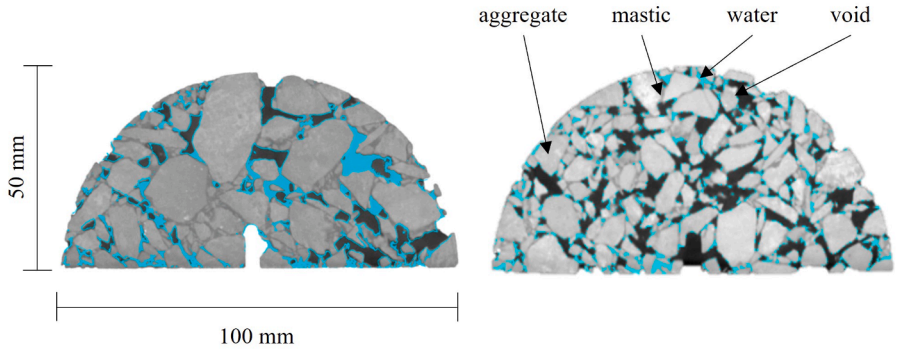

Fig. 4. Example of water retained in the asphalt pores, 9.8% (a) and 14% (b). Blue is described the water retained in the pores, gray is the mastic and aggregates, and black are the voids. (For interpretation of the references to colour in this figure legend, the reader is referred to the web version of this article.)

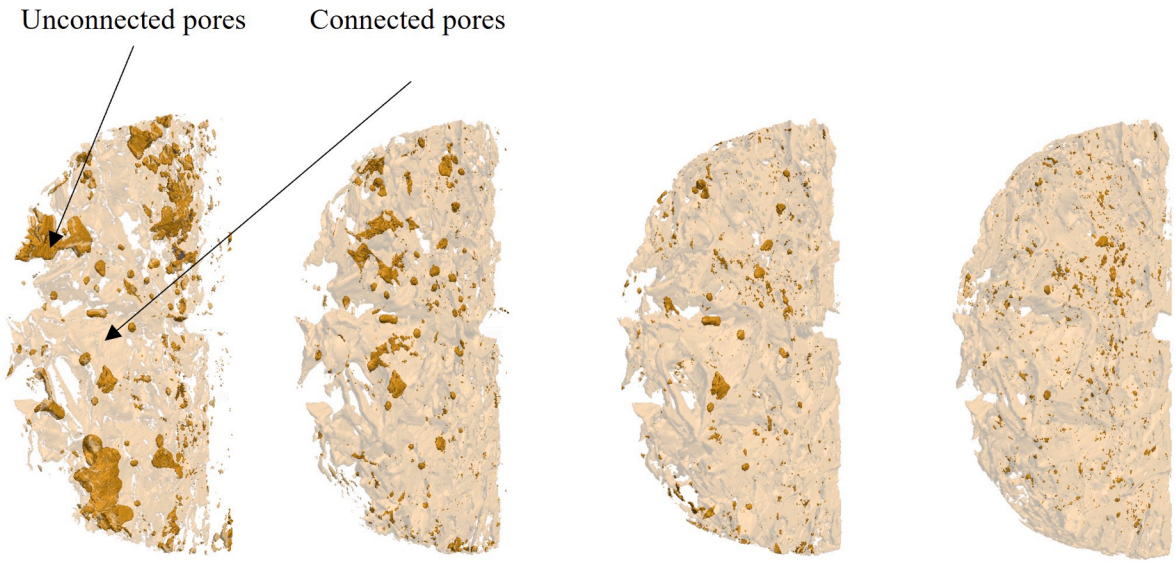

Fig. 5. Evolution of voids with freeze–thaw cycles: Total pores in (a) new (dry) condition and after (b), 1st cycle (c), 2nd cycle (d), 3rd cycle.

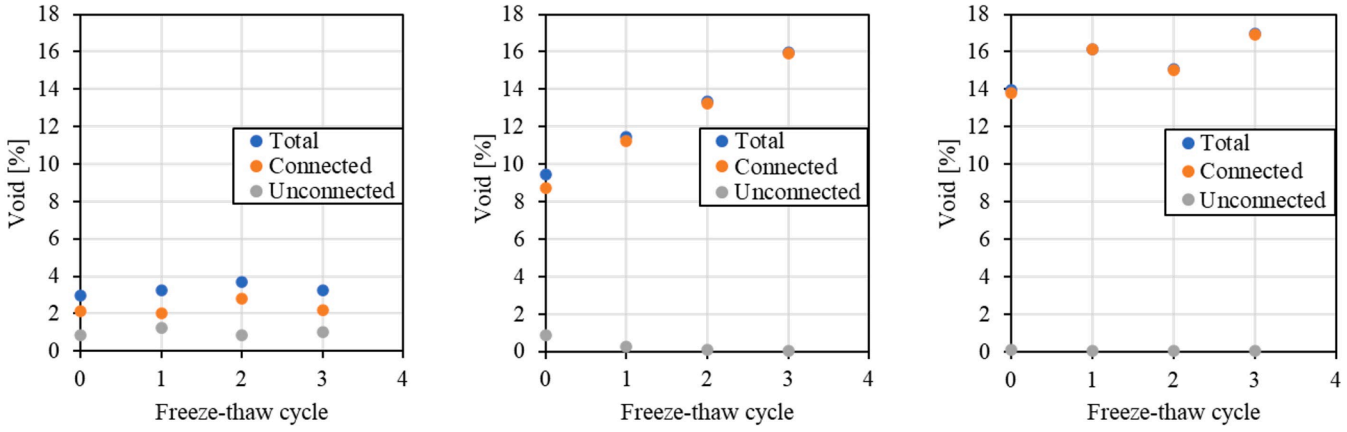

Fig. 6. Void content percentage against freeze–thaw cycles (in wet conditions) for asphalts with target air voids (a) 3%, (b) 9.8%, (c) 14%. Blue points represent the total void content, orange points represent the connected void content, and grey points represent the unconnected void content.

$$K_i = \sigma_m x f\left(\frac{a_i}{W_i}\right) \tag{2}$$

where W_i, a_i, and $f(\frac{a_i}{W_i})$ are the height of the specimen, the notch length, both in mm, and a geometric factor, see Fig. 3. The geometric factor $f(\frac{a_i}{W_i})$ is 5.956, for $9 < a_i < 11$ mm and $70 < W_i < 75$ mm. For other a_i and W_i values, the geometric value can be calculated according to the formula presented in reference [21]:

$$f\left(\frac{a_i}{W_i}\right) = -4.9965 + 155.58\left(\frac{a_i}{W_i}\right) - 799.94\left(\frac{a_i}{W_i}\right)^2 + 2141.9\left(\frac{a_i}{W_i}\right)^3 - 2709.1\left(\frac{a_i}{W_i}\right)^4 + 1398.6\left(\frac{a_i}{W_i}\right)^5 \tag{3}$$

The fracture energy [22] is the energy released during cracking, obtained as the area below the load–displacement curve until the specimen is broken following the Equation:

$$G_f = \frac{W}{A_{lig}} \tag{4}$$

Where W and A_{lig} are the work of fracture and the ligament area defined as.

$$A_{lig} = (r - a_i)xt \tag{5}$$

Where, a and t are specimen radius, in m, notch length, in m, and specimen thickness, in m, respectively, see Fig. 3.

2.4. Images acquisition and processing of X-ray CT

The asphalt samples were scanned using a Phoenix v|tome|x L 300 micro CT scanner; the X-ray tube used was (MXR320HP/11, 3.0 mm Be + 2 mm Al from GE Sensing and Inspection Technology) operating with an acceleration voltage of 290 kV and a current of 1300 mA.

The samples were positioned at 906.84 mm from the X-ray source

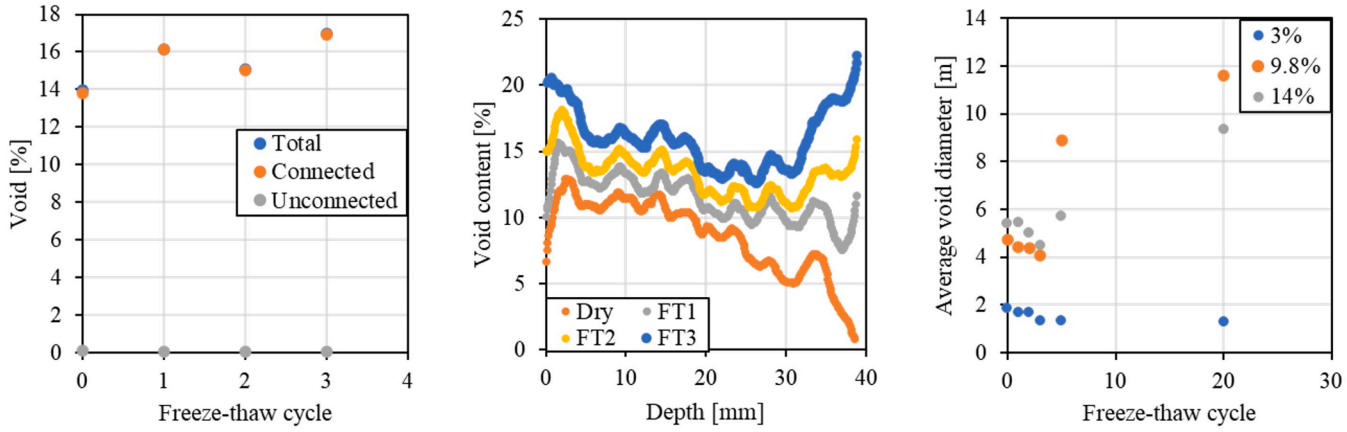

Fig. 7. (a) Average diameter evolution with freeze–thaw cycles. (b) Void content for asphalt with target voids 9.8% against depth. (c) Average void diameter per freeze–thaw cycle.

Table 3
Topology of voids changes rate due to the freeze–thaw cycles.

	Sample (target voids content)	Air void content (% / cycle)	Mean void diameter (mm / cycle)	Mean void area (cm^2 / cycle)	ΔVoids Aspect ratio / cycle	Euler number / cycle	Tortuosity / cycle
Fast damage stage	3%	0.125	−0.151	24.90	−0.013	213.7	0.138
	9.80%	2.142	−0.201	415.50	0.028	−708.3	0.030
	14%	0.793	−0.318	158.50	−0.037	−82.4	−0.028
Slow damage stage	3%	0.158	−0.019	16.34	0.006	−55.8	−0.004
	9.80%	0.111	0.366	23.23	0.013	17.9	−0.017
	14%	0.223	0.220	42.98	0.005	5.9	−0.012

and mounted on a rotational table. The scan images were reconstructed using the GE Datos|x reconstruction software with 2x resolution obtaining a spatial resolution of 45.2 mm; the scans had an isotropic resolution, meaning that the slice thickness was also 45.2 mm.

The original images were in 16-bit (.tiff format), and the voxel value represented the x-ray attenuation, then are processed with the software tools VG studio max and ImageJ, Version 1.8.0 [23,24], and converted to 8-bit grayscale resolution.

The different components of the samples, such as aggregates, mastic, and air voids, were separated by segmenting the materials based on grayscale thresholding using ImageJ. Based on experience, we considered that small isolated clusters with<0.5 mm could be small voids or noise effects and were removed from the image. The segmented images of the air voids were stacked using the software VGSTUDIO MAX, to generate 3D surfaces.

2.5. Density

The test specimens' asphalt mixture density and bulk density were calculated according to BS EN 12697, part 5 [19] and part 6 [19], respectively.

2.6. Air voids content

The air voids content of the samples has been calculated according to Equation (6) [19].

$$V_s = \frac{\rho_m - \rho_b}{\rho_m} \tag{6}$$

where V_s is the air void content of the sample, %, ρ_m is the maximum density of the mixture, kg/m^3, and ρ_b, the bulk density of the test sample, kg/m^3.

2.7. Connected air voids

There are two categories of voids in the asphalt: connected voids and unconnected voids.

Connected voids have at least one end communicating with the external surface and allow water to pass through them. One particular case of connected voids is the dead-end voids with only one end connected to an external surface and retaining water. Unconnected voids do not communicate with the external surface. In this study, we are interested in the connected voids.

The VG studio max software has been used to identify the connected and dead-end voids connected to one of the surfaces.

2.8. Mean void diameter

The mean void diameter, V_{mean}, has been obtained using a thickness algorithm within the Particle Analyser plugin [24] (Version 1.4.3) in Fiji and calculated as:

$$V_{mean} = \frac{\sum_{i=1}^{n} d_i V_i}{\sum_{i=1}^{n} V_i} \tag{7}$$

where, d_i is the diameter of each single void and, V_i is the volume of each pore in the sample.

2.9. Mean void area

The Mean void area is calculated by converting the pores into meshes with triangular shapes and measuring the total surface area of pores and their volume. It was done using the BoneJ surface area [24] plugin (Version 1.4.3). The mean void area is calculated using the Equation:

$$Meanvoidarea = \frac{A}{V} \tag{8}$$

Where A is the total surface of pores and V the volume of the specimen.

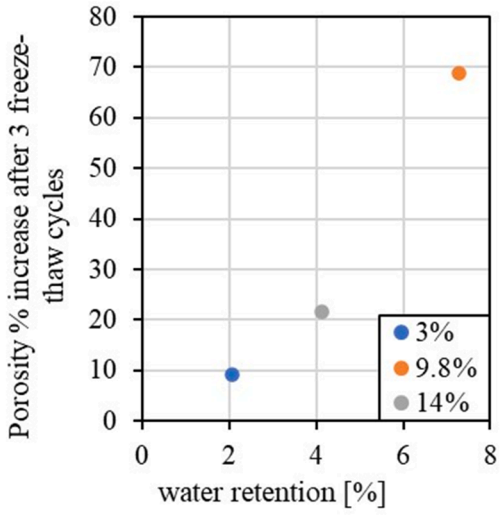

Fig. 8. Water retention [%] at the first cycle versus porosity increase.

2.10. Aspect ratio

The aspect ratio of a void is the ratio between its largest and smallest orthogonal diameters. The aspect ratio's value (A_r) has been obtained using the shape descriptor algorithm within the Particle Analyser plugin [25] (Version 1.4.3) in Fiji and calculated as:

$$A_r = \frac{d_{max}}{d_{min}} \quad (9)$$

Where d_{max} and d_{min} are the largest and smallest orthogonal axis, respectively.

2.11. Circularity

The circularity (*Circ*) has been obtained using the shape descriptors algorithm within the Particle Analyser plugin [25] (Version 1.4.3) in Fiji and calculated as:

$$Circ = \frac{4\pi A}{P^2} \quad (10)$$

Where A is the area and P is the perimeter. A value of 1 means the void is a perfect circle, and a value closer to 0 indicates that the void is elongated.

2.12. Roundness

The roundness measures how similar is the shape of an object to a perfect cycle and it is calculated using the shape descriptors algorithm within the Particle Analyser plugin [25] (Version 1.4.3) in Fiji as:

$$Round = \frac{4A}{\pi {d_{max}}^2} \quad (11)$$

Where A is the area and d_{max} the largest orthogonal axis.

2.13. Tortuosity

Tortuosity, T, is defined as the height of the test specimen to the minimum distance between the two ends of specimen:

$$T = \frac{L_p}{L_s} \quad (12)$$

Where T is the tortuosity, L_p is the total length of pore and, L_s is the shortest distance between the two ends of samples.

The values were obtained with the Skeletonize 2D/3D and Analyse Skeleton modules in ImageJ [25], with no pruning of the dead ends.

2.14. Euler number

The Euler number is the function of the number of isolated air voids, N, the number of redundant connections in air paths, C, and closed cavities, H. A negative Euler number means the air voids are percolated [26,27,28]. These parameters were determined with the BoneJ particle analyser plugin (Version 1.3.11) in ImageJ [25].

$X = N\text{-}C + H$ (13).

3. Results and discussion

3.1. Internal structure evolution of asphalt mixtures during freeze–thaw cycles

Table 2 shows how the topology of voids changes after each freeze–thaw cycle in asphalt that had been previously submerged in water. These values have been obtained from CT-Scans and are the average properties of each CT-Scan. We have selected mixtures with target air voids 3%, 9.8% and 14%, due to their high difference in voids content, which are representative of dense, semi-dense and porous asphalts. Please note that referring to samples as "new" implies that they were tested in dry conditions prior to being frozen and thawed.

Besides, to have a visual idea of how the water is retained in the asphalt, Fig. 4 shows the presence of water in asphalts with 9.8% target air voids and 14% target air voids after they have been submerged and removed from the water. This figure shows that the voids are not full of water, which is retained only in the dead-end voids and the narrowest areas.

The voids in asphalt can be connected or unconnected [29]. They are unconnected when they do not communicate with the atmosphere and connected when they communicate. According to previous studies [30], connected pores are the only types that allow water to penetrate through the asphalt during freeze–thaw cycles. Therefore, in this study, we identified the connected and unconnected pores to determine their influence on the effect of freeze–thaw cycles on asphalt's durability. Fig. 5 (a) illustrates the asphalt's connected and unconnected air voids, with a target air void percentage of 9.8%. Before the specimen was subjected to freeze–thaw cycles, the mixture had 8.7% connected voids and 0.86% unconnected voids. After three freeze–thaw cycles, the mixture had 15.9% connected voids and 0.05% unconnected voids. With every cycle, the asphalt became more porous, which increased the amount of water damage with each freeze–thaw cycle.

Moreover, Fig. 5 shows the void content evolution with the freeze–thaw cycles of the three types of asphalt studied, highlighting the connected and unconnected voids since that may help understand their evolution with the number of freeze–thaw cycles. With the freeze–thaw cycles, the total voids and the connected voids increased in every asphalt studied, and the unconnected voids decreased. The unconnected voids in the mixture with target air voids 3% remained approximately stable during the freeze–thaw cycles, while the connected voids increased from approximately 2.12% to 2.8%. For the mixture with target air voids 9.8%, the total voids content increased from 9.5% to 14.1%, which are 48% more. Furthermore, the unconnected voids reduced from 0.86% to 0.05%, and the connected voids increased from 8.7% to 15.9% in three freeze–thaw cycles, a growth of 83%. In addition, in the mixture with 14.0% void content, the connected porosity increased up to 16.9%, a growth of 22%.

In reference [30], the authors divided the evolution of voids during freeze–thaw cycles into three arbitrary stages (i) initial stage, (ii) steady increase stage and (iii) increase stage; however, in this paper, it is unclear what each of these stages means and, the number of cycles in each stage varied depending on the type of asphalt mixtures. Moreover, in [6], the stiffness of the asphalt they studied reduced steadily until approximately the 5th freeze–thaw cycle and after, the stiffness

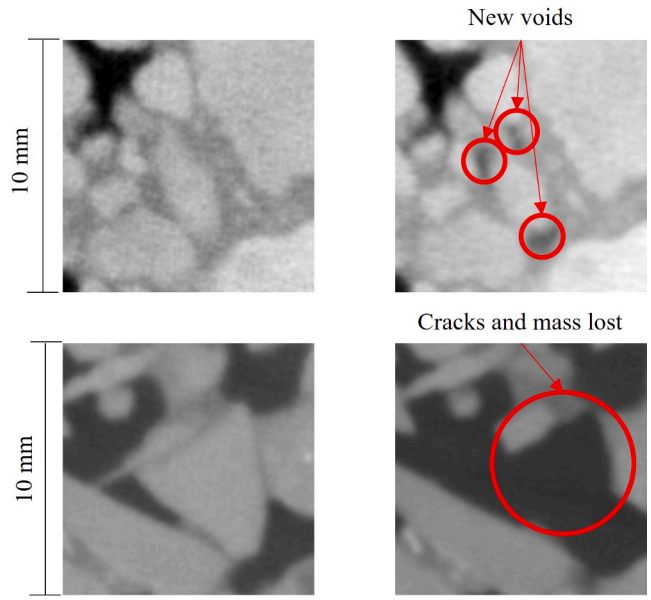

Fig. 9. CT scan of new asphalt and damaged after 20 cycles. (a) Asphalt with target voids 9.8% before the freeze–thaw cycles. (b) Asphalt with target voids 9.8% after 5 cycles. (c) Asphalt with target voids 14% before the freeze–thaw cycles. (d) Asphalt with target voids 14% after 20 cycles.

remained steady with additional freeze–thaw cycles. Hence, the authors have tested the evolution of voids in asphalts for 20 freeze–thaw cycles and, based on observation, decided to divide the freeze–thaw cycles into two stages: (i) fast damage stage and (ii) slow damage stage.

In Table 3, we describe the rate of change of topological properties of the asphalts, ranging from 0 to 3 cycles, to describe the fast damage stage and from 0 to 20 cycles to describe the slow damage stage. We have used Fig. 7 (a), which shows the evolution of air voids for the three types of asphalt analysed with the number of freeze–thaw cycles, to select the range of freeze–thaw cycles for the fast and the slow damage stages.

The first remarkable aspect observed in Table 3 and Fig. 7 (a) is that the air voids content increased for every asphalt studied during the freeze–thaw cycles. The average rate of air voids increase was 1.02%/cycle in the fast damage stage and 0.16 %/cycle in the slow damage stage. In general, it can be observed that the voids increase linearly with the freeze–thaw cycles at a rate of 0.12 %/cycle for the asphalt with target voids of 3%, 2.14 %/cycle for the asphalt with target voids of 9.8% and 0.79 %/cycle for the asphalt with target voids 14%. The asphalt with a target air void of 9.8% suffers greater damage than the rest of the test samples during the fast damage stage [32]. Besides, Fig. 7 (b) shows how the voids change with the depth of the specimen (thickness, which is the *t* dimension in Fig. 3) in asphalt with 9.8% voids content. This mixture had segregation, as seen in the connected voids that reduced with the height. However, the voids increased and became progressively connected with the cycles, which gives an idea of how the asphalt gets damaged due to freeze–thaw cycles under wet conditions.

To explain the higher increase of porosity in the mixture with target air voids 9.8%, Fig. 8 correlates the increase in porosity with the water retained in the three asphalts studied. We found using the CT scans that the percentages of water retained by weight of the asphalts are 2.05%, 7.28%, and 4.13% for the mixtures with 3%, 9.8%, and 14% target voids, respectively. Hence, there is a linear relationship between the amount of water retained in the asphalt and the physical damage it suffers in each freeze–thaw cycle, suggesting that to minimise the freeze–thaw damage, the internal structure of the pores plays a key role.

As a result of the higher water retention rate, asphalt with 9.8% target voids has the highest increase of porosity and area in the fast damage stage, see Table 3, which is similar to the results reported in [10]. However, in this mixture, the diameter of the voids decreased, which indicates the creation of several small pores or cracks with a small diameter. Besides, it is interesting that the mixture with target voids of 3% had the lowest rate of void diameter increase, which, as can be observed in Table 3, must be related to having the lowest water retention rate. In general, in Table 3, we can observe that during the fast damage stage, the void diameter decreased for all the asphalts analysed, which could indicate the creation of new voids and cracks in the material, which were smaller than the existing voids; for example, see examples in Fig. 9 (a) and Fig. 9 (b), for the asphalt with 9.8 target voids content.

In the slow damage stage, after the third freeze–thaw cycle, cracks widened, which caused some aggregates to fall through the voids; see Fig. 9 (c) and (d) for an example. In this stage, the voids area increased for the three mixtures studied, and the tortuosity decreased steadily, which could be due to voids coalescing and creating bigger voids, as explained in reference [10]. For example, for the mixture with a target air void of 3%, in 20 cycles, the voids increased steadily from 2.96% to 6.2%, and the Euler number and tortuosity decreased, reflecting that the pores were better connected, and cracks started to appear. It is expected that when the voids topologies of the mixture with target air void 3% become like those of mixture with target air void 9.8%, more water will be retained, and there will be a sudden increase of damage, which may explain why some dense asphalts that have been several years in service get suddenly damaged after a cold day. This has been reported before in reference [6], where the asphalts resist several freeze–thaw cycles until they break suddenly.

Furthermore, from Table 3, it is apparent that the initial aspect ratio of the voids in all the asphalts studied is greater than 1, implying that the voids are not circular; with each freeze–thaw cycle, the aspect ratio decreases and the voids become circular. If the aspect ratio increases, it can be inferred that cracks are more prevalent than new pores, which would be reflected by a negative increase in the asphalt ratio. The rate of growth of the aspect ratio for the mixture with 9.8% voids content is positive. Hence, during the fast damage stage, the formation of cracks is predominant in this mixture. Also, see how the Euler number decreases, meaning more connectivity in the pores. In the other two mixtures, the voids became rounder, reflecting the formation of new small unconnected voids in the asphalt. Finally, the aspect ratio increased steadily with the cycles in the slow damage stage, which implies that the cracks grew gradually.

We analysed the R^2 values of topological properties from Table 2 versus the number of cycles in wet conditions to confirm the results. A R^2 value of 1 indicates a direct correlation between two variables, while a

Table 4
R^2 values of the void's topological values versus the freeze–thaw cycles in wet conditions.

	Sample (target voids content)	Air void content	Mean void diameter	Mean void area	ΔVoids Aspect ratio	Euler number	Tortuosity
Fast damage stage	3%	0.263	0.819	0.256	0.189	0.678	0.727
	9.80%	0.994	0.948	0.995	0.603	0.986	0.003
	14%	0.616	0.832	0.570	0.916	0.096	0.509
Slow damage stage	3%	0.927	0.401	0.845	0.464	0.466	0.012
	9.80%	0.136	0.801	0.154	0.300	0.035	0.594
	14%	0.460	0.894	0.404	0.219	0.000	0.684

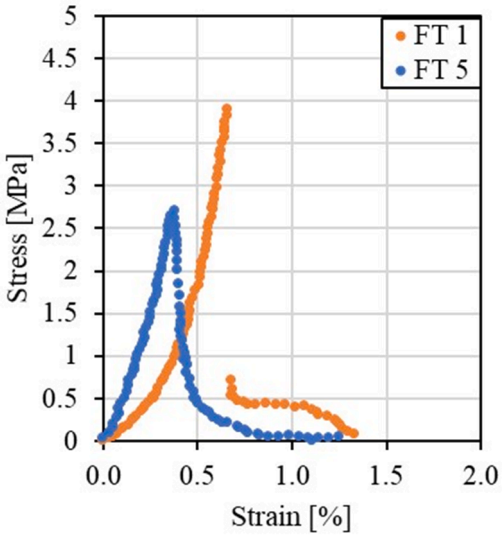

Fig. 10. Examples of stress–strain curves for the asphalt with 9.8% air voids content.

R^2 value of 0 indicates no correlation between the variables. In the fast damage stage for semi-open and open asphalts, the R^2 value is close to 1 for most properties, indicating a clear trend of change with the freeze–thaw cycles and confirming that damage occurs in this stage for these two types of asphalt. Moreover, in the slow damage stage, the topologies of dense asphalt strongly correlated with the number of cycles, confirming that dense asphalt degraded slowly with the cycles in wet conditions. However, semi-dense and porous asphalt showed lower correlations, which confirms that most of the damage in these materials occurred during the fast damage stage, as shown in Fig. 6. Furthermore, the authors appreciate that the Euler number and tortuosity may change with the number of cycles, as it was mentioned above; however, one cannot appreciate a clear trend in the data shown in Table 4.

3.2. *Effect of freeze–thaw cycles on the asphalt's mechanical properties*

An example of the semi-circular bending test results of asphalt with 9.8% of void content is shown in Fig. 10. The stress–strain curve followed a brittle behaviour; the load increased with compression with a brittle and sudden fracture after the load reached the peak force, exceeding the bearing capacity of the material.

Fig. 11 shows the evolution of various mechanical properties such as peak load, see Fig. 11(a), Young modulus, Fig. 11(b), fracture toughness, Fig. 11(c), and fracture energy, Fig. 11(d), with the freeze–thaw cycles. The four mechanical properties reflect the fast and slow damage stages that we mentioned above, where the mechanical properties degrade with the first five cycles; in this case, it can be seen that the fast damage stage lasts between 3 and 5 cycles, while the damage growth rate is reduced in the slow damage phase, as expected [32]. Moreover, in Table 5, the data from Fig. 11 have been presented to allow easy comparison to the topological values from Table 2. As established in Table 3, the reduction rate depended on the initial internal structure of asphalt.

As seen in Fig. 9, with the increase in freeze–thaw cycles, new voids are created, cracks are formed, and aggregates are lost in the voids, which increases the connected voids [9]. Moreover, increased air-voids content provides space for frost heaving generated by subsequent freeze–thaw cycles and slows the damage growth, as seen in Table 3. A similar reduction of mechanical properties was presented in [1,5,31], with an initial reduction of fracture toughness and a plateau after the fifth cycle. Furthermore, in [12], the Young modulus and fracture toughness dropped about 30% after one freeze–thaw cycle and slowly reduced.

In previous studies, it was found that asphalts with porosity ranging from 6% to 13% have, in general, lower durability than other asphalts [2,3,5,6,9]; in general, most of these studies did not consider the topology of pores in the asphalt and the changes that occur to these voids in the freeze–thaw cycles. As shown in Table 2 and Fig. 8, the asphalt with 3% air void content is characterised by having the smallest void diameter, highest Euler number, and lowest water retention rate. The asphalt with 9.8% air void content has an intermediate voids diameter, Euler number and the highest water retention rate. Finally, the asphalt with 14% of air voids has the highest voids diameter, smallest Euler number and an intermediate water retention rate. The authors found linear correlations between the mechanical and some of the topological properties of the pores at the range of freeze–thaw cycles studied. The Pearson correlations have been presented in Table 6.

Reference [29] shows a strong and direct positive correlation between the air voids content, voids diameter or perimeter and volume of the biggest air void and Euler number. Hence, we refer to these properties by referring to the air void content. In Table 6, we observe a strong negative correlation between the air void content and the peak load, Young modulus, and fracture toughness of the asphalts. During the fast-damage stage, all of these properties declined with increasing air void content regardless of the gradation, asphalt composition, or previous freeze–thaw cycles. Based on this, it could be possible to approximately predict the freeze–thaw durability of asphalt by simply measuring its voids content, and one can conclude that the main source of low durability for the asphalt during the freeze–thaw cycles is the physical damage it suffers from increasing its voids size and content. Moreover, despite the high reduction rate in the fast damage stage, the mechanical properties did not undertake additional damage, reaching a steady stage, which indicates that asphalt with higher void content has the highest long-term durability. The tortuosity influences also the mechanical properties indicating that asphalt with more twisty void shapes, with lower circularity and higher aspect ratio, has lower ultimate strength, fracture toughness and fracture energy. Finally, the fracture energy shows the same trend as the rest of the mechanical properties studies; however, it does not seem to be strongly correlated to any of the topological properties being considered, which may occur because this property is related to the mastic properties rather than to the asphalt's gradation.

Besides, Fig. 12 shows the slope of the percentage reduction of peak load, young modulus, fracture toughness and fracture energy during the first three freeze–thaw cycles. This figure shows the asphalt that reduced its mechanical properties most due to freeze–thaw, regardless of the initial strength of the material.

The peak load, fracture toughness and fracture energy of asphalt with target air voids content of 9.8% reduced the most; the Young modulus, defined as the relationship between the peak load and the deformation at the peak load, did not reduce as much as in the other two materials, probably because the asphalts broke before the deformation could reach a high value. From Table 2, it can be observed that the topological properties of air voids in the asphalt with target voids of 9.8% are not higher than those of the asphalt with target air voids of 14%. The only difference between both asphalts was the water retained, which was 2.05%, 7.28% and 4.13% by total weight in the mixtures with target air voids of 3%, 9.8% and 14%, respectively. Hence, one can conclude that the capacity to retain water by the asphalts is a key factor regarding its durability to freeze–thaw cycles.

Fig. 13 displays the fracture toughness reduction rate per cycle for all samples in dry and wet conditions after three cycles. The result shows that the asphalt tested in wet conditions has the highest strength reduction within three cycles; hence, this figure demonstrates the damage caused by water to the asphalt during the freeze–thaw cycles. Interestingly, in dry conditions, the asphalt with target air voids of 3% suffers the greatest damage, possibly due to the highest amount of bitumen, which has a different coefficient of thermal expansion compared to the aggregates. Aggregates and bitumen contract and

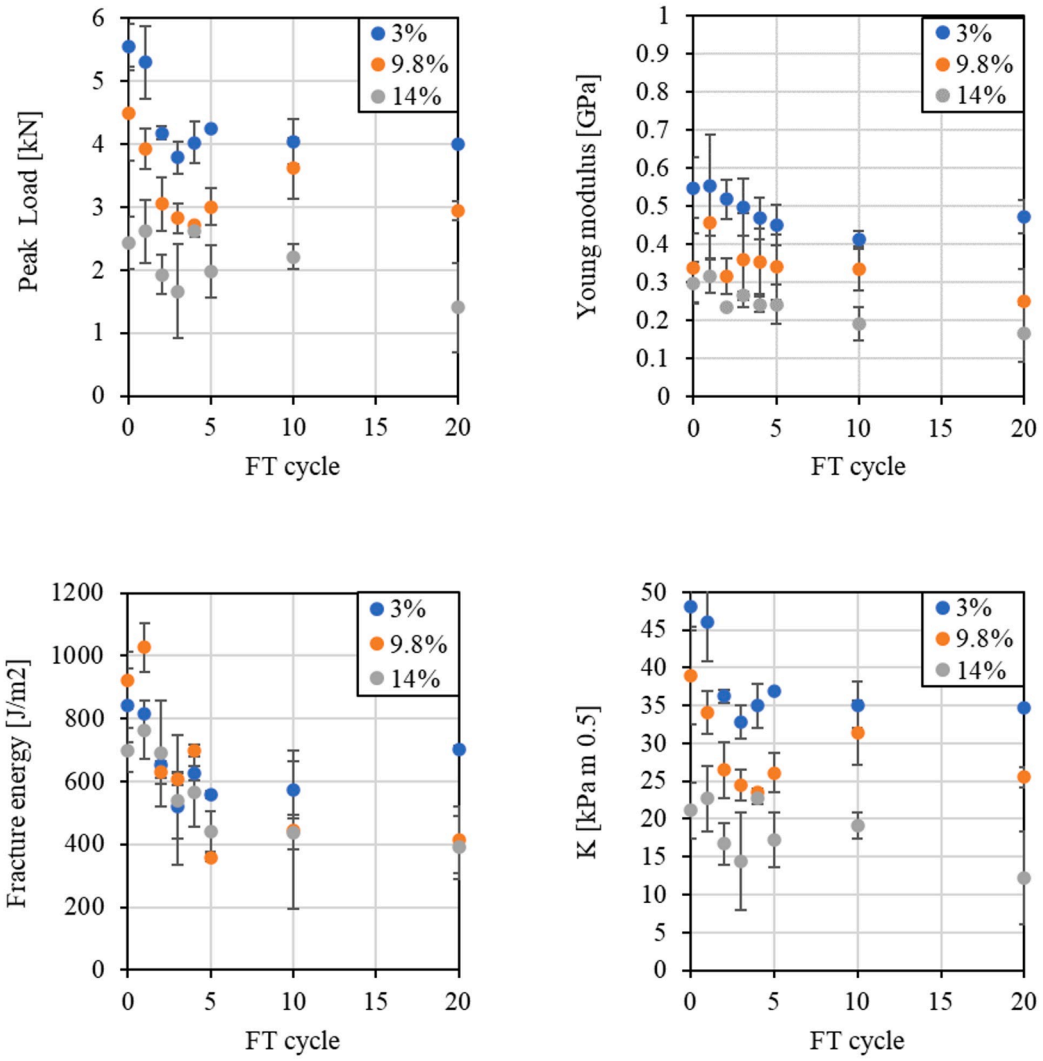

Fig. 11. Evolution of (a) Peak load, (b) Young modulus, (c) Fracture toughness, (d) Fracture energy with the freeze–thaw cycles.

Table 5
Mechanical properties of the test samples examined.

Sample (target voids content)	Values Freeze Cycle	Peak load (kN)	Young Modulus (GPa)	Fracture toughness (kPa m 0.5)	Fracture energy (J/m^2)	Standard deviation Peak load (kN)	Young Modulus (GPa)	Fracture toughness (kPa m $^{0.5}$)	Fracture energy (J/m^2)
3%	New	5.54	0.55	841	48.14	0.37	0.08	117	3.23
	FT1	5.29	0.56	814	45.97	0.58	0.13	246	5.05
	FT2	4.17	0.52	651	36.23	0.10	0.05	39	0.90
	FT3	3.78	0.50	521	32.84	0.25	0.07	104	2.17
	FT5	4.25	0.45	558	36.92	0.01	0.05	11	0.07
	FT20	4.00	0.47	704	34.76	0.02	0.05	10	0.07
9.8%	New	4.48	0.34	921	38.93	0.74	0.09	91	6.43
	FT1	3.92	0.46	1027	34.03	0.32	0.10	77	2.80
	FT2	3.05	0.32	628	26.46	0.42	0.05	37	3.67
	FT3	2.82	0.36	609	24.53	0.24	0.12	21	2.07
	FT5	3.00	0.34	359	26.09	0.30	0.09	12	2.58
	FT20	2.94	0.25	414	25.54	0.15	0.08	107	1.34
14%	New	2.43	0.30	699	21.11	0.42	0.05	70	3.67
	FT1	2.61	0.32	763	22.70	0.50	0.05	93	4.30
	FT2	1.93	0.23	689	16.77	0.32	0.00	168	2.75
	FT3	1.67	0.27	540	14.47	0.74	0.01	206	6.47
	FT5	1.99	0.24	440	17.25	0.42	0.05	64	3.61
	FT20	1.40	0.17	390	12.19	0.71	0.07	101	6.17

Table 6
Pearson correlations between the samples' mechanical and topological properties, including new asphalt (dry condition) and, after going through freeze–thaw cycles.

	Air void content	Average void diameter	Volume of biggest air void	Void perimeter (%)	Voids Aspect ratio (%)	Voids circularity (%)	Euler	Tortuosity
Peak load (kN)	−0.89	−0.61	−0.90	−0.81	−0.45	0.64	0.77	−0.55
Young Modulus (GPa)	−0.91	−0.78	−0.91	−0.89	−0.55	0.70	0.75	−0.51
Fracture toughness (kPa m $^{0.5}$)	−0.89	−0.61	−0.90	−0.81	−0.45	0.64	0.77	−0.55
Fracture energy (J/m^2)	−0.40	−0.50	−0.40	−0.24	−0.43	0.14	0.08	−0.04

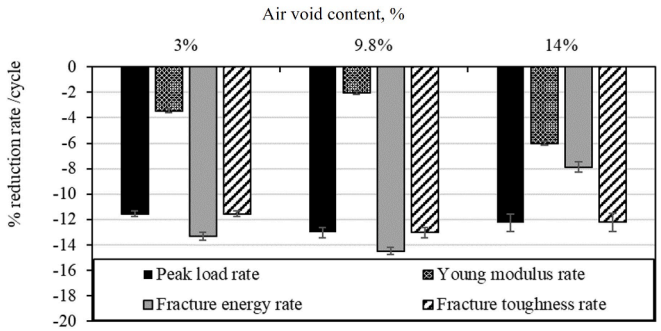

Fig. 12. Percentage of reduction per cycle for the: (a) Peak load, (b) Young modulus, (c) fracture toughness, and (d) fracture energy.

expand differently during the freeze–thaw cycles, causing stress during the freeze–thaw cycles. The results align with references [33,34]. These

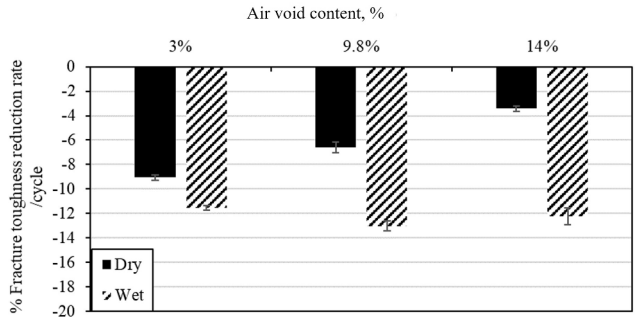

Fig. 13. Percentage of fracture toughness reduction per cycle for dry and wet conditions.

authors observed a drop in mechanical properties for asphalt with air void content of around 3%, concluding that the principal factors influencing degradation are bitumen content and aggregate type and shapes..

3.3. Summary

Fig. 14 shows how the damage progresses for the three types of asphalt analysed in the slow and fast damage stages.

In the asphalt with target air voids 3%, the connected voids increased gradually during the slow and fast damage phases, see Fig. 14 (a). During the slow damage phase, the unconnected voids content remained approximately stable, and the connected voids content increased gradually. As a result, the fracture toughness, fracture energy, Young modulus and peak load of the asphalt decreased [9]. This was the asphalt that retained less water, and hence, it was characterised by high fracture energy and resistance to low-temperature cracking. However, in dry conditions, this asphalt is the one that degrades the fastest.

In the asphalt with target air voids of 9.8%, the voids content grew approximately 48% in 20 cycles; the unconnected voids reduced to approximately none, while all the rest of the voids were connected, see Fig. 14 (b). This mixture retained the most water because it had a high content of open voids with one closed end. As a result, several cracks appeared, very fast during the fast damage phase and progressively during the slow damage phase [10,30]; these cracks coalesced to the extent that aggregates were lost. This resulted in the largest decrease in mechanical properties among all the asphalts studied [6].

Finally, the asphalt with target air voids of 14% retained less water than the previous one, and the ice had more room to expand; hence, the reduction in mechanical properties was lower [30]. The voids in this asphalt were mostly connected and increased their size and total air voids content with the freeze–thaw cycles. In dry conditions, this is the asphalt that degrades more slowly.

4. Conclusions

Several types of asphalt with acceptable air void contents ranging from 3% to 14% were examined for their influence during freeze–thaw cycles, where a correlation between differences in air void topology and changes in mechanical properties was established. According to the results in this study, the topological properties evolution under freeze–thaw cycles was influenced by three different phenomena: (1) volume increase of the existing voids and formation of small cracks, (2) voids coalescence, and (3) cracking and new voids formation. The voids were analysed using X-ray CT scans after every freeze–thaw cycle, and the mechanical properties were measured from 3-point bending tests. The following conclusions were obtained:

The three different asphalts had different behaviours when exposed to freeze–thaw cycles, attributed to the different aggregate size distributions and air void topologies. Hence, the durability of asphalt to freeze–thaw cycles could be controlled by carefully selecting the aggregate gradation, aggregate morphology and air void topologies.

The damage under wet conditions progressed in two stages; (i) fast damage stage and (ii) slow damage stage. The fast damage stage lasted approximately three freeze–thaw cycles and new voids and cracks formed rapidly; the peak load strength reduced fast too. The slow damage stage occurred after the fast damage stage, and the voids and cracks opened gradually. Therefore, the mechanical properties reduced gradually too.

In wet conditions, the asphalt with target air voids of 9.8% showed the highest level of damage in the fast damage stage and the lowest in the slow damage stage. The reason was that this asphalt retained the highest amount of water in the pores of all the three types studied. Water retention and air void content were among the main parameters influencing the durability of asphalt; hence, the durability of asphalt can be controlled with the gradation and mastic content. This result suggests that open grade asphalt may perform best in cold regions.

In wet conditions, the fast damage stage could not be appreciated in the asphalt with target air voids of 3%; the reason was that the voids in this mixture were not connected, and the water retained was minimal. Hence, damage progressed slowly and constantly in this asphalt, leading to sudden failure. The fast damage stage occurred in the mixtures where voids were connected, and the water retention by weight of the asphalt was high.

Unlike in wet conditions, in dry conditions, the asphalt with target air voids of 3% suffered the highest amount of damage during the

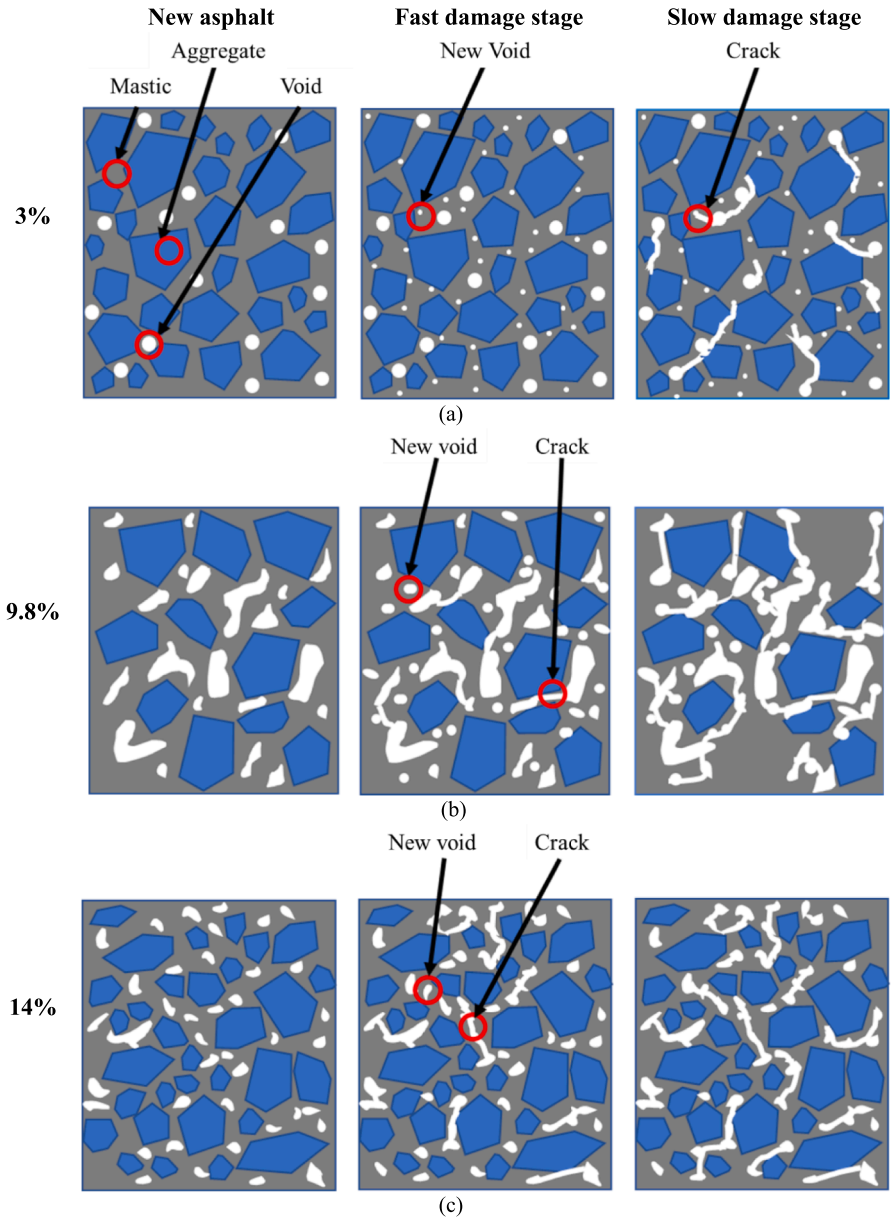

Fig. 14. (a) schematic representation of the three sample during the two stages: (a) 3%; (b) 9.8%; (c) 14%.

freeze–thaw cycles due to the higher amount of aggregates and bitumen and their thermal expansion.

Based on these findings, we can conclude that the internal void topology influences the mechanical properties of asphalt through freeze–thaw cycles; and that open grade asphalt may perform well in cold climates.

The initial water retention of the asphalt could be established as the index to determine the durability of the asphalt, with equal importance to measuring the air voids and macrotexture, as it is done at present.

Declaration of Competing Interest

The authors declare that they have no known competing financial interests or personal relationships that could have appeared to influence the work reported in this paper.

Acknowledgements

The first author acknowledges the funding of the Universities of Nottingham and Birmingham for the stipend and National Highways for the funding for experiments.

References

[1] M.M. Karimi, E.A. Dehaghi, A. Behnood, A fracture-based approach to characterise long-term performance of asphalt mixes under moisture and freeze-thaw conditions, Eng. Fract. Mech. 241 (2021), 107418.
[2] Z. Fan, H. Xu, J. Xiao, Y. Tan, Effects of freeze-thaw cycles on fatigue performance of asphalt mixture and development of fatigue-freeze-thaw (FFT) uniform equation, Constr. Build. Mater. 242 (2020), 118043.
[3] E. Özgan, S. Serin, Investigation of certain engineering characteristics of asphalt concrete exposed to freeze-thaw cycles, Cold Reg. Sci. Technol. 85 (2013) 131–136.
[4] S. Wu, R. He, H. Chen, Y. Luo, Low temperature characteristics of asphalt mixture based on the semi-circular bend and thermal stress restrained specimen test in alpine cold regions, Constr. Build. Mater. 311 (2021), 125300.
[5] M. Fakhri, S. Ali Siyadati, M.R.M. Aliha, Impact of freeze–thaw cycles on low temperature mixed mode I/II cracking properties of water saturated hot mix asphalt: An experimental study, Constr. Build. Mater. 261 (2020) 119939.
[6] M. Sol-Sánchez, F. Moreno-Navarro, G. García-Travé, M.C. Rubio-Gámez, Laboratory study of the long-term climatic deterioration of asphalt mixtures, Constr. Build. Mater. 88 (2015) 32–40.

[7] J. Yi, S. Shen, B. Muhunthan, D. Feng, Viscoelastic-plastic damage model for porous asphalt mixtures: Application to uniaxial compression and freeze-thaw damage, Mech. Mater. 70 (2014) 67–75.
[8] S. Badeli, A. Carter, G. Doré, Complex Modulus and Fatigue Analysis of Asphalt Mix after Daily Rapid Freeze-Thaw Cycles, J. Mater. Civ. Eng. 30 (2018) 04018056.
[9] L. Cong, M. Ren, J. Shi, F. Yang, G. Guo, Experimental investigation on performance deterioration of asphalt mixture under freeze–thaw cycles, Int. J. Transp. Sci. Technol. 9 (3) (2020) 218–228.
[10] H. Xu, W. Guo, Y. Tan, Internal structure evolution of asphalt mixtures during freeze-thaw cycles, Mater. Des. 86 (2015) 436–446.
[11] Y. Cheng, D.i. Yu, G. Tan, C. Zhu, Low-temperature performance and damage constitutive model of eco-friendly basalt fiber-diatomite-modified asphalt mixture under freeze-thaw cycles, Materials (Basel) 11 (11) (2018) 2148.
[12] J. Li, F. Wang, F.u. Yi, J. Ma, Z. Lin, Fractal analysis of the fracture evolution of freeze-thaw damage to asphalt concrete, Materials (Basel). 12 (14) (2019) 2288.
[13] C. Zhang, H. Wang, X.u. Yang, Low-temperature performance of SBS modified asphalt mixture in high altitude and cold regions, Int. J. Pavement Res. Technol. 12 (1) (2019) 33–42.
[14] G. Saha, K.P. Biligiri, Fracture properties of asphalt mixtures using semi-circular bending test: A state-of-the-art review and future research, Constr. Build. Mater. 105 (2016) 103–112.
[15] J. Ren, L. Sun, Characterising air void effect on fracture of asphalt concrete at low-temperature using discrete element method, Eng. Fract. Mech. 170 (2017) 23–43.
[16] S. Pirmohammad, A. Kiani, Study on fracture behaviour of HMA mixtures under mixed mode I/III loading, Eng. Fract. Mech. 153 (2016) 80–90.
[17] E. Masad, V.K. Jandhyala, N. Dasgupta, N. Somadevan, N. Shashidhar, Characterisation of air void distribution in asphalt mixes using X-ray computed tomography, J. Mater. Civ. Eng. 14 (2002) 122–129.
[18] M.E. Kutay, Modeling Moisture Transport in Asphalt Pavements(Ph.D Thesis), University of Maryland, College Park, US, 2005.
[19] N. Abdul Hassan, G.D. Airey, N.I. Nur, M.R. Hainin, R. Putrajaya, M.E. Abdullah, M.M.A. Aziz, Microstructural characterisation of dry mixed rubberised asphalt mixtures, Constr. Build. Mater. 82 (2015) 173–183.
[20] EN 12697-22. (2020). BSI Standards Publication - Bituminous mixtures - Test methods, Part 22: Wheel tracking.
[21] BSI Standards Publication Bituminous mixtures — Material specifications Part 5 : Stone Mastic Asphalt, BSI Br. Stand. (2016).
[22] BS EN 12697-44-2010–[2021-10-25–06-49-03 PM].pdf, (n.d.).
[23] AASHTO, Standard method of test for determining the fracture energy of asphalt mixtures using the semi-circular bend geometry (SCB), Des. TP105 − 13. (2013) 1–14.
[24] G. Volume Graphics, VGStudio MAX 3.0. Reference Manual, 2016.
[25] M.D. Abramoff, P.J. Magalhaes, S.J. Ram, Image processing with ImageJ. Biophotonics Int 11 (7) (2004) 36–42.
[26] M. Doube, M.M. Kłosowski, I. Arganda-Carreras, F.P. Cordelieres, R.P. Dougherty, J.S. Jackson, B. Schmid, J.R. Hutchinson, S.J. Shefelbine, BoneJ: free and extensible bone image analysis in ImageJ, Bone 47 (6) (2010) 1076–1079.
[27] H.J. Vogel, Morphological determination of pore connectivity as a function of pore size using serial sections, Eur. J. Soil Sci. 48 (1997) 365–377.
[28] H.-J. Vogel, K. Roth, Quantitative morphology and network representation of soil pore structure, Adv. Water Resour. 24 (3-4) (2001) 233–242.
[29] M. Aboufoul, A. Garcia, Factors affecting hydraulic conductivity of asphalt mixture, Mater. Struct. Constr. 50 (2) (2017).
[30] Z. Zhang, Q. Liu, Q. Wu, H. Xu, P. Liu, M. Oeser, Damage evolution of asphalt mixture under freeze-thaw cyclic loading from a mechanical perspective, Int. J. Fatigue. 142 (2021) 1–9.
[31] D. Feng, J. Yi, D. Wang, L. Chen, Impact of salt and freeze-thaw cycles on performance of asphalt mixtures in coastal frozen region of China, Cold Reg. Sci. Technol. 62 (1) (2010) 34–41.
[32] G. Xu, Y. Yu, D. Cai, G. Xie, X. Chen, J. Yang, Multi-scale damage characterisation of asphalt mixture subject to freeze-thaw cycles, Constr. Build. Mater. 240 (2020), 117947.
[33] H.M. El Hussein, A.O.A. El Halim, Differential thermal expansion and contraction: a mechanistic approach to adhesion in asphalt concrete, Can. J. Civ. Eng. 20 (1993) 366–373.
[34] D. Jung, T.S. Vinson, Thermal stress restrained specimen test to evaluate low-temperature cracking of asphalt-aggregate mixtures, Transp. Res. Rec. 12–20 (1993).

Chapter 6

Peridynamic modelling and simulation of asphalt at low and high temperature

In this Chapter experiments on asphalt mixture with three different void content has been carried out at low and high temperature to assess the mechanical and fracture properties and correlated with the internal structure such as void and aggregate. Further investigation has been carried out using X-ray CT scan to obtain the topologies. The computational studies have been used to compare with the experiments.

This chapter has been submitted to Journal of *Construction and Building Materials*

My contributions in this work were: Conceptualisation, Designed the work and performed the simulations, Methodology, Validation, Writing the original draft, Reviewing and Editing.

I would like to thank all the authors who have contributed to this work.

Abstract

Asphalt mixture undergoes damage caused by loading and environmental conditions. Understanding the degradation mechanisms may help design novel types of asphalt mixture. Experimental tests, X-Ray CT scans and computational analysis can provide a complete assessment of the asphalt mixture's mechanical properties and fracture characteristics. In this study, the effect of temperature, aggregate, and void characteristics on the mechanical properties and fracture resistance are investigated, both experimentally and computationally. Three types of asphalt mixture are manufactured and x-rayed to acquire the internal structure of voids and aggregates. Asphalt mixture mechanical properties are determined and correlated with aggregate, void and properties. Asphalt mixture has lower mechanical and fracture properties with higher void content (more than 14%) and larger aggregate (20 mm). Irregular pores are detrimental to the asphalt mixture properties. CT scans were used to digitalize the asphalts mixture samples before they were simulated with the peridynamics model. The model reproduces the asphalt mixture characteristic at both low and high temperatures with 23.06% and 6.9% errors respectively.

6.1 Introduction

Asphalt mixture is one of the most utilized pavement materials. As a heterogeneous composite material, composed of aggregates, bitumen, and mineral filler, the properties of asphalt mixture is dependent on its component's mechanical/physical properties (such as aggregate and binder composition, gradation, distribution and orientation) and void ratio in addition to the environmental factors such as high temperatures or freeze-thaw actions [2], [3]. The cycling and environmental conditions cause the deterioration of asphalt mixture; hence reducing its lifespan and increasing maintenance costs [5], [6]. Understanding these degradation mechanisms is, therefore, important for better design and maintenance of this widely used material.

Asphalt mixture properties are influenced by the temperature which directly influences the asphalt mixture properties and lifetime. Asphalt mixture 's performance and softness changed as the temperature changed, and temperature sensitivity is an influential index for estimating asphalt mixture properties. Asphalt mixture is a viscoelastic material that becomes brittle at low temperatures [4]. At high temperatures, the typical asphalt mixture damage is rutting caused by the low stiffness of bitumen [168] and a poor asphalt mixture composition [169]. At low temperatures, water permeation may lead to crack formation which may cause ravelling and the premature failure of the pavement [172].

Many researchers using semi-circular bending tests (SCB) have investigated the effect of mechanical properties of aggregate gradation, the topology of voids and temperature on the properties of asphalt mixture [6], [12], [13].

SCB test is the most popular to assess the mechanical properties of asphalt mixture such as the tensile strength and the fracture energy [15]. Moreover, this test is also used to determine the cracking resistance using the fracture toughness [14]. However, the SCB test alone is insufficient to determine the asphalt mixture's properties because the asphalt mixture's internal structure plays a key role in

asphalt mixture performance. Hence, X-ray CT scans provide information on void content and the topologies of voids [172]. This technology allows for characterising and quantifying voids percentage, tortuosity, void circularity, roundness [172], and aggregates' topology [8].

Despite several efforts to investigate the fracture characteristics of asphalt mixture using X-ray CT scans, these cannot illustrate the evolution of the damage within asphalt mixture which is crucial for understanding the deterioration mechanisms. As a result, a numerical method could give a tool for understanding the mechanics of asphalt mixture degradation.

Numerical approaches have clear advantages compared to experimental tests providing a more flexible and cost-effective approach to researching asphalt mixture behaviour, and numerous studies have used numerical simulations of SCB tests. For example, Sun et al. [19] used experiments and the discrete element method to study the impact of porosity on fracture properties at low temperatures. Xue et al [20] used the discrete element method in a 2D model to simulate the fracture behaviour of asphalt concrete at low temperature. However, the model did not consider void and in 2D the crack development is not close to the 3D.

Successful numerical models and techniques have been used to explore the mechanical behaviour of asphalt mixture in recent years, including the finite element method (FEM) [21] and the lattice spring model (LSM) [20]. Three-dimensional dynamic fracture and multi-crack propagation are still difficult to represent, for example, with FEM which is based on continuum mechanics and has limitations when singularities appear [25], XFEM address that limitation by reducing the remeshing in cracking analysis but for the heterogeneous material is still limited due the facial boundaries need more adjustment [173]. Novel mesh-free methods may exhibit excellent results to simulate crack propagation without mesh regeneration. The Lattice spring model (LSM) is one of the first mesh-free methods, representing the material as computational particles and the mechanical properties with springs that connect the particles [174]. Moreover, Peridynamic (PD) [175] is a novel mesh-free

method that belongs to the same category of LSM based on discretising the material using spatial integral equations rather than partial differential equations. Unlike the FEM, Peridynamic can model discontinuities, including stationary, and unlike the lattice spring model, it can be used for dynamic fracture and crack propagation in brittle materials [8], [176]. The model is discussed in the next paragraph. The application of Peridynamic to simulate the mechanical properties and damage in construction materials is highly innovative.

The results present in the literature, e.g. [2], [12], [13], are experimentally based and ignore the influence of the single component of the mixture. Researchers [127], [130], [172] have investigated asphalt mixture at a smaller scale with the CT scan providing topologies information of the asphalt mixture under different loading and environmental effect. Despite these efforts, the CT scans results are not correlated with the mechanical results and in addition, both the experiment and CT scan hardly provide the evolution of the damage under these detrimental effects. The numerical studies provide the information necessary for understanding the evolution of asphalt mixture performance under different solicitations, but to the best of our knowledge, the methods used to numerically study asphalt mixture are not very accurate like the damage phenomenon. For instance, in [151] the fracture behaviour of asphalt mixture was investigated using XFEM, to overcome the re-meshing limitation. Despite the model corrections, the crack propagates through aggregate or follows a straight line [144] which is not observed in the experiment. In general, researchers seek to improve the anti-crack performance of asphalt mixtures from the standpoint of material properties, such as filler and additives, rather than focusing on optimizing aggregate gradation and composition.

However, experimental studies are expensive because they require many time-consuming tests. Hence, combining experiments with computational studies based on peridynamic may cut the cost of developing more resistant materials. This study provides a tool for optimising asphalt mixtures and predicting mechanical and fracture properties using computational methods.

Hence, this experimental and computational investigation aims to understand the effects of internal structure and temperature on the asphalt mixture's mechanical properties and its fracture resistance. To achieve this goal, we quantified asphalt mixture and mastic's mechanical and fracture properties at various temperatures. Asphalt mixtures samples were scanned to acquire the aggregate and void characteristics to compare them to asphalt mixture's mechanical and fracture properties. Furthermore, the results of the computational analysis using the realistic digital samples were compared with the experimental results to understand the mechanism and the impact of the internal structure on fracture performance and provide information for a better design of asphalt mixture under different temperature conditions.

6.2 Theory

6.2.1 Peridynamics

The material body is represented as a lattice in the Peridynamic theory. The nodes of the lattice interact with other nodes in the neighbourhood, known as horizons which behave through a constitutive equation that relates deformation and force, contrary to traditional continuum mechanics which relates strain and stress. Peridynamic modelling can be generally based on a bond-based or a state-based approach. In the Bond-based Peridynamic [175], the particle forces are solely dependent on the bond between them and thus the results are constrained to a Poisson ratio of 1/4 3D (or 1/3 in 2D). In states-based Peridynamic [177] the connection between bonded elements depends on a matrix of particle states. State-based Peridynamic is more complex, but it is not limited to a constant Poisson ratio. In the state-based Peridynamic, the materials are modelled as elastic using the state-based peridynamic linearly elastic models (LPS) [177], viscoelastic using visco-elastic peridynamic solid models (VES) [178] and elastoplastic using elastoplastic peridynamic solid models (EPS) [179]. Here

we use the LPS and VES model which belong to the State-based peridynamic. In addition, VES is a special case of LPS which can model both elastic and viscous material.

The fundamental Peridynamic equation of motion are given by [177]

$$\rho(x)\ddot{u}(x,t) = \int_{H_x} \{\underline{T}\,(x,t)\langle x' - x\rangle - \underline{T}(x',t)\langle x - x'\rangle\} dV' + b(x,t) \tag{63}$$

where $\rho(x)$ is the mass density of the material at the reference position x, ü is the acceleration of the material point x, H_x is a neighbourhood of x comprising all material points x' inside the horizon δ, b is the density field of a body force, and dV' is the infinitesimal volume. The $\underline{T}$ is the force vector state field at time t, acting to the bond $\langle x' - x\rangle$ within the horizon and with the dimension of the force vector per unit volume squared, is defined as

$$\underline{T}(x,t)\langle x' - x\rangle = \underline{f}\langle x' - x\rangle \frac{\varepsilon + \eta}{\|\varepsilon + \eta\|} \tag{64}$$

where f is the force state's scalar component known as the force modulus state, ε is the vector state; that is the relative position between the two particles in the reference configuration defined as

$$\underline{X}\,\langle x' - x\rangle = x' - x\ = \varepsilon \tag{65}$$

In a non-deformed body, $B_0, \underline{X}$ is the reference state mapping all bonds. Associating with the bond, $\underline{U}$ is the relative displacement vector state provided by

$$\underline{U}\langle x' - x\rangle = u(x', t) - u(x, t) = \eta \tag{66}$$

Figure 28 shows the deformation state $\underline{Y}$ which maps all bonds into its deformed image, B distorted picture, and given by

$$\underline{Y} = \underline{X} + \underline{U} = y' - y = \varepsilon + \eta \tag{67}$$

Where y and y' are the new position of the particles x and x'.

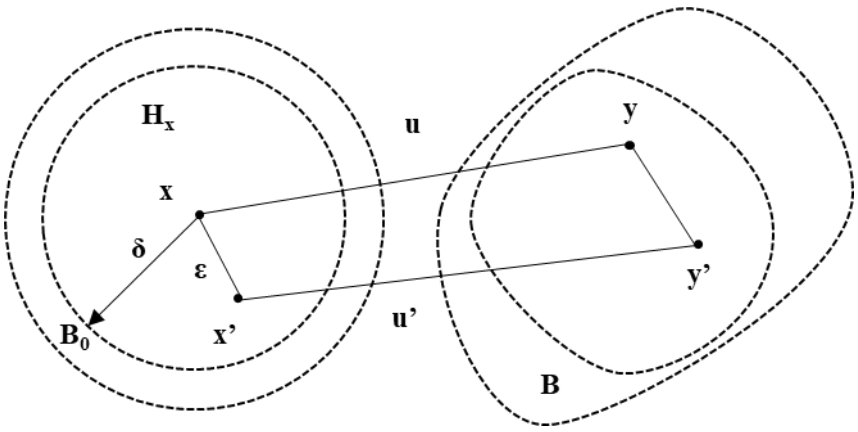

Figure 28: Graphical illustration of the deformation of body B_0 **and the relative modification of the bond** ε **represented in (3).**

The force scalar state for the linear elastic model is given by [177]-[179]

$$\underline{t} = \underline{t^i} + \underline{t^d} = \frac{3k\theta}{m}\underline{\omega}\,\underline{x} + a\,\underline{\omega}\,\underline{e^d} \tag{68}$$

where $\underline{t^i}$ and $\underline{t^d}$ are respectively the scalar volumetric and deviatoric state, k is the bulk modulus, the $\underline{\omega}$ is the influence function also named the scalar weighting function that measures the influence of the bonds involved in the force state calculation, whose argument is the bond vector ε in the reference configuration [177].

The weighted volume is given by

$$m = (\underline{\omega}\ \underline{x}) \cdot \underline{x} \tag{69}$$

The dilatation volume which is a scalar state, of the neighbourhood H_x defined as follow

$$\theta = \frac{3}{m}(\underline{\omega}\ \underline{x})\underline{e} \tag{70}$$

The extension $\underline{e}$ which is a scalar state, is given by

$$\underline{e} = \|\underline{Y}\| - \|\underline{X}\| \tag{71}$$

Also defined as

$$\underline{e} = \underline{e}^i - \underline{e}^d \tag{72}$$

$\underline{e}^i$ is defined as spherical extension state and given by

$$\underline{e}^{i} = \frac{\theta \|X\|}{3} \tag{73}$$

The reference position scalar state is given by

$$\underline{x}\langle\varepsilon\rangle = \|\varepsilon\| \tag{74}$$

The scalar deviator state component $\underline{e^{d}}$ is defined as

$$\underline{e^{d}} = \underline{e} - \frac{\theta \|X\|}{3} \tag{75}$$

and a is related to the shear modulus G as

$$a = \frac{15\ G}{m} \tag{76}$$

The viscoelastic model, as an extension of the LPS model, adds a decomposition of the scalar extension state $\underline{e}$. The model applies the viscoelasticity to the deviatoric part of the scalar extension state $\underline{e}$ remaining associated with the elastic theory.

The viscoelastic peridynamic model (VES) [178] describes the material as a standard linear solid, schematized in Figure 22.

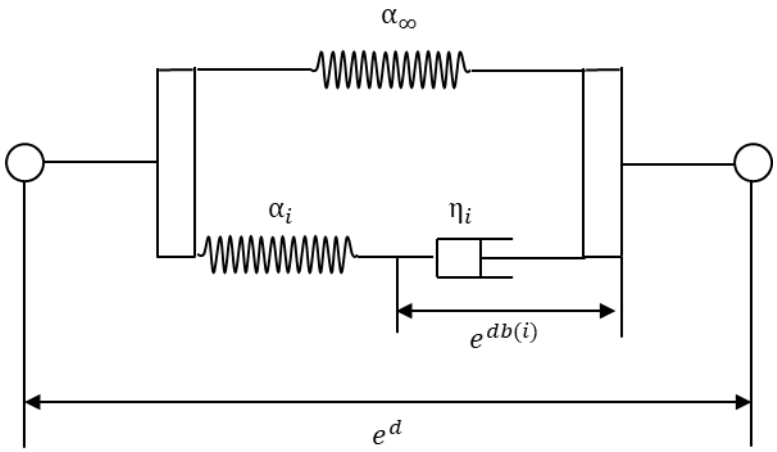

Figure 29 Standard linear solid model for viscoelastic peridynamic solid models.

The scalar extension state $\underline{e}$ is divided into spherical and deviatoric parts. The spherical part represents the isotropic expansion and the deviatoric part the shear deformation [178]. The deviatoric is made of elastic $\underline{e^{de}}$ and back extension $\underline{e^{db(i)}}$ parts

$$\underline{e^d} = e^{de} + e^{db(i)} \tag{77}$$

According to the last equation, the scalar force state $\underline{t}$ is given by

$$\underline{t} = \underline{t^i} + \underline{t^d} = \frac{3k\theta}{m}\underline{\omega}\,\underline{x} + (a_\infty + a_0)\underline{e^d} - a_i\underline{\omega e^{db(i)}}) \tag{78}$$

The elastic parameter a is described as follows

$$a = a_\infty + a_i \tag{79}$$

a_∞ is the elastic part and a_i is the relaxation moduli.

Normalising the relaxation moduli a_i as

$$a_i = a\,\lambda_i \tag{80}$$

Substituting (80) in (79) the elastic a_∞ is

$$a_\infty = a(1-\lambda_i) \tag{81}$$

where λ_i ranges between 0 and 1. When λ_i is close to 0, the model is elastic, and when it is close to 1 viscoelastic [178].

The evolution equation of the scalar deviatoric force back extensions' dashpot is given by [178]

$$\underline{t^d}(t) = \underline{e_0^d}(a_\infty + a_i e^{\frac{-t}{\tau_i^b}}) \tag{82}$$

where τ_i^b is a time constant.

To describe fracture, the concept of bond failure is introduced in proportion to the strain of the bond, as defined by

$$s = \frac{\left\|\underline{Y}\langle x'-x\rangle\right\| - \left\|\underline{X}\langle x'-x\rangle\right\|}{\left\|\underline{X}\langle x'-x\rangle\right\|} = \frac{\|\eta+\varepsilon\| - \|\varepsilon\|}{\|\varepsilon\|} \tag{83}$$

When s exceeds a crucial value s_0, the bond is broken and consequently not part of the body after that. The critical constant value s_{00} is defined as [153]

$$s_{00} = \sqrt{\frac{5\pi\, G}{9\, K\, \delta}} \tag{84}$$

The critical value s_0 is not constant depending on the overall state and adjusts dependent on its damage which is described as

$$\varphi(\boldsymbol{x}, t) = \frac{1 - \int_{H_x} \mu(\boldsymbol{x}, t, \varepsilon) dV_\varepsilon}{\int_{H_x} dV_\varepsilon} \tag{85}$$

where μ is a value of 0 or 1 and history dependent damage function, i.e.

$$\mu(t, \varepsilon) = \begin{cases} 1 \; if \; s(t', \varepsilon) < s_0 \;\; \forall\, 0 \leq t' \leq t \\ 0 \qquad\qquad\qquad otherwise \end{cases} \tag{86}$$

For materials like mastic, it is a simplification an independent s_0 from other conditions, like compressions, therefore the damage criterion is better modelled if the value is variable as follow

$$s_0(t) = s_{00} - \alpha s_{min}(t) \tag{87}$$

For a given material point, s_{00} is a constant and s_{min} is the current stretch minimum among all bonds attached to it [153]

$$\mathrm{s_{min}(t)} = \min \left\{ \frac{\left\| \underline{\mathrm{Y}}\langle \mathrm{x}' - \mathrm{x} \rangle \right\|(\mathrm{t}) - \left\| \underline{\mathrm{X}}\langle \mathrm{x}' - \mathrm{x} \rangle \right\|}{\left\| \underline{\mathrm{X}}\langle \mathrm{x}' - \mathrm{x} \rangle \right\|} \right\} = \frac{\|\eta + \varepsilon\|(\mathrm{t}) - \|\varepsilon\|}{\|\varepsilon\|} \tag{88}$$

6.3 Methodology

6.3.1 Asphalt mixture and Mastic preparation

Three different asphalt mix varieties are manufactured according to BS EN 12697-33 [180] and BS EN 12697-35 [181]. All mixes are made with crushed granite aggregates up to 20 mm in size and 60/40 pen bitumen, blended at 165 °C and roller compacted at 165 °C. Table 1 provides the aggregate gradation and binder content of asphalt mixtures.

Table 1. Asphalt mixture composition

Size (mm)	Target void content, %		
	3%	9.8%	14%
20	0	23.6	0
14	0	42.4	0
10	58.9	0	63.5
6.3	7.5	9.4	18.9
Dust	18.7	12.3	7.6
Filler	8.4	6.6	4.7
Bitumen	6.5	5.7	5.5
Air void content	3	9.8	14

The bulk densities of the asphalt mixtures are calculated following BS EN 12697, part 5 [180] and part 6 [180]. Ten asphalt mixture slabs of 300 mm x 300 mm x 60 mm are manufactured with 3%, 9.8%, and 14% air voids and calculated using the equation (89) according to [180].

$$V_s = \frac{\rho_m - \rho_b}{\rho_m} \tag{89}$$

where the asphalt mixture's void is V_s, %, the asphalt mixture maximum density is ρ_m, kg/m^3, and ρ_b is the bulk density of asphalt mixture, kg/m^3.

Cylindrical cores 100 mm in diameter and 60 mm in height are extracted from the slabs using a core saw. The cylinders are trimmed for around 10 mm on the top and the bottom of the cores. Five cores per slab are removed, totalling 50 cores of 100 mm diameter and 40 mm height. Cutting each core along its diameter lead to two semi-circular specimens which are used to investigate their fracture properties. To examine fracture properties, a vertical notch is inserted along the symmetrical axis with 10 mm ± 1 mm of length and thickness of 4 ± 0.5 mm.

Three mastics corresponding to these in the asphalt mixtures in Table 1 are manufactured. The mastics are a mixture of bitumen and aggregates with an average diameter smaller than 2.36 mm [182]. The dust is sieved to 2.36 mm and mixed with filler and bitumen in the same percentages shown in Table 1.

Bitumen and aggregates are mixed manually with a spatula at 165 °C and poured into a mould to produce beams with a dimension of 3 cm x 3 cm x 10 cm, see Figure 30. The mould had a triangular notch to induce a predetermined breaking point. Once the mastic cooled down to 20 °C, it is removed from the mould and stored at constant temperatures, of -10 °C and 20 °C.

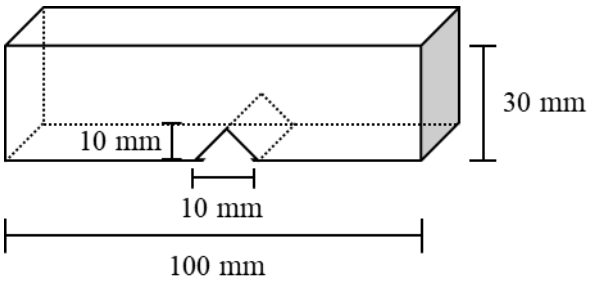

Figure 30: Mastic specification

6.3.2 3-point bending test

The 3-point bending test is used to characterise asphalt mixtures and mastics at -10 °C and 20 °C following to BS EN 12697-44 [183].

In this study, semi-circular specimens and mastic beam are conducted under the three-point bending load configuration. The sample is placed on two rollers, at the distance of 80 mm between them see Figure 1.

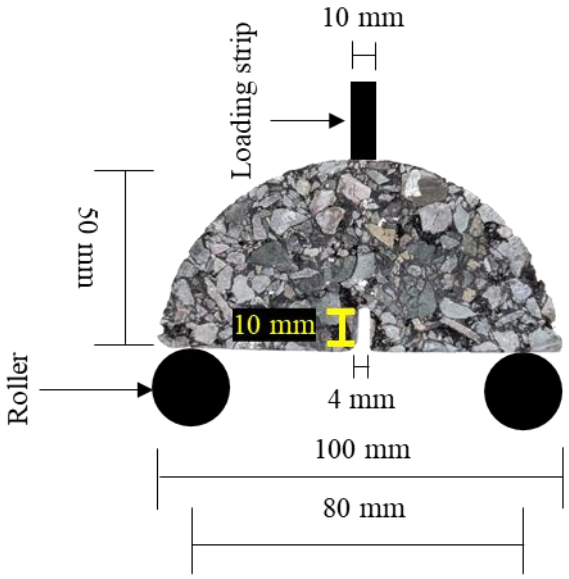

Figure 31: Semi-circular bending test

Until the material failed, the load is applied at a steady rate of 5 mm/min. The load and specimen deformation are both reported. The specimen's peak load is also calculated.

The maximum stress at failure [183], σ_m, is obtained with the equation

$$\sigma_m = \frac{4.263\ x\ F}{D\ x\ h} \tag{90}$$

Where D is the diameter, m, h is sample thickness, m, and F is the peak load, N.

The material's resistance to fracture is calculated using the fracture toughness, K_i, as shown in [183]

$$K_i = \sigma_m \, x \, f(\frac{a_i}{W_i}) \tag{91}$$

where W_i is the height of the specimen, a_i is the notch depth, and $f(\frac{a_i}{W_i})$ the geometric factor. The geometric factor $f(\frac{a_i}{W_i})$ is 5.956, for $9 < a_i < 11$ mm and $70 < W_i < 75$ mm. For other a_i and W_i values, the geometric value can be calculated according to the formula [183]

$$f\left(\frac{a_i}{W_i}\right) = -4.9965 + 155.58\left(\frac{a_i}{W_i}\right) - 799.94\left(\frac{a_i}{W_i}\right)^2 + 2141.9\left(\frac{a_i}{W_i}\right)^3 - 2709.1\left(\frac{a_i}{W_i}\right)^4 + 1398.6\left(\frac{a_i}{W_i}\right)^5 \tag{92}$$

The fracture energy is the area below the load-displacement curve until the specimen is broken [183] and describes the energy released during cracking

$$G_f = \frac{W}{A_{lig}} \tag{93}$$

Where W is the fracture's work and A_{lig} the ligament area, defined as

$$A_{lig} = (r - a)\, x\, h \tag{94}$$

Where r is the specimen radius, m, a is the notch length, m, and h specimen thickness, in m.

In this study, the fracture performance of asphalt mixture is calculated through its fracture toughness. The Young modulus and fracture energy of mastics are used as inputs for the numerical model of the asphalt mix.

The coefficient of variation (COV) is the ratio of the standard deviation to the mean of the experimental value [170]. COV is calculated using equation (95)

$$COV = \frac{Standard\ deviation}{mean} \tag{95}$$

6.3.3 Images acquisition and creation of digital materials

A Phoenix v|tome|x L 300 micro-CT scanner is used to scan the asphalt mixture's CT scans. The device contains an X-ray tube (MXR320HP/11, 3.0 mm Be + 2 mmAl from GE Sensing and Inspection Technology) that generates 290 kV of acceleration voltage and 1300 mA of current [8],[172].

The specimens are mounted on a rotatable table and positioned 906.84 mm from the X-ray source. The scans are recreated using the GE Datos|x reconstruction programme at 2x resolution. The results have a spatial resolution of 45.2 mm and isotropic, therefore the slice thickness is also 45.2 mm.

Voxel values represent the attenuation of x-rays, and the images are generated in 16-bit format (.tiff). VG Studio Max [166] and ImageJ, Version 1.8.0 [184], are used to analyse the images and convert them to grayscale in 8-bit.

ImageJ is used to distinguish the different parts of the samples, such as aggregates, air voids, and mastic applying the grayscale thresholding to segment the materials. Minor isolated clusters of less than 0.5 mm are deleted from the image as small voids, aggregates, or noise. The segmented photos of the air spaces and aggregate are stacked in VGSTUDIO MAX to create 3D surfaces. ImageJ is used to calculate the void and aggregate topologies obtaining the mean diameter, mean area, aspect ratio and circularity.

Using Fiji's Particle Analyser plugin [184] (Version 1.4.3), the equation (96) calculates the mean diameter, D_{mean}, using the thickness algorithm

$$D_{mean} = \frac{\sum_{i=1}^{n} d_i V_i}{\sum_{i=1}^{n} V_i} \tag{96}$$

where, d_i is the diameter of single void or aggregate and, V_i is the volume of each pore or aggregate in the sample. The mean area is calculated using the BoneJ surface area [184] plugin (Version 1.4.3) by converting pores or aggregate into triangular meshes and calculating the total surface area and volume of pores or aggregate

$$Mean\ area = \frac{A}{V} \tag{97}$$

Where A is the total surface of voids or aggregates and V the specimen's volume.

The digital volume of voids and aggregates (e.g. air void content) is calculated as the $average\ mean\ area$ of all images divided by the number of images

$$Mean\ volume = \frac{average\ mean\ area}{number\ of\ images} \tag{98}$$

The aspect ratio is defined as the ratio between the biggest and smallest orthogonal diameter of the void or aggregate. Particle Analyser plugin [184] (Version 1.4.3) in Fiji calculates the aspect ratio's value (A_r) using the equation (100) utilising the shape descriptors algorithm as

$$A_r = \frac{d_{max}}{d_{min}} \tag{99}$$

Where d_{max} and d_{min} respectively are the largest and smallest orthogonal axis.

Particle Analyser plugin [184] (Version 1.4.3) in Fiji calculates the circularity ($Circ$) using the equation (100) utilising the shape descriptors algorithm as

$$Circ = \frac{4\pi A}{P^2} \tag{100}$$

Where A and P are respectively the area and the perimeter. The perfect circle void or aggregate has a value of 1, and the elongated void or aggregate has 0 value.

A square lattice with side l=0.00067 m is imposed on the image stacks of asphalt mixtures using MATLAB. The lattice distance was chosen accordingly with a previous study [8] where the validation of the model was assessed. A peridynamic particle corresponds to a lattice node, see Figure 32. Since

different asphalt mixtures had a range of void and aggregate contents, they also had different particle numbers.

The numbers of particles for the mortar are 272,237, 186,503 and 221,665 for asphalt mixtures with 3%, 10% and 14% voids content, respectively. The numbers of particles for the aggregates are 191,151, 246,681 and 198,719 for asphalt mixtures with 3%, 10% and 14% voids content, respectively.

To evaluate the reliability of the simulation, we calculated the errors [185] between the result of the simulation and the physical test using equation (101).

$$Error = \left|\frac{Result_{sim} - Result_{lab}}{Result_{lab}}\right| x\ 100\% \quad (101)$$

Where $Result_{sim}$ and $Result_{lab}$ are the value of the simulation and experiment respectively.

The relative error between the air voids content of the asphalt mixture samples and digital asphalt mixture is calculated with equation (101) to evaluate the accuracy of the model generation's methods. The relative errors in the air void content in digital asphalt mixture are for the 3%, 10% and 14% asphalt mixtures 1.3%, 3.3% and 0.3% respectively. The error is attributable to the inevitable loss of information on the sample's surface during the X-ray process [131]. The result indicates an accurate reproduction of the real asphalt mixture structure.

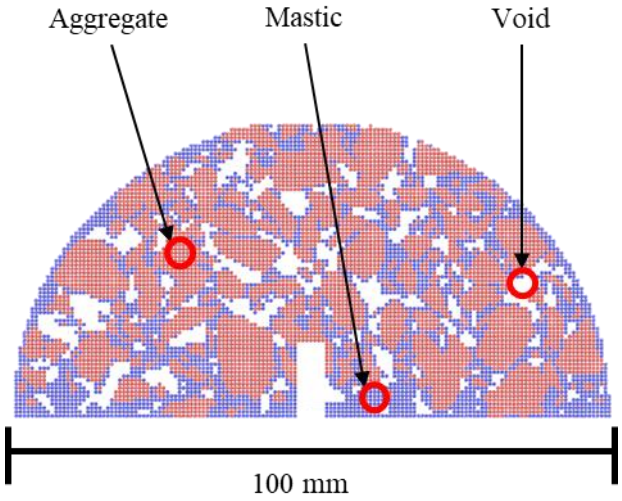

Figure 32: Asphalt mixture digital sample

6.3.4 Software used for the simulations

The simulations are carried out in LAMMPS [186] with the Peridynamic package [187] which is a free open-source software for material modelling at a range scale from atomic to mesoscale to continuum with the advantages to interact with different models [8]. The simulation output is visualised with OVITO [188] which is a free software for atomic visualisation and analysis.

6.3.5 Material properties for the simulations

The intrinsic properties of aggregates are the same for all simulations. The mastic and the mastic-aggregate proprieties depended on the mastic mixture and the temperature. This chapter has investigated three temperatures: -10 ℃ and 20 ℃. Mortar is elastic and brittle at -10 ℃, and viscoelastic at 20 ℃. The aggregate is considered elastic at all temperatures. We used the linear elastic Peridynamic model (LPS), for brittle materials and the viscoelastic Peridynamic model, VES, for viscoelastic materials. The viscoelastic material in VES is modelled using the standard linear solid model.

In Table 2, the mechanical properties of the mastic, aggregate and interface simulations are listed. These have been obtained from a previous study for -10℃ [172]. For 20℃, they are obtained from 3-point bending tests.

The mechanical properties of aggregate are obtained from reference [189], and for the interface, we assumed the Young modulus is the same as the mastic, and the fracture energy G_0 at the interface is determined from reference [190]. The literature emphasises the difficulty in obtaining the fracture energy at -10 °C, and the results obtained are highly varied. As a result, the author chose the value that best matched the results.

Table 2. mechanical properties of mastic, aggregate and interface used in the simulation.

		E [Pa]	**υ [-]**	**ρ [Kg/m^3]**	**G_0 [J/m^2]**
Asphalt mixture 3% void (-10℃)	**Mastic**	1.9 x 10^8	0.25	2200	255
	Aggregate	1.4 x 10^{10}	0.15	2500	1250
	Interface	1.9 x 10^8	0.25	-	5
Asphalt mixture 10% void (-10℃)	**Mastic**	1.41 x 10^8	0.25	2200	207
	Aggregate	1.4 x 10^{10}	0.15	2500	1250
	Interface	1.41 x 10^8	0.25	-	5
Asphalt mixture 14% void (-10℃)	**Mastic**	4.37 x 10^7	0.25	2200	235
	Aggregate	1.4 x 10^{10}	0.15	2500	1250
	Interface	4.37 x 10^7	0.25	-	5
Asphalt mixture 3% void (20℃)	**Mastic**	7.9 x 10^5	0.25	2200	523
	Aggregate	1.4 x 10^{10}	0.15	2500	1250

	Interface	7.9×10^5	0.25	-	637
Asphalt mixture 10% void (20°C)	**Mastic**	5.8×10^5	0.25	2200	611
	Aggregate	1.4×10^{10}	0.15	2500	1250
	Interface	5.8×10^5	0.25	-	637
Asphalt mixture 14% void (20°C)	**Mastic**	2.9×10^5	0.25	2200	312
	Aggregate	1.4×10^{10}	0.15	2500	1250
	Interface	2.9×10^5	0.25	-	637

6.3.6 Description of the viscoelastic behaviour of asphalt mixture using a Prony series

Viscoelasticity is a time-dependent property of materials that exhibit both elastic and viscous behaviour when deformed, such as the mastic. It can be described with a creep test which consists of a sudden strain applied to the body which is kept constant over time to measure the relaxation of stress. The elastic part is the initial tension, while the viscous part represents the stress relaxation over time.

The resulting stress against time is modelled with a Prony series [191] as follows

$$E(t) = E_\infty + \sum_{1}^{n} E_0 exp\left(\frac{-t}{\tau_i}\right) \quad (102)$$

Where the equilibrium modulus is E_∞ when the material stress is totally lowered and it happens at time t infinite, the relaxation modulus is E_0, τ_i is the relaxation time.

The τ_i required for the VES is obtained with the Prony series [178], see Table 3. The τ_i is obtained fitting the standard nonlinear solid model curve using the minimisation solver between predicted with experimental one.

Table 3. Prony series for the mastic [192].

Item	t (s)	E_m (MPa)
1	6.20×10^{-2}	26.99
2	1.35×10^{-1}	20.13
3	2.91×10^{-1}	13.85
4	6.28×10^{-1}	8.72
5	1.35×10^{0}	5.04
6	2.92×10^{0}	2.76
7	6.28×10^{0}	1.44
8	1.35×10^{1}	0.73
9	2.91×10^{1}	0.37
10	6.28×10^{1}	0.18

The parameters of the Prony series are in Table 3 and obtained from reference [192].

6.3.7 Peridynamic parameters used for the simulations and virtual experiment

Table 4 shows the peridynamic parameters of the aggregate and mastic used for the simulations.

The value of λ describes the viscoelasticity degree of material and is between 0 and 1. The value of λ closes to 0 describe a material as elastic and close to 1 as viscoelastic. For instance, the aggregate value assigned for λ is 0.01 and for mortar and interface is 0.99.

Table 4. Peridynamic parameters used in the simulations

		S_{00} [-]	α [-]	N	τ	λ
Asphalt mixture 3% void (-10°C)	**Mastic**	0.02366	0.25	272,237	---	---
	Aggregate	0.00721	0.15	191,151	---	---
	Interface	0.00054	0.25	---	---	---
Asphalt mixture 10% void (-10°C)	**Mastic**	0.02475	0.25	186,503	---	---
	Aggregate	0.00721	0.15	246,681	---	---
	Interface	0.00054	0.25	---	---	---
Asphalt mixture 14% void (-10°C)	**Mastic**	0.04736	0.25	221,665	---	---
	Aggregate	0.00721	0.15	198,719	---	---
	Interface	0.00054	0.25	---	---	---
Asphalt mixture 3% void (20°C)	**Mastic**	0.52520	0.25	272,237	0.0048	0.95
	Aggregate	0.00721	0.15	191,151	100	0.01
	Interface	0.00615	0.25	---	0.0048	0.95
Asphalt mixture 10% void (20°C)	**Mastic**	0.66253	0.25	186,503	0.0048	0.95
	Aggregate	0.00615	0.15	246,681	100	0.01
	Interface	0.00615	0.25	---	0.0048	0.95
Asphalt mixture 14% void (20°C)	**Mastic**	0.66953	0.25	221,665	0.0048	0.95
	Aggregate	0.00721	0.15	198,719	100	0.01
	Interface	0.00615	0.25	---	0.0048	0.95

The semi-circular bending test is replicated by placing the digital sample in a simulation box, laying on two cylindrical supports separated by 80 mm, simulating the experiment conditions.

The compression is supplied from the top of the virtual specimen at a regulated velocity along the vertical direction at 0.001 m/s, emulating the test metal piston (we verified that at 0.001 m/s, quasi-static conditions are attained.). The remaining directions are left available for expansion or contraction. All simulations used a time step of 10^{-8} s.

Each particle has the volume of a cube and a side length equal to the lattice distance, such as 0.00067 m. The resultant force is determined as the density force per particle volume, see Figure 33. The peridynamic force is determined using the total force per volume acting through the initial layer of particles in contact with the piston. The displacement is monitored from the upper layer of particles.

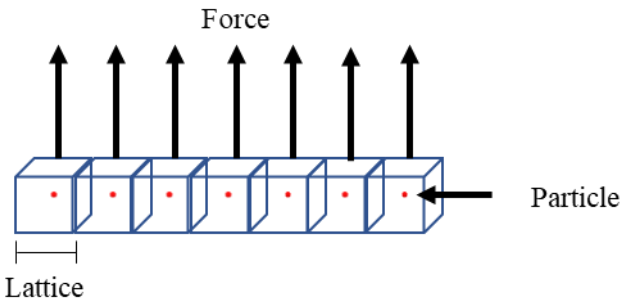

Figure 33: Peridynamic force representation in the particles.

6.4 Results and discussion

6.4.1 Mechanical and volumetric properties of asphalt mixture

The SCB test results of asphalt mixture with 3%, 10% and 14% air void content assessed at -10 °C, and 20 °C are shown in Figure 34. The results in this section will be used to validate the numerical simulations of asphalt mixture mechanical properties. The stress-strain curve for the sample at -10 °C indicates that the asphalt mixture behaviour is brittle, with an abrupt fracture at the peak force [4]. The crack began in the notch and spread straight across the sample [193]. The sample at 20 °C shows low stiffness with visco-elasticity behaviour before the peak; after, the peak load gradually decreases

[4]. The sample deformed permanently; however, this asphalt mixture had better fracture properties with slow crack propagation, indicating high relaxation and long post-break displacement [194].

The average values, standard deviations and coefficient of variation of peak load, ultimate strain, fracture toughness, and fracture energy of asphalt mixture at -10 °C and 20 °C are provided in Table 5. The peak load and ultimate strain are the maximum load and deformation of the sample before failure, respectively. The equivalent Young Modulus has been calculated as the slope of the linear section of the stress/strain curve. The values of the coefficient of variation are below 25% indicating that the repeatability condition for this test is satisfied [12], [170]. As can be expected from previous research, e.g. [195], asphalt mixture at higher temperatures has a lower peak load, Young modulus, fracture energy, fracture toughness, and higher ultimate strength than asphalt mixture at a lower temperature. In addition, the air voids content and aggregate skeleton affect the mechanical properties of asphalt mixture [196]. These variations are ascribed to the influence of internal structure which will be discussed using the simulations. Furthermore, as reported in other papers, e.g. [193], increasing the air void content reduces the asphalt mixture's peak load, young modulus, fracture toughness, and fracture energy. For example. at 20 °C, the asphalt mixture with 3% void content has the largest peak load, fracture energy, and fracture toughness, and its ultimate strain is lower than the asphalt mixture with 14% air void content [197], [198].

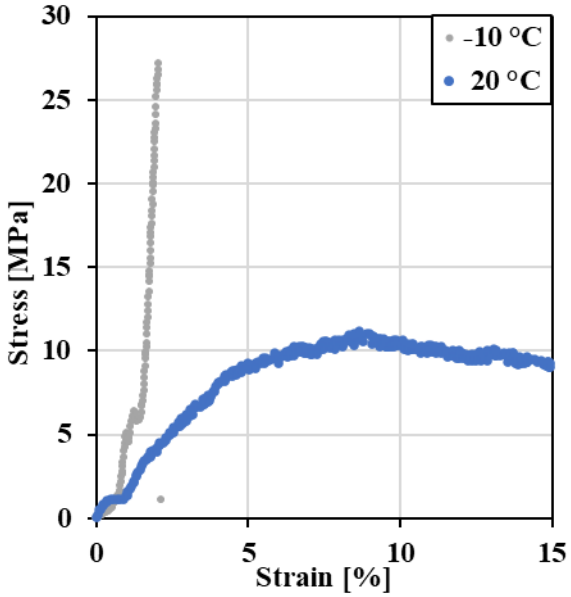

Figure 34: Example of semi-circular bending test results at different temperatures

Differences in asphalt mixture composition and testing temperature resulted in different asphalt mixture cracking behaviours [185],[199]. For example, at -10 °C in asphalt mixture with 3% air voids content, cracks propagated primarily through the interfaces between aggregate and mastic and occasionally broke aggregates to follow a straight line, as shown in Figure 35 (a). In addition, asphalt mixture with a 3% air void content has the lowest aggregate content. Furthermore, larger aggregates slowed crack propagation, deviating the cracks, see Figure 35 (b), a similar finding in [199]. Indeed, the asphalt mixture with 10% void, with the highest aggregate dimensions and aggregate content, has the highest ultimate strain and is less affected by temperature changes, while the asphalt mixture with 3% void and the smallest aggregate dimensions and content has a lower fracture characteristic, a longer crack path, and is the one most affected by temperature changes (see Table 5 and Table 6. Moreover, Figure 35 (c) shows asphalt mixture with 14% air void content, where aggregates had less structural support, the crack propagated along the edge of aggregates and tried to follow a straight line. Besides, the cracks at 20 °C occurred above the notch and over the test support for the asphalt mixtures with 10% air void content, see Figure 35 (d). Finally, the crack for the asphalt mixture with

14% air void content occurred above the notch only, see Figure 35 (e). The reason for this is that the pores provided space for rearrangement that prevented cracking.

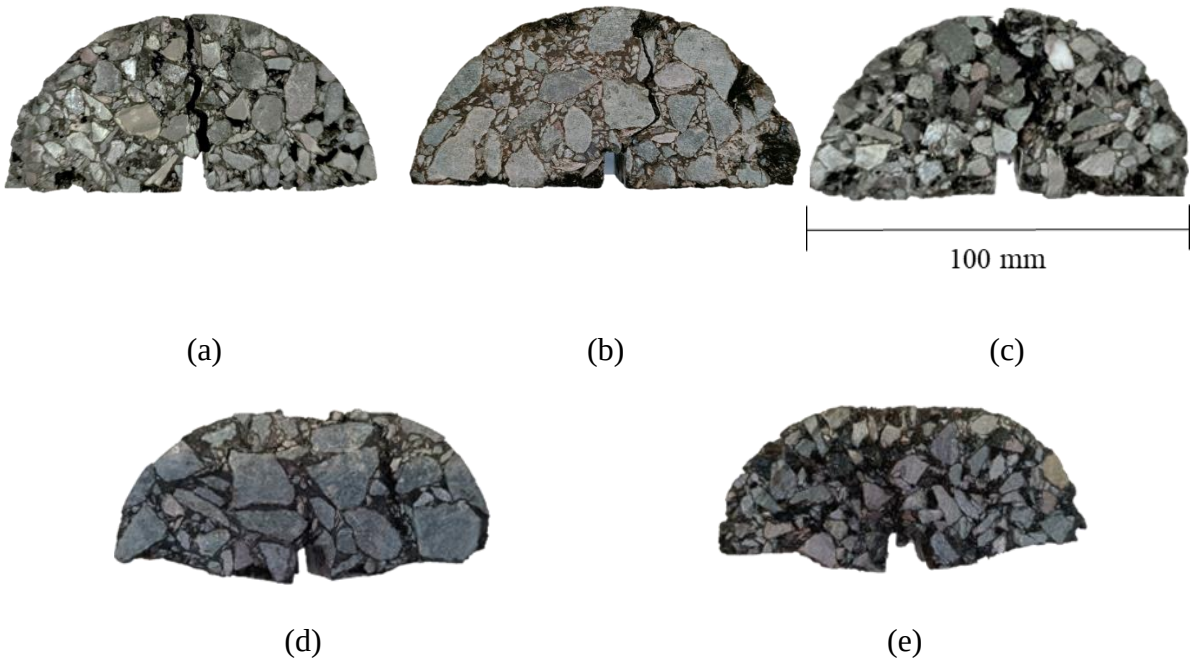

Figure 35: Crack paths after semi-circular bending test at, (a) asphalt mixture with 3% air void content at -10 °C, (b) asphalt mixture with 10% air void content at -10 °C, (c) asphalt mixture with 14% air void content at -10 °C, (d) asphalt mixture with 10% air void content at 14 °C (e) asphalt mixture with 14% air void content at 14 °C.

Table 5. Mechanical properties of asphalt mixtures

Sample (target voids content)	**Temperature (°C)**	**Peak load (kN)**	**Young Modulus (GPa)**	**Fracture energy (kPa m $^{0.5}$)**	**Fracture toughness (J/m^2)**	**Ultimate strain (%)**
3%	-10	5.5	3.8	841.0	48.1	1.3
10%	-10	4.1	2.9	921.0	35.6	2.0
14%	-10	2.2	1.4	699.0	19.1	1.0
3%	20	2.3	0.4	4200.0	20.0	2.9
10%	20	2.1	0.2	3652.3	18.0	6.4
14%	20	1.0	0.1	2825.0	9.0	16.1
Standard deviations						
Sample (target voids content)	Temperature (°C)	Peak load (kN)	Young Modulus (GPa)	Fracture energy (kPa m $^{0.5}$)	Fracture toughness (J/m^2)	Ultimate strain (%)
3%	-10	0.37	0.30	117	3.23	0.009
10%	-10	0.15	0.17	91	1.30	0.026
14%	-10	0.049	0.13	70	0.43	0.090
3%	20	0.23	0.03	114	2.03	0.400
10%	20	0.19	0.01	181	1.67	0.597
14%	20	0.15	0.01	247	1.30	0.624
Coefficient of variant						

Sample (target voids content)	Temperature (°C)	Peak load (kN)	Young Modulus (GPa)	Fracture energy (kPa m $^{0.5}$)	Fracture toughness (J/m^2)	Ultimate strain (%)
3%	-10	6.7	7.8	13.9	6.7	0.6
10%	-10	3.6	5.8	9.8	3.6	1.3
14%	-10	2.2	9.2	10.0	2.2	9.0
3%	20	10.0	7.5	2.7	10.1	13.8
10%	20	9.0	5.8	4.9	9.2	11.8
14%	20	15.0	5.6	8.7	14.4	3.7

Table 6. Topology of aggregate

Sample (target voids content)	**aggregate content (%)**	**Mean aggregate diameter (mm)**	**Mean aggregate area (cm^2)**	**Aggregate perimeter (mm)**
3%	58.507	3.999	7299.446	5.903
9.8%	60.111	11.959	9189.788	10.027
14%	51.634	7.754	7751.569	9.416

6.4.2 Validation of semi-circular bending test simulations at -10 °C with experimental results

To understand if Peridynamic can capture the mechanical and fracture properties of asphalt mixture at temperatures at -10 °C, semi-circular bending tests have been simulated, and the stress-strain curves

compared with experimental test results. The experimental and computational stress/strain curves for the asphalt mixture with 3% void, tested at -10 °C, are compared in Figure 36 as an example.

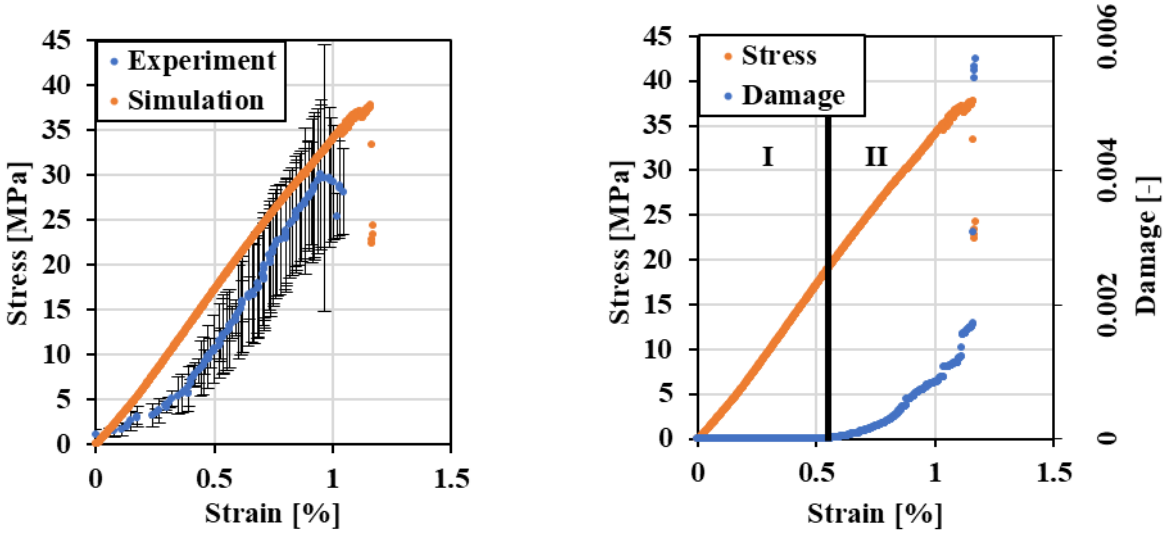

(a) (b)

Figure 36: (a) Experiment and computational results compared for asphalt mixture with 3% void at -10 °C. (b) Stress-strain curve and broken peridynamic bonds.

At -10 °C, see Figure 36 (a), the stress-strain curve follows a two stages failure process, as was previously explained in references [8], [200]. During the failure process from the stress-strain curve, two stages can be distinguished. In Stage I, there are no visible cracks; hence the stress-strain curve predicted by the simulation is linearly elastic, see Figure 36 (b). However, in the experiment, the piston contacts the asphalt mixture sample and applies an initial pressure, which accommodates the test sample. This causes that stress increases nonlinearly. In the simulation, the geometry is ideal, and no re-accommodation occurs. During Stage II, the local strain increases up to the critical stress value s_0. Then, the bonds start breaking, see Figure 36 (b), resulting in micro-cracks at the interfaces. With the increase of strain micro-cracks propagate. In this case, the stress simulated results in a higher value than in the experiment because of the ideal geometry and the model's incapability to reproduce

the nonlinearity in Stage I. The stress relative error in this study was 22.4% which is close to the error of 22.9% obtained in [171]. Furthermore, the young modulus of the digital asphalt mixture is 3.5 GPa for the 3% mixture, with a relative error compared to the experiment is 7%, indicating that the digital asphalt mixture has a similar mixture's proportion to the real sample at 3% void content. The results confirm that the simulation using the digital asphalt mixture is reliable reproduction of the asphalt mixture performance. Therefore, the accuracy of the simulation against the experiment was related to the consistency of the digital asphalt mixture's composition generation method. The solidity of the method is confirmed by the relative error of the young modulus, which led to mechanical properties with an error in line with other studies [171]. To the best of our knowledge, this study was the first to investigate asphalt mixture performances with Peridynamics. Hence, these results constitute a benchmark for further investigation.

In addition, Figure 37 shows the cracks, broken bonds and stress levels for the three types of asphalt mixture studied. All the simulations at -10 ℃ have in common the failure mode, where the crack propagates linearly from the notch and occasionally through the aggregates, as observed in the experiment in section 4.1. A similar case had been reported in reference [201], see Figure 37 (a) and (b). Furthermore, the asphalt mixtures at 3% and 10% void content have a higher bearing capacity compared to the asphalt mixtures with 14% air void content. For instance, the crack paths for the asphalt mixtures with 3% and 10% air void content are the longest ones, 27.9 cm and 19.6 cm respectively, versus the crack path for the asphalt mixture with 14% air void content, 11 cm, see Figure 37 (b).

The local stress has been monitored in Figure 37 (c) to assess the influence of the internal asphalt mixture's structure. The scale indicates compression for value closest to -3 MPa (blue) and tension for the value closest to 1 MPa. The stress analysis for the asphalt mixture at -10 ℃ indicates that except for the area under tension in the centre of the specimen, the aggregate skeleton is mainly under

compression stress which confirms that provides the bearing capacity of the asphalt mixture, and the mastic and the interface under the tension stress, see Figure 37 (c).

Furthermore, the stress occurs mainly in the middle of the specimen at the interfaces along with the loading direction predicting where damage will occur [202]. In addition, small, and sharp aggregates and voids have a higher concentration of stress as shown in Figure 37 (c). Song et al. [151] conducted in XFEM similar stress analysis on asphalt mixture using aggregate with defined shapes, such as circles, ellipse convex and concave shapes; the results indicate that the high-stress level around sharp areas may weaken the asphalt mixture

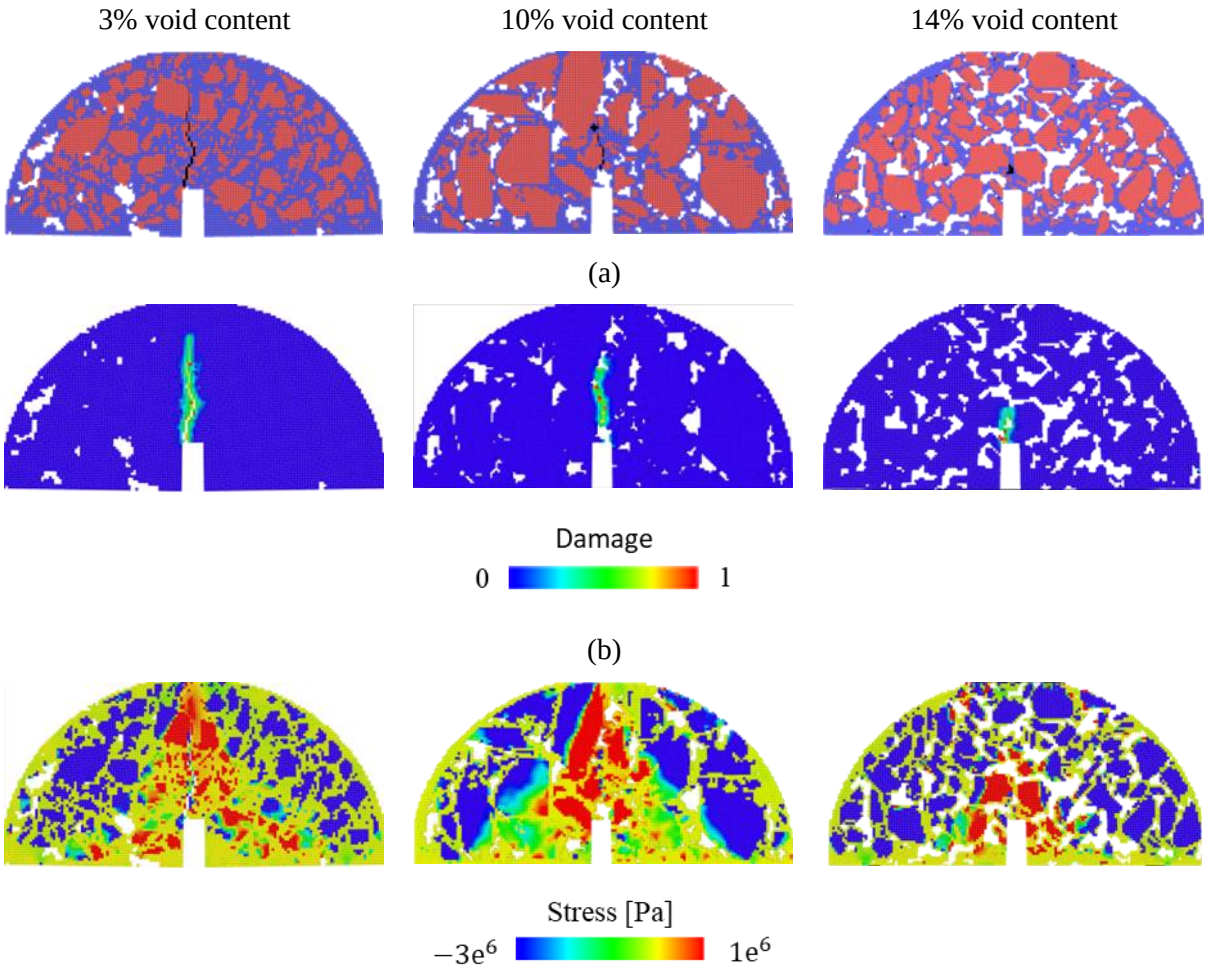

Figure 37: Asphalt mixture simulation at -10 °C. (a) asphalt at failure (damage in black), (b) bond broken at failure (particle at 0 value mean no broken bond and at 1 value mean fully broken, see section 2), (c) stress at failure (compression in blue and tension in red).

6.4.3 Validation of semi-circular bending test simulations at 20 °C with experimental results

To understand if Peridynamic can capture the mechanical and fracture properties of asphalt mixture at 20 °C, semi-circular bending tests of asphalt mixture have been simulated, and the stress-strain curves compared with experimental test results. The experimental and computational stress/strain

curves for the asphalt mixture with 10% void tested at 20 °C are compared in Figure 38, as an example.

At 20 °C the stress-strain curve shows three different stages; stages I and II are the undamaged stages where Stage I is the linear viscoelastic part and Stage II is the nonlinear viscoelastic part. Stage III is where damage and cracking occurred at a fast rate, see Figure 38 (b). In Stage I, the stress increases and there are no cracks. In Stage II while the stress increases with at a lower rate, the curve is softening reaching the peak load and some cracks appear. In Stage II, the highest difference between the experiment and simulation is 6.9% within the experimental results. The relative error is smaller compared with the simulations at -10 °C, indicating that the viscoelastic model is capable to reproduce nonlinearity behaviour, contrary to the elastic model. This result suggests that the VES reproduces the asphalt mixture's mechanical properties better than the LPS. Further investigations are required at a lower temperature using VES. In Stage III the stress reduced and reached a plateau; then, many cracks appeared, which induced plastic and viscoelastic deformations and no post-peak is observed [200]. In the Stage III simulation results, the fast breakage of bonds induced instability which explains the peaks and differences when compared to the experimental result. Figure 38 shows only the experimental result at the same strain deformation of the simulation for better visualisation and comparison of the curves. Furthermore, since the digital sample internal structure used in the simulation is not identical to the physical sample internal structure in the test, the result cannot be identical either, but fall within the same range.

At 20 °C, the damage affects not only areas above the notch, but also above the supports, around the voids, and at the interfaces, when the distance among aggregates is narrow, see Figure 39 (a) and (b). For instance, see Figure 40 as a higher-detail example of the damages at the interface and around the voids. The failure mode in the simulation is identical to the damage observed in the experiment discussed in 5.4.1.

The digital asphalt mixtures at 20 °C are characterised by many particles with bonds partially broken (the average damage value across the samples is 0.2) which allows the sample to withstand stress and still have bearing capacity.

Furthermore, the asphalt mixture with 10% void content shows lower damage (0.18 of damage) concentration across the sample. The bigger aggregate size confirms the beneficial effect on the fracture properties because the aggregate has higher fracture energy which required larger deformation, as explained in Section 4.1. For instance, the aggregates in the asphalt mixture with 10% void content has mostly zero damage across the XYZ direction, Figure 39 (b).

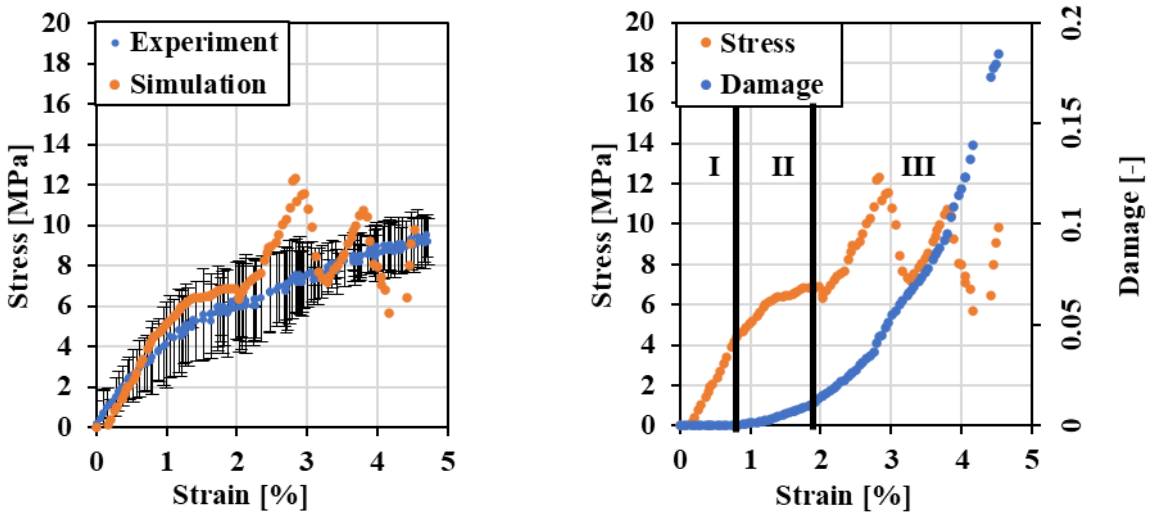

(a) (b)

Figure 38: (a) Experiment and computational results compared for asphalt mixture with 10% void at 20 °C, (b) Stress-strain curve and broken peridynamic bonds.

The local stress was monitored to assess the influence of the internal structure analysed above at the lower scale [151]. The stress analysis for the asphalt mixture at 20 °C, indicates that the aggregate skeleton was under compression stress, which confirms that provides the bearing capacity of the asphalt mixture, while the mastic and the interface mastic-aggregate were under tension stress, see Figure 40 (c). Furthermore, since the viscoelastic model used allows stress relaxation across the sample, the stress-induced the internal readjustment of the aggregates.

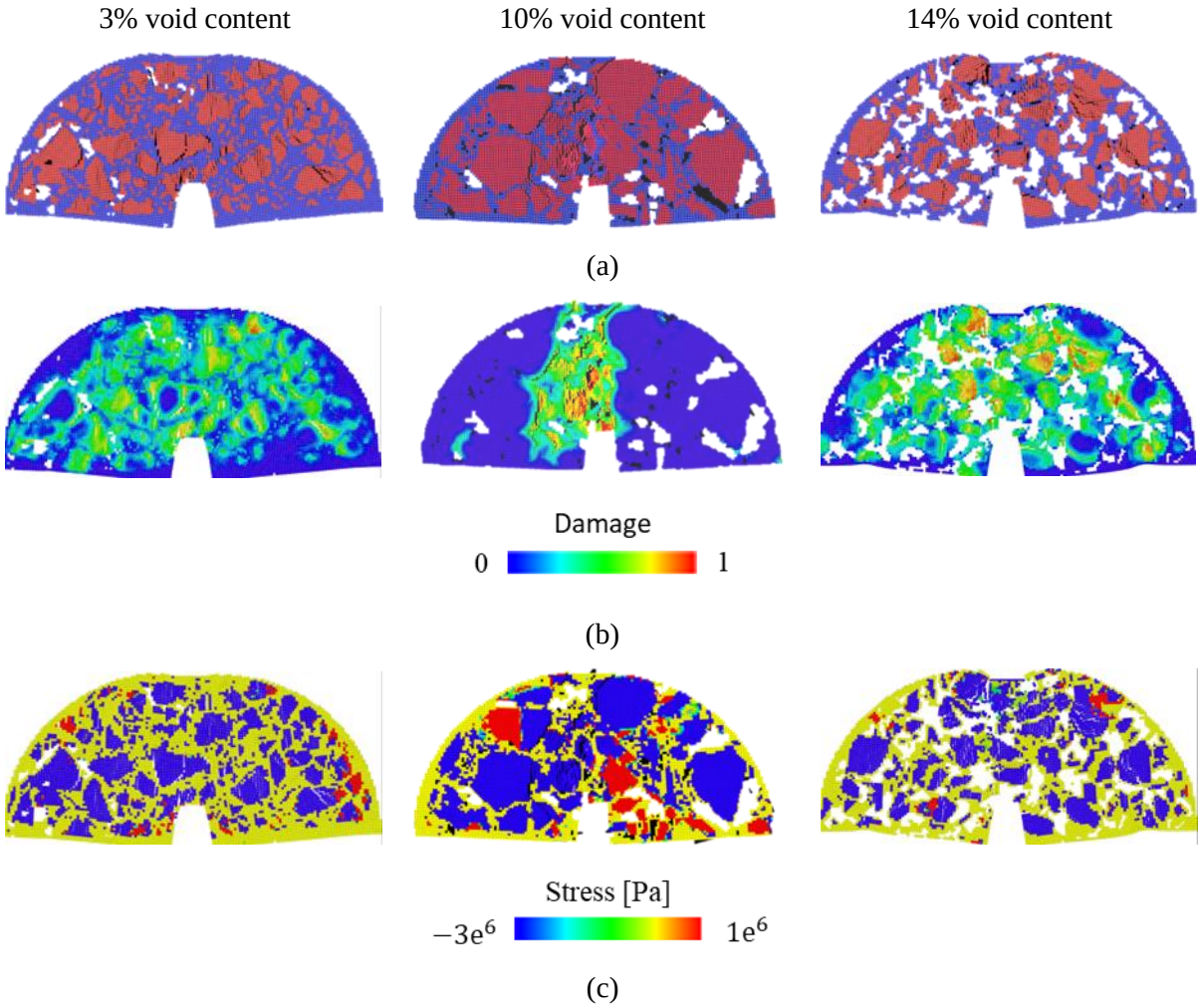

Figure 39: Asphalt mixture simulation at 20 °C. (a) asphalt mixture at failure (damage in black), (b) bond broken at failure, (c) stress at failure.

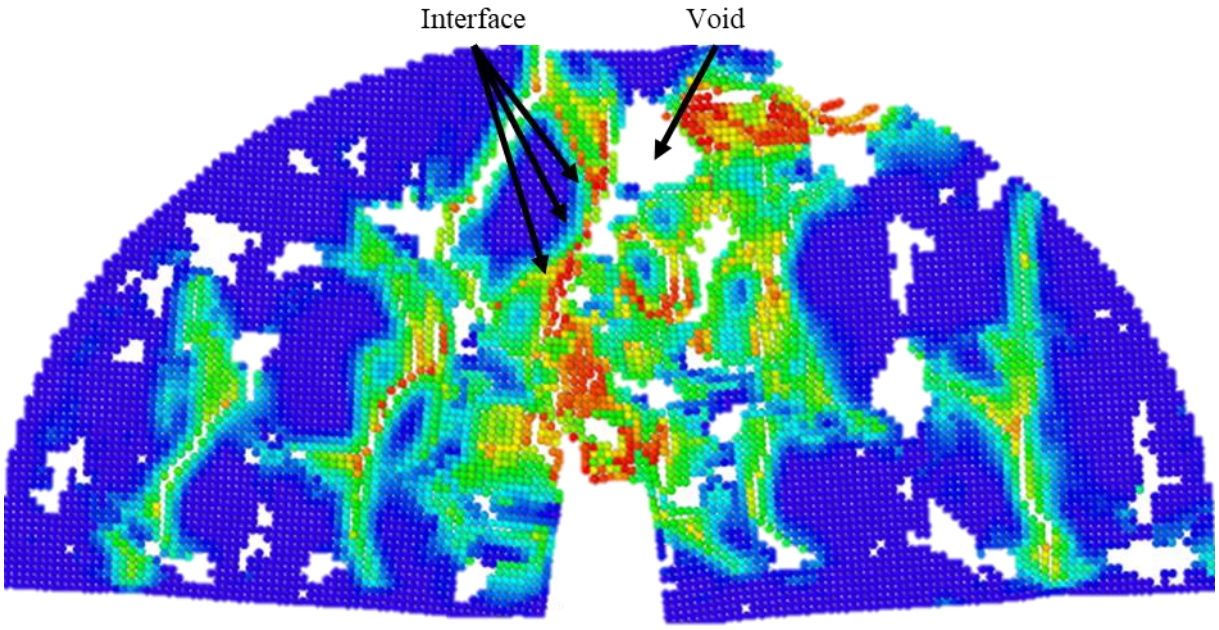

Figure 40: Asphalt mixture with 10% void content simulation at 20 ℃.

6.5 Conclusion

This paper demonstrated the use of the peridynamic modelling of asphalt mixture at -10 ºC and 20 ºC. These temperatures were chosen because of the very different behaviours that asphalt mixture presents. The mechanical and fracture properties of three types of asphalt mixture with target air voids content ranging from 3% to 14% were also discussed. Peridynamic simulations have been successfully used to obtain the stress-strain curves with a reasonable approximation at all temperatures.

The study obtained the following conclusions:

- Void and aggregates influence the performances. At low temperatures, high void content has a detrimental effect on it. However, at higher temperatures, the asphalt mixture with a 3% void has a lower ultimate strain. In addition, the shape plays an important role in the performance, indeed, elongated shape voids harm the mechanical properties.

- Asphalt mixture with 10% of void content has the highest aggregate content and the biggest size. This gradation provides good performances of asphalt mixture at all temperatures. Cracks at low temperatures start from the notch and seem to be strongly influenced by the stone. Considering the crack propagates through the interfaces, a bigger stone put an obstacle to its propagation of it. The asphalt mixture with 10% of void content experiences fractures after long strain.
- The asphalt mixture mechanical properties at -10 °C and 20 °C are replicated with 23.08% and 6.9% errors, respectively. The error may result from the different geometries used between the simulated asphalt and the real asphalt mixture tested at that condition. Despite this, the ultimate properties are within the range of average experimental results.
- The stress analysis for the asphalt mixture at -10 °C and 20 °C shows a similar result: the aggregate skeleton is under compression and provides the bearing capacity of the asphalt mixture, and the mastic is under tension.
- The highest concentration of stress predicts damage creation, and it is observed above the notch at low temperatures, voids, aggregate elongated parts, and narrow mastic areas among aggregates.
- Peridynamic can successfully detect cracks accurately. The damage creation and propagation in 3D are similar to the experimental results. The damages occur at the interfaces or mastic and propagates around aggregates.
- The stress at low temperatures is the highest above the notch, where damage occurs and propagates along the direction of loading in the area with high-stress values across the interfaces. In addition, the stone influences the damage. Since the crack propagates through the interfaces, a bigger stone can be an obstacle in the crack propagation.

- At high temperatures, the stress is more diffused across the sample with a lower concentration. The model allows stress relaxation. Damage occurs in the entire digital asphalt mixture (propagating slowly compared to the asphalt mixture at -10 °C).

This study provides a powerful tool in the field for reproducing and understanding the mechanical properties and fracture performances of asphalt mixture and all infrastructure material.

Chapter 7

Discussion, conclusion and future applications

7.1 Discussion

The literature review revealed extensive experimental research on the asphalt mixture mechanical and fracture properties under a variety of internal (aggregate type, gradation and void content) and external conditions (loading mode and environmental solicitation). However, the experimental tests are incapable or inadequate to provide information at a smaller scale and how phenomenon, like damage, occurs and evolves. The limitation was addressed using a computational tomography scan to observe the asphalt mixture at a smaller scale, evaluating the influence of external solicitation on the internal structure and how the internal structure evolves under these solicitations. The CT scans are expensive and require expertise to analyse the image and identify internal structure modification and damages. Numerical methods are a valid alternative to experimental methods and X-ray CT scans, because are cost-effective, provide information under a variety of conditions and can be applied combined with experiments and X-ray CT scans. The literature review indicates different numerical methods such as DEM and FEM. In particular, FEM was used to investigate asphalt mixtures. As seen from the literature, most studies were in 2D, the voids were not included and the aggregate was modelled as a polygon, only a few studies use realistic aggregate gradation, shape and distribution. Furthermore, FEM required a priori knowledge of the position of cracks to add a cohesive element to model damage. Despite the insertions of these elements, the damages and cracks appear different

from the experimental observations. Peridynamics is a promising numerical method for reproducing damage and cracks. The method does not require insertions or particular calculations for the input simulation values. The literature shows that this study is the first to use Peridynamic to model asphalt mixtures. Therefore, the results constitute the benchmark for further work and investigations.

In this thesis, we investigated the role of the temperature, water, and internal structure of asphalt mixture on its mechanical and fracture behaviours and developed a Peridynamic model to reproduce the asphalt mixture's performances.

In Chapter 4, we adopted Peridynamic and Discrete Multiphysics to reproduce the mechanical properties of asphalt mixture and its fracture behaviours at low temperatures and freezing conditions. Asphalt mixtures with different air void content were manufactured. The asphalt mixture's CT scan was used to recreate the digital asphalt mixture model with MATLAB and ImageJ to obtain the topology of voids. Additional digital geometries were generated to obtain several air voids content and to add water into the voids to simulate FT cycles. Preliminary validation of Peridynamic modelling of a tensile test on bitumen at -10 °C proved that the model replicates the mechanical and fracture properties with an error of 10%, which is in line with other studies in FEM with an error of 10% up to 20%. Simulations with different air void content at -10 °C and under freeze-thaw cycles were compared with literature result for similar asphalt mixtures. The analysis highlights the ability of the model to reproduce the negative influences of air void content and freeze-thaw cycle on mechanical properties. The model showed the ability to reproduce the asphalt mixture performance and damages under a different scenario.

In Chapter 5, we assessed a correlation between the mechanical and fracture characteristic of the internal structure of asphalt mixtures. Three asphalt mixtures with air void content of 3%, 10% and 14% were tested. The tests are carried out at -10 °C and under freeze-thaw cycles for asphalt mixtures

and mastics. The internal structure of asphalt mixture is acquired using the X-ray CT scan where we identified the correlation between the reduction of the mechanical properties and the internal modification of asphalt mixture under freezing cycles. The image analysis presents three different behaviours: 1) increasing existing void volume, 2) coalescing of existing voids, and 3) cracking and new void formations. The three asphalt mixtures perform differently under freeze-thaw cycles. These differences are attributed to the different air void content and aggregate gradations. Therefore, the asphalt mixture's durability is different. Analysing the evolution of the internal structure and mechanical properties under the freeze-thaw cycle, we observed two different stages: fast damage and slow damage. In the fast damage stage (up to 5 cycles) is observed a rapid creation of air void content and damages with a strong mechanical property decrease. In the slow damage stage (from 5 to 20 cycles) in observed a void coalescing predominance and a slower decrease of mechanical properties. The 10% void content asphalt mixture shows the highest level of damage in the fast damage because has the highest water retained observed in the X-Ray CT scan. The water retention was correlated with the reduction of the mechanical properties finding a linear correlation. The asphalt mixture with the 3% void content has less water retention. Therefore, the influence of the freeze-thaw cycle is minimal compared to the other asphalt mixture. The asphalt mixture with the 14% void content has less water retention than the 10% void content asphalt mixture. Hence, the reduction of the mechanical properties was lower. Based on the finding the internal void topology influences the asphalt mixture mechanical properties under the freeze-thaw cycle and the 10% void content asphalt mixture is the highest influenced due to the highest water retained. Therefore, the topology of void and water retained could be established as the index for asphalt mixture durability.

In Chapter 6, experiments on different asphalt mixtures are carried out at -10 °C and 20 °C to investigate the influence of temperature and void on the asphalt mixture performance. The temperatures were chosen because the asphalt mixtures behave differently. We analyse the influence

of the gradation of the asphalt mixture on the final properties observing that different gradations with the same materials can improve the asphalt mixture quality. The experimental test at -10 °C shows that asphalt mixture with high air void has the lowest mechanical properties. Furthermore, the shape of the voids plays an important role in the influence on the performances. The experiment result repeatability was evaluated with the calculation of the coefficient of variation, which is below 25% for all parameters calculated indicating a satisfactory condition. The finding was previously observed in the computational analysis in chapter 4, confirming the Peridynamics model can reproduce the asphalt mixture properties. The damage in the asphalt mixtures at -10 °C and 20 °C were analysed. We observed that at -10 °C the cracks start from the notch and propagate along the load direction at the interfaces between aggregate and mastic. Therefore, larger aggregate obstacles the propagation, creating a long crack path and increasing the mechanical properties of the asphalt mixtures. The asphalt mixture with 10% of air void has a larger aggregate (20 mm) and higher ultimate strain is observed. The model is used at -10 °C and 20 °C to reproduce the asphalt mixture's mechanical and fracture characteristics. We used the generation of the digital sample method in Chapter 4. The computational simulation of the asphalt mixture performed at -10 °C was compared with the experiments. The results show an elastic behaviour following two stages: in stage I the behaviour is elastic, and no cracks are observed. Although in the experiment the piston contacts the asphalt mixture sample, this results in re-accommodation of the sample, causing the stress to increase nonlinearly. In the simulation, the geometry is ideal, and no re-accommodation occurs. In stage II cracks are formed at the interface and the sample fails suddenly. The simulation results error calculated against the experimental result is 22.4% closest to the error in similar studies using FEM. Furthermore, the relative error of the Young modulus is 7% and the relative error between the air void content in the asphalt mixture samples and the digital reproduction is below 3%. The results reveal an accurate generation of the digital sample confirming the reliability of the model with errors in the same range

of other studies. The values are acceptable and in line with similar studies where the error was between 10 % and 20 % [12], [170], [171].

The simulations show a similar failure mode: crack starts from the notch and propagates along the loading direction across the interfaces, similar to the experimental tests. Furthermore, the stress analysis shows the aggregate skeleton is under compression and the mastic under tension with higher values close to the notch. In addition, the model allowed us to observe the increase of stress locally before the damage occurs.

The computational simulation of the asphalt mixture performed at 20 °C was compared with the experiments. The results show three stages: in stage I the behaviour is viscoelastic, and no cracks occur, and the stage II is nonlinear viscoelastic, the stress decreases and peak load is observed. The error in the simulation is 6.9%, lower than the simulation at -10 °C, indicating that the model can replicate the nonlinear behaviour. In stage III damages appear at a fast rate creating instability, post-peak is not observed like in the experiment. The simulations show a similar failure mode: cracks are formed across the sample, similar to the experimental tests. Furthermore, the stress analysis shows the aggregate skeleton is under compression and the mastic under tension. In addition, the model allowed us to observe the increase of stress locally before the damage occurs.

7.2 Conclusion

The road network experiences different loading and environmental condition reducing the lifespan. The numerical method is a useful tool to understand the asphalt mixture’s mechanical and fracture properties and its damage mechanisms. Compared to experimental tests, the numerical method provides a more flexible and cost-effective alternative to studying asphalt mixture behaviour and is fundamental to improving the design and preventing damage. The numerical methods used for asphalt

mixtures like DEM and FEM have limitations such as complicated procedure calculation for input value and unrealistic damage simulations. The proposed framework used Peridynamics and discrete multiphysics to investigate the asphalt mixture mechanical and fracture properties.

The research has demonstrated the objectives outlined in Chapter 1:

- Understand the role of the temperature, water, and internal structure of asphalt mixture on its mechanical and fracture behaviours.
- Develop a reliable procedure to simulate asphalt mixture or infrastructure material, in general, using Peridynamic and Peridynamic coupled with Lennard-Jones to reproduce the asphalt mixture performance. The advanced numerical model adds information which is unprovided by experiments such as local stress and damages

The following conclusions are drawn from the research:

- The experimental investigation at -10 °C, 20 °C and under freeze-thaw cycle together with the X-ray CT scans revealed a correlation between the internal structure evolution and mechanical properties influences. High void content reduces asphalt mixture performance as well as irregularity in the pores. A larger aggregate improves the fracture characteristic. Asphalt mixtures under the freeze-thaw cycle experience three changes: 1) creation of voids, 2) coalescing of existing voids, and 3) crack formation. Asphalt mixtures have different behaviour under the freeze-thaw cycle because have different voids and water content. The asphalt mixture with 10% void content has high water retention and experiences a higher reduction of mechanical properties.
- The Peridynamics and Discrete multiphysics methods reproduce the mechanical and fracture performance of asphalt mixture at -10 °C, 20 °C and under freeze-thaw cycle. The mechanical properties have an error of 22.4% at -10 °C in line with the other numerical methods and 6.9%

at 20 °C showing that the viscoelastic model reproduces nonlinearity behaviour compared to the linear elastic model. However, the viscoelastic model is unstable, and the post-peak is not reproduced. The cracks are similar to the experimental observation: at -10 °C cracks start from the notch and propagate through the interfaces along load direction and at 20 °C cracks appear also above the support and across the sample. The stress analysis confirms that the aggregate skeleton is under compression and the mastic under tension. At -10 °C, high-stress tension is observed in the notch. The reduction of the mechanical properties with the increased air void has been simulated and correlated as well as with the freeze-thaw cycle.

In conclusion, the thesis has demonstrated the capabilities of Peridynamic and Discrete Multiphysics in reproducing the asphalt mixture mechanical properties, cracks and damages.

7.3 Future works

Although the results presented have proven the reliability of Peridynamic to reproduce the asphalt mixture performance, further investigation is required to improve the numerical method.

The following research is recommended:

- The research presented herein relied on the use of a small range of air void content and aggregate gradations. Research should be carried out to investigate the role of different void content, aggregate gradation on the mechanical properties to understand the impact of the stone dimensions and shape on the ultimate properties
- The computational study involves only two temperatures (-10 °C, and 20 °C). The asphalt mixtures are employed in a wider range of temperatures from -30 °C to 50 °C. Therefore, a systematic study using a wide range of temperatures is useful to understand the impact on the internal structure.

- The simulation at -10 °C is unable to reproduce nonlinearity. The simulation at 20 °C can reproduce nonlinearity. The reliability of the viscoelastic model at low temperatures should be studied.
- Further research would be the application of this method on other infrastructure materials (e.g. concrete, masonry) to simulate its performance and ultimately improve endurance.
- The final step would be to use the model on a bigger scale to predict the lifetime of infrastructures.

8. Reference

[1] J. Read, D. Whiteoak, The Shell bitumen handbook, 2014.

[2] G.D. Airey, A.E. Hunter, A.C. Collop, The effect of asphalt mixture gradation and compaction energy on aggregate degradation, Constr. Build. Mater. 22 (2008) 972–980.

[3] D.H. Shen, M.F. Kuo, J.C. Du, Properties of gap-aggregate gradation asphalt mixture and permanent deformation, Constr. Build. Mater. 19 (2005) 147–153.

[4] J. Yi, S. Shen, B. Muhunthan, D. Feng, Viscoelastic-plastic damage model for porous asphalt mixtures: Application to uniaxial compression and freeze-thaw damage, Mech. Mater. 70 (2014) 67–75.

[5] M.M. Karimi, E.A. Dehaghi, A. Behnood, A fracture-based approach to characterise long-term performance of asphalt mixes under moisture and freeze-thaw conditions, Eng. Fract. Mech. 241 (2021) 107418.

[6] Z. Fan, H. Xu, J. Xiao, Y. Tan, Effects of freeze-thaw cycles on fatigue performance of asphalt mixture and development of fatigue-freeze-thaw (FFT) uniform equation, Constr. Build. Mater. 242 (2020) 118043.

[7] F. Canestrari, L.P. Ingrassia, A review of top-down cracking in asphalt pavements: Causes, models, experimental tools and future challenges, J. Traffic Transp. Eng. (English Ed. 7 (2020) 541–572.

[8] D. Sanfilippo, B. Ghiassi, A. Alexiadis, A.G. Hernandez, Combined peridynamics and discrete multiphysics to study the effects of air voids and freeze-thaw on the mechanical properties of asphalt, Materials (Basel). 14 (2021).

[9] D. Sanfilippo, A. Garcia-Hernández, A. Alexiadis, B. Ghiassi, Effect of freeze–thaw cycles on the void topologies and mechanical properties of asphalt, Constr. Build. Mater. 344 (2022) 128085.

[10] G. Saha, K.P. Biligiri, Fracture properties of asphalt mixtures using semi-circular bending test: A state-of-the-art review and future research, Constr. Build. Mater. 105 (2016) 103–112.

[11] F. Guo, J. Pei, J. Zhang, B. Xue, G. Sun, R. Li, Study on the adhesion property between asphalt binder and aggregate: A state-of-the-art review, Constr. Build. Mater. 256 (2020) 119474.

[12] X.J. Li, M.O. Marasteanu, Using Semi Circular Bending Test to Evaluate Low Temperature Fracture Resistance for Asphalt Concrete, Exp. Mech. 50 (2010) 867–876.

[13] X. Chen, M. Solaimanian, Effect of Test Temperature and Displacement Rate on Semicircular Bend Test, J. Mater. Civ. Eng. 31 (2019) 04019104.

[14] S. Pirmohammad, M. Abdi, M.R. Ayatollahi, Effect of support type on the fracture toughness and energy of asphalt concrete at different temperature conditions, Eng. Fract. Mech. 254 (2021) 107921.

[15] G. Saha, K.P. Biligiri, Fracture damage evaluation of asphalt mixtures using Semicircular Bending test based on fracture energy approach, Eng. Fract. Mech. 142 (2015) 154–169.

[16] L. Gao, H. Kong, X. Deng, Z. Wang, Multi-scale finite element simulation of asphalt mixture anti-cracking performance, Theor. Appl. Fract. Mech. 121 (2022).

[17] E. Coleri, J.T. Harvey, K. Yang, J.M. Boone, A micromechanical approach to investigate asphalt concrete rutting mechanisms, Constr. Build. Mater. 30 (2012) 36–49.

[18] I.M. Lancaster, H.A. Khalid, I.A. Kougioumtzoglou, Extended FEM modelling of crack propagation using the semi-circular bending test, Constr. Build. Mater. 48 (2013) 270–277.

[19] J. Ren, L. Sun, Characterising air void effect on fracture of asphalt concrete at low-temperature using discrete element method, Eng. Fract. Mech. 170 (2017) 23–43.

[20] B. Xue, J. Pei, B. Zhou, J. Zhang, R. Li, F. Guo, Using random heterogeneous DEM model to simulate the SCB fracture behavior of asphalt concrete, Constr. Build. Mater. 236 (2020) 117580.

[21] J. Kollmann, P. Liu, G. Lu, D. Wang, M. Oeser, S. Leischner, Investigation of the microstructural fracture behaviour of asphalt mixtures using the finite element method, Constr. Build. Mater. 227 (2019) 117078.

[22] Pazdniakou, P.M. Adler, Lattice spring models, Transp. Porous Media. 93 (2012) 243–262.

[23] S.A. Silling, Reformulation of elasticity theory for discontinuities and long-range forces, J. Mech. Phys. Solids. 48 (2000) 175–209.

[24] W.G. Buttlar, Z. You, Discrete element modeling of asphalt concrete: Microfabric approach, Transp. Res. Rec. (2001) 111–118.

[25] J. Mehrmashhadi, L. Wang, F. Bobaru, Uncovering the dynamic fracture behavior of PMMA with peridynamics: The importance of softening at the crack tip, Eng. Fract. Mech. 219 (2019) 106617.

[26] N. Sukumar, D.L. Chopp, N. Moës, T. Belytschko, Modeling holes and inclusions by level sets in the extended finite-element method, Comput. Methods Appl. Mech. Eng. 190 (2001) 6183–6200.

[27] C. Jiang, G.F. Zhao, N. Khalili, On crack propagation in brittle material using the distinct lattice spring model, Int. J. Solids Struct. 118–119 (2017) 1339–1351.

[28] J. Guo, W. Gao, Z. Liu, X. Yang, F. Li, Study of Dynamic Brittle Fracture of Composite Lamina Using a Bond-Based Peridynamic Lattice Model, Adv. Mater. Sci. Eng. 2019 (2019).

[29] S.A. Silling, M. Epton, O. Weckner, J. Xu, E. Askari, Peridynamic states and constitutive modeling, 2007.

[30] J. a. Mitchell, Non-Local, Ordinary-State-Based Viscoelasticity Model for Peridynamics, Sandia Rep. SAND2011-8 (2011) 28p.

[31] J.A. Mitchell, A Nonlocal , Ordinary , State-Based Plasticity Model for Peridynamics, Sandia Rep. (2011) 1–34.

[32] Simanzhenkov V, Idem R. Crude oil chemistry. CRC Press; 2003.

[33] Asphalt Institute, European Bitumen Association. The Bitumen Industry - a Global Perspective: Production, Chemistry, Use, Specification and Occupational Exposure. Asphalt Institute; 2015.

[34] J. Chen, L. Zhang, Y. Du, H. Wang, H. Dan, Three-dimensional microstructure based model for evaluating the coefficient of thermal expansion and contraction of asphalt concrete, Constr. Build. Mater. 284 (2021) 122764.

[35] A.W. Hefer, A. Bhasin, D.N. Little, Bitumen Surface Energy Characterization Using a Contact Angle Approach, J. Mater. Civ. Eng. 18 (2006) 759–767.

[36] M. Buczkó, Z. Dezső, J. Csikai, Determination of the bitumen content in asphalt concrete using a neutron reflection method, J. Radioanal. Chem. 25 (1975) 179–183.

[37] BSI (2002) BS EN 13043:2002. Aggregates for bituminous mixtures and surface treatments for roads, airfields and other trafficked areas. BSI, London, UK.

[38] A.H. Albayati, H. Abdulsattar, Performance evaluation of asphalt concrete mixes under varying replacement percentages of natural sand, Results Eng. 7 (2020) 100131.

[39] Y. Li, P. Hao, C. Zhao, J. Ling, T. Wu, D. Li, J. Liu, B. Sun, Anti-rutting performance evaluation of modified asphalt binders: A review, J. Traffic Transp. Eng. (English Ed. 8 (2021) 339–355.

[40] X. Zhang, B. Zhang, H. Chen, D. Kuang, Feasibility evaluation of preparing asphalt mixture with low-grade aggregate, rubber asphalt and desulphurization gypsum residues, Materials (Basel). 11 (2018).

[41] L.H. Csanyi, Funtions of fillers in bituminous mixes, Symp. Miner. Fill. Bitum. Mix. (1962) 1–5.

[42] F. Mastoras, A. Varveri, M. van Tooren, S. Erkens, Effect of mineral fillers on ageing of bituminous mastics, Constr. Build. Mater. 276 (2021) 122215.

[43] J. Ren, Y. Xu, J. Huang, Y. Wang, Z. Jia, Gradation optimization and strength mechanism of aggregate structure considering macroscopic and mesoscopic aggregate mechanical behaviour in porous asphalt mixture, Constr. Build. Mater. 300 (2021) 124262.

[44] O. Šernas, A. Vaitkus, J. Gražulytė, D. Skrodenis, M. Wasilewska, P. Gierasimiuk, Development of low noise and durable semi-dense asphalt mixtures, Constr. Build. Mater. 293 (2021).

[45] A.M. Zaltuom, A Review Study of The Effect of Air Voids on Asphalt Pavement Life, 2 (2018) 618–625.

[46] K.Y. Kim, T.S. Yun, J. Choo, D.H. Kang, H.S. Shin, Determination of air-void parameters of hardened cement-based materials using X-ray computed tomography, Constr. Build. Mater. 37 (2012) 93–101.

[47] BSI (2012b) BS EN 933-3:2012. Tests for geometrical properties of aggregates. Determination of particle shape – Flakiness index. BSI, London, UK

[48] BSI (2008a) BS EN 933-4:2008. Tests for geometrical properties of aggregates. Determination of particle shape. Shape index. BSI, London, UK.

[49] BSI Standards Publication Bituminous mixtures — Material specifications Part 5 : Stone Mastic Asphalt, BSI Br. Stand. (2016).

[50] L. Shi, D. Wang, C. Jin, B. Li, H. Liang, Measurement of coarse aggregates movement characteristics within asphalt mixture using digital image processing methods, Meas. J. Int. Meas. Confed. 163 (2020) 107948.

[51] L. Shi, X. Xiao, X. Wang, H. Liang, D. Wang, Mesostructural characteristics and evaluation of asphalt mixture contact chain complex networks, Constr. Build. Mater. 340 (2022) 127753.

[52] Y. Du, J. Chen, Z. Han, W. Liu, A review on solutions for improving rutting resistance of asphalt pavement and test methods, Constr. Build. Mater. 168 (2018) 893–905.

[53] H. Taherkhani, Experimental Characterisation of the Compressive Permanent Deformation Behaviour in Asphaltic Mixtures, (2006).

[54] W. Cai, G.R. McDowell, G.D. Airey, Discrete element modelling of uniaxial constant strain rate tests on asphalt mixtures, Granul. Matter. 15 (2013) 163–174.

[55] S. Starodubsky, I. Blechman, M. Livneh, Stress-strain relationship for asphalt concrete in compression, Mater. Struct. 27 (1994) 474–482.

[56] Goodrich, J L. “asphalt and polymer modified asphalt properties related to the performance of asphalt concrete mixes (with discussion).” (1988).

[57] C. Der Van Poel, A general system describing the visco-elastic properties of bitumens and its relation to routine test data, J. Appl. Chem. 4 (2007) 221–236.

[58] P. Li, X. Jiang, K. Guo, Y. Xue, H. Dong, Analysis of viscoelastic response and creep deformation mechanism of asphalt mixture, Constr. Build. Mater. 171 (2018) 22–32.

[59] T. Ma, D. Zhang, Y. Zhang, J. Hong, Micromechanical response of aggregate skeleton within asphalt mixture based on virtual simulation of wheel tracking test, Constr. Build. Mater. 111 (2016) 153–163.

[60] L.S. de Oliveira, J.L.O. Lucas Júnior, L.F.A.L. Babadopulos, J.B. Soares, Stiffness and fatigue evaluation in cyclic tests with rest periods for asphalt mixtures with or without fly ash, Constr. Build. Mater. 322 (2022) 126426.

[61] M.L. Williams, R.F. Landel, J.D. Ferry, The Temperature Dependence of Relaxation Mechanisms in Amorphous Polymers and Other Glass-forming Liquids, J. Am. Chem. Soc. 77 (1955) 3701–3707.

[62] R. Delorme, I. Tabiai, L. Laberge, L. Martin, Generalization of the ordinary state-based peridynamic model for isotropic linear viscoelasticity, Mech Time-Depend Mater. (2017) 549–575.

[63] C. Wang, H. Zhang, C. Castorena, J. Zhang, Y.R. Kim, Identifying fatigue failure in asphalt binder time sweep tests, Constr. Build. Mater. 121 (2016) 535–546.

[64] H. Wang, J. Wang, J. Chen, Micromechanical analysis of asphalt mixture fracture with adhesive and cohesive failure, Eng. Fract. Mech. 132 (2014) 104–119.

[65] A. Rahman, H. Huang, C. Ai, H. Ding, C. Xin, Y. Lu, Fatigue performance of interface bonding between asphalt pavement layers using four-point shear test set-up, Int. J. Fatigue. 121 (2019) 181–190.

[66] L. Wang, M. Ren, Y. Xing, G. Chen, Study on affecting factors of interface crack for asphalt mixture based on microstructure, Constr. Build. Mater. 156 (2017) 1053–1062.

[67] Q. Guo, G. Li, Y. Gao, K. Wang, Z. Dong, F. Liu, H. Zhu, Experimental investigation on bonding property of asphalt-aggregate interface under the actions of salt immersion and freeze-thaw cycles, Constr. Build. Mater. 206 (2019) 590–599.

[68] J.P. Aguiar-Moya, A. Baldi-Sevilla, J. Salazar-Delgado, J.F. Pacheco-Fallas, L. Loria-Salazar, F. Reyes-Lizcano, N. Cely-Leal, Adhesive properties of asphalts and aggregates in tropical climates, Int. J. Pavement Eng. 19 (2018) 738–747.

[69] S. Xu, F. Xiao, S. Amirkhanian, D. Singh, Moisture characteristics of mixtures with warm mix asphalt technologies – A review, Constr. Build. Mater. 142 (2017) 148–161.

[70] A. Massahi, H. Ali, F. Koohifar, M. Baqersad, ScienceDirect Investigation of pavement raveling performance using smartphone, Int. J. Pavement Res. Technol. 11 (2018) 553–563.

[71] K.A. Ghuzlan, B.W. Al-Mistarehi, A.S. Al-Momani, Rutting performance of asphalt mixtures with gradations designed using Bailey and conventional Superpave methods, Constr. Build. Mater. 261 (2020) 119941.

[72] Y.S. Jenq, C.J. Liaw, P. Liu, Analysis of crack resistance of asphalt concrete overlays. A fracture mechanics approach, Transp. Res. Rec. (1993) 160–166.

[73] U. Bagampadde, U. Isacsson, B.M. Kiggundu, Classical and Contemporary Aspects of Stripping in Bituminous Mixes, Road Mater. Pavement Des. 5 (2004) 7–43.

[74] Y. Tan, M. Guo, Using surface free energy method to study the cohesion and adhesion of asphalt mastic, Constr. Build. Mater. 47 (2013) 254–260.

[75] R. Zhang, W. Zhang, S. Shen, S. Wu, Y. Zhang, Evaluation of the correlations between laboratory measured material properties with field cracking performance for asphalt pavement, Constr. Build. Mater. 301 (2021) 124126.

[76] R. Zhang, J. Huang, W. Zheng, Evaluation of the significance of different mix design variables on asphalt mixtures' cracking performance measured by laboratory performance tests, Constr. Build. Mater. 350 (2022) 128693.

[77] B.P. Das, A.K. Siddagangaiah, Identification of parameter to assess cracking resistance of asphalt mixtures subjected to aging and moisture conditioning, J. Traffic Transp. Eng. (English Ed. 9 (2022) 293–304.

[78] Y.R. Kim, Cohesive zone model to predict fracture in bituminous materials and asphaltic pavements: State-of-the-art review, Int. J. Pavement Eng. 12 (2011) 343–356.

[79] A.A. Abdulshafi, K. Majidzadeh, J-Integral and Cyclic Plasticity Approach To Fatigue and Fracture of Asphaltic Mixtures., Transp. Res. Rec. (1985) 112–123.

[80] G.R. Chehab, Y.R. Kim, R.A. Schapery, M.W. Witczak, R. Bonquist, Characterization of asphalt concrete in uniaxial tension using a viscoelastoplastic continuum damage model, Asph. Paving Technol. Assoc. Asph. Paving Technol. Tech. Sess. 72 (2003) 315–355.

[81] A.A. Griffith, VI. The phenomena of rupture and flow in solids. Philosophical transactions of the royal society of london. Series A, containing papers of a mathematical or physical character, 221 (582-593) (1921) 163-198.

[82] J. Suchorzewski, J. Tejchman, M. Nitka, Discrete element method simulations of fracture in concrete under uniaxial compression based on its real internal structure, Int. J. Damage Mech. 27 (2018) 578–607.

[83] C. Du, Y. Sun, J. Chen, H. Gong, X. Wei, Z. Zhang, Analysis of cohesive and adhesive damage initiations of asphalt pavement using a microstructure-based finite element model, Constr. Build. Mater. 261 (2020) 119973.

[84] S. Wu, R. He, H. Chen, Y. Luo, Low temperature characteristics of asphalt mixture based on the semi-circular bend and thermal stress restrained specimen test in alpine cold regions, Constr. Build. Mater. 311 (2021) 125300.

[85] X. Luo, R. Luo, R.L. Lytton, Energy-Based Crack Initiation Criterion for Viscoelastoplastic Materials with Distributed Cracks, J. Eng. Mech. 141 (2015) 04014114.

[86] Y. Gao, L. Li, Y. Zhang, Modelling crack initiation in bituminous binders under a rotational shear fatigue load, Int. J. Fatigue. 139 (2020) 105738.

[87] G. Zeng, X. Yang, L. Chen, F. Bai, Damage Evolution and Crack Propagation in Semicircular Bending Asphalt Mixture Specimens, Acta Mech. Solida Sin. 29 (2016) 596–609.

[88] G. Teng, C. Zheng, X. Chen, X. Lan, Y. Zhu, C. Shan, Numerical fracture investigation of single-edge notched asphalt concrete beam based on random heterogeneous FEM model, Constr. Build. Mater. 304 (2021) 124581.

[89] E. Organ, S. Serin, Investigation of certain engineering characteristics of asphalt concrete exposed to freeze-thaw cycles, Cold Reg. Sci. Technol. 85 (2013) 131–136.

[90] M. Fakhri, S. Ali Siyadati, M.R.M. Aliha, Impact of freeze–thaw cycles on low temperature mixed mode I/II cracking properties of water saturated hot mix asphalt: An experimental study, Constr. Build. Mater. 261 (2020).

[91] M. Sol-Sánchez, F. Moreno-Navarro, G. García-Travé, M.C. Rubio-Gámez, Laboratory study of the long-term climatic deterioration of asphalt mixtures, Constr. Build. Mater. 88 (2015) 32–40.

[92] S. Badeli, A. Carter, G. Doré, Complex Modulus and Fatigue Analysis of Asphalt Mix after Daily Rapid Freeze-Thaw Cycles, J. Mater. Civ. Eng. 30 (2018) 04018056.

[93] Y. Cheng, Di Yu, G. Tan, C. Zhu, Low-temperature performance and damage constitutive model of eco-friendly basalt fiber-diatomite-modified asphalt mixture under freeze-thaw cycles, Materials (Basel). 11 (2018).

[94] J. Li, F. Wang, F. Yi, J. Ma, Z. Lin, Fractal analysis of the fracture evolution of freeze-thaw damage to asphalt concrete, Materials (Basel). 12 (2019).

[95] L. Cong, M. Ren, J. Shi, F. Yang, G. Guo, Experimental investigation on performance deterioration of asphalt mixture under freeze–thaw cycles, Int. J. Transp. Sci. Technol. 9 (2020) 218–228.

[96] G. Xu, Y. Yu, D. Cai, G. Xie, X. Chen, J. Yang, Multi-scale damage characterisation of asphalt mixture subject to freeze-thaw cycles, Constr. Build. Mater. 240 (2020) 117947

[97] M.B. Bouraima, Y. Qiu, Investigation of influential factors on the tensile strength of cold recycled mixture with bitumen emulsion due to moisture conditioning, J. Traffic Transp. Eng. (English Ed. 4 (2017) 198–205.

[98] G.P. Piuzzi, H.C. Scheuermann Filho, J.A. Villena Del Carpio, N.C. Consoli, The effects of porosity, asphalt content and fiberglass incorporation on the tensile strength and resilient modulus of asphalt concrete blends, Geotext. Geomembranes. 49 (2021) 864–870.

[99] T. Bennert, E. Haas, E. Wass, Indirect tensile test (IDT) to determine asphalt mixture performance indicators during quality control testing in New Jersey, Transp. Res. Rec. 2672 (2018) 394–403.

[100] K.P. Biligiri, S. Said, H. Hakim, Asphalt mixtures' crack propagation assessment using semi circular bending tests, Int. J. Pavement Res. Technol. 5 (2012) 209–217.

[101] S.H. Chang, C.I. Lee, S. Jeon, Measurement of rock fracture toughness under modes I and II and mixed-mode conditions by using disc-type specimens, Eng. Geol. 66 (2002) 79–97.

[102] BS EN 12697-44-2010--[2022-05-23--05-17-56 PM].pdf, (n.d.).

[103] M.D. Kuruppu, Y. Obara, M.R. Ayatollahi, K.P. Chong, T. Funatsu, ISRM-suggested method for determining the mode i static fracture toughness using semi-circular bend specimen, Rock Mech. Rock Eng. 47 (2014) 267–274.

[104] D.X. Lu, H.H. Bui, M. Saleh, Effects of specimen size and loading conditions on the fracture behaviour of asphalt concretes in the SCB test, Eng. Fract. Mech. 242 (2021) 107452.

[105] M. Arabani, B. Ferdowsi, Evaluating the Semi-Circular Bending Test for hma mixtures, Int. J. Eng. Trans. A Basics. 22 (2009) 47–58.

[106] B. Huang, X. Shu, G. Zuo, Using notched semi circular bending fatigue test to characterize fracture resistance of asphalt mixtures, Eng. Fract. Mech. 109 (2013) 78–88.

[107] H. Ziari, M.R.M. Aliha, A. Moniri, Y. Saghafi, Crack resistance of hot mix asphalt containing different percentages of reclaimed asphalt pavement and glass fiber, Constr. Build. Mater. 230 (2020) 117015.

[108] M. Fakhri, E. Haghighat Kharrazi, M.R.M. Aliha, F. Berto, The effect of loading rate on fracture energy of asphalt mixture at intermediate temperatures and under different loading modes, Frat. Ed Integrita Strutt. 12 (2018) 113–132.

[109] I. Artamendi, H.A. Khalid, A comparison between beam and semi-circular bending fracture tests for asphalt, Road Mater. Pavement Des. 7 (2006) 163–180.

[110] R.A. Tarefder, E.M. Kias, T. Ng, Factors affecting cracking of notched asphalt concrete, Int. J. Pavement Res. Technol. 2 (4) (2009) 137–147.

[111] I.S. Darma, T. Sugiyama, M.A.B. Promentilla, Application of X-ray CT to study diffusivity in cracked concrete through the observation of tracer transport, J. Adv. Concr. Technol. 11 (2013) 266–281.

[112] S. Guo, Q. Dai, X. Sun, X. Xiao, X-ray CT characterization and fracture simulation of ASR damage of glass particles in alkaline solution and mortar, Theor. Appl. Fract. Mech. 92 (2017) 76–88.

[113] Z. You, S. Adhikari, M. Emin Kutay, Dynamic modulus simulation of the asphalt concrete using the X-ray computed tomography images, Mater. Struct. Constr. 42 (2009) 617–630.

[114] S. Erdem, X-ray computed tomography and fractal analysis for the evaluation of segregation resistance, strength response and accelerated corrosion behaviour of self-compacting lightweight concrete, Constr. Build. Mater. 61 (2014) 10–17.

[115] J. Hu, Z. Qian, D. Wang, M. Oeser, Influence of aggregate particles on mastic and air-voids in asphalt concrete, Constr. Build. Mater. 93 (2015) 1–9.

[116] Y. Liu, Q. Dai, Z. You, Viscoelastic Model for Discrete Element Simulation of Asphalt Mixtures, J. Eng. Mech. 135 (2009) 324–333.

[117] H. Kim, M.P. Wagoner, W.G. Buttlar, Micromechanical fracture modeling of asphalt concrete using a single-edge notched beam test, Mater. Struct. Constr. 42 (2009) 677–689.

[118] H. Kim, M.P. Wagoner, W.G. Buttlar, Simulation of Fracture Behavior in Asphalt Concrete Using a Heterogeneous Cohesive Zone Discrete Element Model, J. Mater. Civ. Eng. 20 (2008) 552–563.

[119] A. Farhidzadeh, E. Dehghan-Niri, A. Moustafa, S. Salamone, A. Whittaker, Damage Assessment of Reinforced Concrete Structures Using Fractal Analysis of Residual Crack Patterns, Exp. Mech. 53 (2013) 1607–1619.

[120] A. Bhasin, A. Izadi, S. Bedgaker, Three dimensional distribution of the mastic in asphalt composites, Constr. Build. Mater. 25 (2011) 4079–4087.

[121] E. Coleri, J.T. Harvey, K. Yang, J.M. Boone, Micromechanical investigation of open-graded asphalt friction courses' rutting mechanisms, Constr. Build. Mater. 44 (2013) 25–34.

[122] T. You, R.K. Abu Al-Rub, M.K. Darebin, E.A. Masad, D.N. Little, Three-dimensional microstructural modeling of asphalt concrete using a unified viscoelastic-viscoplastic-viscodamage model, Constr. Build. Mater. 28 (2012) 531–548.

[123] J. Jiang, F. Ni, X. Gu, L. Yao, Q. Dong, Evaluation of aggregate packing based on thickness distribution of asphalt binder, mastic and mortar within asphalt mixtures using multiscale methods, Constr. Build. Mater. 222 (2019) 717–730.

[124] J. Hu, P. Liu, D. Wang, M. Oeser, Y. Tan, Investigation on fatigue damage of asphalt mixture with different air-voids using microstructural analysis, Constr. Build. Mater. 125 (2016) 936–945.

[125] J. Jiang, F. Ni, Q. Dong, L. Yao, X. Ma, Investigation of the internal structure change of two-layer asphalt mixtures during the wheel tracking test based on 2D image analysis, Constr. Build. Mater. 209 (2019) 66–76.

[126] S. Diamond, Aspects of concrete porosity revisited, Cem. Concr. Res. 29 (1999) 1181–1188.

[127] J.D. Lin, M.C. Yeh, P.H. Sung, R.H. Shiu, Preliminary study on X-ray computed tomography to evaluate voids in porous asphalt concrete, Appl. Mech. Mater. 174–177 (2012) 345–353.

[128] P. Stroeven, J. Hu, Review paper - Stereology: Historical perspective and applicability to concrete technology, Mater. Struct. Constr. 39 (2006) 127–135.

[129] L. Chu, T.F. Fwa, Functional sustainability of single- and double-layer porous asphalt pavements, Constr. Build. Mater. 197 (2019) 436–443.

[130] I. Jerjen, L.D. Poulikakos, M. Plamondon, P. Schuetz, T. Luethi, A. Flisch, Drying of Porous Asphalt Concrete Investigated by X-Ray Computed Tomography, Phys. Procedia. 69 (2015) 451–456.

[131] A. du Plessis, W.P. Boshoff, A review of X-ray computed tomography of concrete and asphalt construction materials, Constr. Build. Mater. 199 (2019) 637–651.

[132] S. Guo, Q. Dai, X. Sun, X. Xiao, R. Si, J. Wang, Reduced alkali-silica reaction damage in recycled glass mortar samples with supplementary cementitious materials, J. Clean. Prod. 172 (2018) 3621–3633.

[133] T. Suzuki, H. Ogata, R. Takada, M. Aoki, M. Ohtsu, Use of acoustic emission and X-ray computed tomography for damage evaluation of freeze-thawed concrete, Constr. Build. Mater. 24 (2010) 2347–2352.

[134] J. Yuan, Y. Liu, Z. Tan, B. Zhang, Investigating the failure process of concrete under the coupled actions between sulfate attack and drying-wetting cycles by using X-ray CT, Constr. Build. Mater. 108 (2016) 129–138.

[135] A. du Plessis, I. Yadroitsava, S.G. le Roux, I. Yadroitsev, J. Fieres, C. Reinhart, P. Rossouw, Prediction of mechanical performance of Ti6Al4V cast alloy based on micro CT-based load simulation, J. Alloys Compd. 724 (2017) 267–274.

[136] P.A.. Cundall, O.D.L. Strack, Cundall_Strack.Pdf, Geotechnique. 29 (1979) 47–65.

[137] L. Al Khateeb, K. Anupam, S. Erkens, T. Scarpas, Micromechanical simulation of porous asphalt mixture compaction using discrete element method (DEM), Constr. Build. Mater. 301 (2021) 124305.

[138] Z. Yan, S.K. Wilkinson, E.H. Stitt, M. Marigo, Discrete element modelling (DEM) input parameters: understanding their impact on model predictions using statistical analysis, Comput. Part. Mech. 2 (2015) 283–299.

[139] D.J. Kirkner, P.N. Caulfield, D.M. McCann, Three-dimensional, finite-element simulation of permanent deformations in flexible pavement systems, Transp. Res. Rec. (1994) 34–39.

[140] A. Kotousov, F. Berto, P. Lazzarin, F. Pegorin, Three dimensional finite element mixed fracture mode under anti-plane loading of a crack, Theor. Appl. Fract. Mech. 62 (2012) 26–33.

[141] A. Kotousov, P. Lazzarin, F. Berto, L.P. Pook, Three-dimensional stress states at crack tip induced by shear and anti-plane loading, Eng. Fract. Mech. 108 (2013) 65–74.

[142] N. Moës, J. Dolbow, T. Belytschko, A finite element method for crack growth without remeshing, Int. J. Numer. Methods Eng. 46 (1999) 131–150.

[143] T. Belytschko, T. Black, Elastic crack growth in finite elements with minimal remeshing, Int. J. Numer. Methods Eng. 45 (1999) 601–620.

[144] Y. Zhao, J. Jiang, L. Zhou, Y. Dai, F. Ni, Meso-structure image pre-selection method for two-dimensional finite element modeling in beam bending simulation of asphalt mixture, Constr. Build. Mater. 268 (2021) 121129.

[145] G.I. Barenblatt, The Mathematical Thsory of Equilibrium Cracks in Brittle Fracture (Initial Experiment for Hydogel as a Medium for...), Adv. Appl. Mech. 7 (1962) 55–129.

[146] X.P. Xu, A. Needleman, Numerical simulations of fast crack growth in brittle solids, J. Mech. Phys. Solids. 42 (1994) 1397–1434.

[147] N. Moës, T. Belytschko, Extended finite element method for cohesive crack growth, Eng. Fract. Mech. 69 (2002) 813–833.

[148] G.J. Wagner, N. Moës, W.K. Liu, T. Belytschko, The extended finite element method for rigid particles in Stokes flow, Int. J. Numer. Methods Eng. 51 (2001) 293–313.

[149] T. Belytschko, H. Chen, J. Xu, G. Zi, Dynamic crack propagation based on loss of hyperbolicity and a new discontinuous enrichment, Int. J. Numer. Methods Eng. 58 (2003) 1873–1905.

[150] G. Zi, T. Rabczuk, W. Wall, Extended meshfree methods without branch enrichment for cohesive cracks, Comput. Mech. 40 (2007) 367–382.

[151] W. Song, Z. Deng, H. Wu, Y. Zhan, Extended finite element modeling of hot mix asphalt based on the semi-circular bending test, Constr. Build. Mater. 340 (2022) 127462.

[152] J. Oliyer, Continuum modelling of strong discontinuities in solid mechanics using damage models, Comput. Mech. 17 (1995) 49–61.

[153] S.A. Silling, E. Askari, A meshfree method based on the peridynamic model of solid mechanics, Comput. Struct. 83 (2005) 1526–1535.

[154] M. Ostoja-Starzewski, Lattice models in micromechanics, Appl. Mech. Rev. 55 (2002) 35–59.

[155] M. Kot, H. Nagahashi, P. Szymczak, Elastic moduli of simple mass spring models, Vis. Comput. 31 (2015) 1339–1350.

[156] A. Javili, R. Morasata, E. Oterkus, S. Oterkus, Peridynamics review, Math. Mech. Solids. 24 (2019) 3714–3739.

[157] M. Zaccariotto, F. Luongo, G. Sarego, U. Galvanetto, Examples of applications of the peridynamic theory to the solution of static equilibrium problems, Aeronaut. J. 119 (2015) 677–700.

[158] Y. Shou, X. Zhou, F. Berto, 3D numerical simulation of initiation, propagation and coalescence of cracks using the extended non-ordinary state-based peridynamics, Theor. Appl. Fract. Mech. 101 (2019) 254–268.

[159] Y. Gao, S. Oterkus, Fully coupled thermomechanical analysis of laminated composites by using ordinary state based peridynamic theory, Compos. Struct. 207 (2019) 397–424.

[160] L. Guo, X. Zhang, W. Li, X. Zhou, Multi-scale peridynamic formulations for chloride diffusion in concrete, Eng. Anal. Bound. Elem. 120 (2020) 107–117.

[161] Y. Sun, B. Chen, M.G. Edwards, C. Li, Investigation of hydraulic fracture branching in porous media with a hybrid finite element and peridynamic approach, Theor. Appl. Fract. Mech. 116 (2021) 103133.

[162] T.L. Warren, S.A. Silling, A. Askari, O. Weckner, M.A. Epton, J. Xu, A non-ordinary state-based peridynamic method to model solid material deformation and fracture, Int. J. Solids Struct. 46 (2009) 1186–1195.

[163] M.L. Parks, R.B. Lehoucq, S.J. Plimpton, S.A. Silling, Implementing peridynamics within a molecular dynamics code, Comput. Phys. Commun. 179 (2008) 777–783.

[164] Z. Piao, M. Bueno, L.D. Poulikakos, S. Hellweg, Life cycle assessment of rubberized semi-dense asphalt pavements; A hybrid comparative approach, Resour. Conserv. Recycl. 176 (2022) 105950.

[165] 12697-26, BSI Standards Publication Bituminous mixtures - Test methods - Part 26: Stiffness, Br. Stand. Institution, London, UK. (2018).

[166] G. Volume Graphics, VGStudio MAX 3.0. Reference Manual, 2016.

[167] Abramoff MD, Magalhaes PJ, Ram SJ (2004) Image processing with ImageJ. Biophotonics Int 11(7):36–42

[168] R. Ghabchi, D. Singh, M. Zaman, Laboratory evaluation of stiffness, low-temperature cracking, rutting, moisture damage, and fatigue performance of WMA mixes, Road Mater. Pavement Des. 16 (2015) 334–357.

[169] E. Coleri, J.T. Harvey, K. Yang, J.M. Boone, Investigation of asphalt concrete rutting mechanisms by X-ray computed tomography imaging and micromechanical finite element modeling, Mater. Struct. Constr. 46 (2013) 1027–1043.

[170] H.R. Radeef, N.A. Hassan, M.Z.H. Mahmud, A.R.Z. Abidin, R.P. Jaya, C.R. Ismail, H.F. Abbas, Linear viscoelastic response of semi-circular asphalt sample based on digital image correlation and XFEM, Meas. J. Int. Meas. Confed. 192 (2022).

[171] L. Gao, H. Kong, X. Deng, Z. Wang, Multi-scale finite element simulation of asphalt mixture anti-cracking performance, Theor. Appl. Fract. Mech. 121 (2022).

[172] D. Sanfilippo, A.G.Hernandez, A. Alexiadis, B. Ghiassi, Effect of freeze – thaw cycles on the void topologies and mechanical properties of asphalt, 344 (2022).

[173] N. Sukumar, D.L. Chopp, N. Moës, T. Belytschko, choles and inclusions by level sets in the extended finite-element method, Comput. Methods Appl. Mech. Eng. 190 (2001) 6183–6200.

[174] C. Jiang, G.F. Zhao, N. Khalili, On crack propagation in brittle material using the distinct lattice spring model, Int. J. Solids Struct. 118–119 (2017) 1339–1351.

[175] S.A. Silling, Reformulation of elasticity theory for discontinuities and long-range forces, J. Mech. Phys. Solids. 48 (2000) 175–209.

[176] J. Guo, W. Gao, Z. Liu, X. Yang, F. Li, Study of Dynamic Brittle Fracture of Composite Lamina Using a Bond-Based Peridynamic Lattice Model, Adv. Mater. Sci. Eng. 2019 (2019).

[177] S.A. Silling, M. Epton, O. Weckner, J. Xu, E. Askari, Peridynamic states and constitutive modeling, 2007.

[178] J. a. Mitchell, Non-Local, Ordinary-State-Based Viscoelasticity Model for Peridynamics, Sandia Rep. SAND2011-8 (2011) 28p.

[179] J.A. Mitchell, A Nonlocal , Ordinary , State-Based Plasticity Model for Peridynamics, Sandia Rep. (2011) 1–34.

[180] EN 12697-22. (2020). BSI Standards Publication - Bituminous mixtures - Test methods, Part 22: Wheel tracking.

[181] BSI Standards Publication Bituminous mixtures — Material specifications Part 5 : Stone Mastic Asphalt, BSI Br. Stand. (2016).

[182] R. Bandyopadhyaya, A. Das, S. Basu, Numerical simulation of mechanical behaviour of asphalt mix, Constr. Build. Mater. 22 (2008) 1051–1058.

[183] BS EN 12697-44-2010--[2021-10-25--06-49-03 PM].pdf, (n.d.).

[184] Abramoff MD, Magalhaes PJ, Ram SJ (2004) Image processing with ImageJ. Biophotonics Int 11(7):36–42

[185] G. Teng, C. Zheng, X. Chen, X. Lan, Y. Zhu, C. Shan, Numerical fracture investigation of single-edge notched asphalt concrete beam based on random heterogeneous FEM model, Constr. Build. Mater. 304 (2021) 124581.

[186] S. Plimpton, Fast Parallel Algorithms for Short-Range Molecular Dynamics, J Comp Phys, 117, 1-19 (1995).

[187] Parks, Lehoucq, Plimpton, Silling, Comp Phys Comm, 179(11), 777-783 (2008).

[188] A. Stukowski, Visualization and analysis of atomistic simulation data with OVITO – the Open Visualization Tool Modelling Simul. Mater. Sci. Eng. 18 (2010), 015012

[189] E. Mahmoud, E. Masad, S. Nazarian, Discrete Element Analysis of the Influences of Aggregate Properties and Internal Structure on Fracture in Asphalt Mixtures, J. Mater. Civ. Eng. 22 (2010) 10–20.

[190] S. Cui, B.R.K. Blackman, A.J. Kinloch, A.C. Taylor, Durability of asphalt mixtures: Effect of aggregate type and adhesion promoters, Int. J. Adhes. Adhes. 54 (2014) 100–111.

[191] E.J. Barbero, (Composite materials (CRC Press)) Barbero%2c Ever J.-Finite element analysis of composite materials using Abaqus (2013), 2013.

[192] A. Bekele, R. Balieu, D. Jelagin, N. Ryden, A. Gudmarsson, Micro-mechanical modelling of low temperature-induced micro-damage initiation in asphalt concrete based on cohesive zone model, Constr. Build. Mater. 286 (2021) 122971.

[193] G. Zeng, X. Yang, L. Chen, F. Bai, Damage Evolution and Crack Propagation in Semicircular Bending Asphalt Mixture Specimens, Acta Mech. Solida Sin. 29 (2016) 596–609.

[194] N.H.T. Nguyen, H.H. Bui, G.D. Nguyen, J. Kodikara, A cohesive damage-plasticity model for DEM and its application for numerical investigation of soft rock fracture properties, Int. J. Plast. 98 (2017) 175–196.

[195] X. Zhang, E. Chen, N. Li, L. Wang, C. Si, C. Wang, Micromechanical analysis of the rutting evolution of asphalt pavement under temperature – stress coupling based on the discrete element method, Constr. Build. Mater. 325 (2022) 126800.

[196] Ren, Y. Xu, J. Huang, Y. Wang, Z. Jia, Gradation optimization and strength mechanism of aggregate structure considering macroscopic and mesoscopic aggregate mechanical behaviour in porous asphalt mixture, Constr. Build. Mater. 300 (2021) 124262.

[197] M. Hadi Nahi, I. Kamaruddin, A. Ismail, R.A.-E. Al-Mansob, Finite Element Model for Rutting Prediction in Asphalt Mixes in Various Air Void Contents, J. Appl. Sci. 14 (2014) 2730–2737.

[198] E. Coleri, J.T. Harvey, K. Yang, J.M. Boone, A micromechanical approach to investigate asphalt concrete rutting mechanisms, Constr. Build. Mater. 30 (2012) 36–49.

[199] H. Liang, L. Shi, D. Wang, X. Xiao, K. Deng, Influence of graded coarse aggregate content and specific surface area on the fracture properties of asphalt mixtures based on discrete element simulations and indoor tests, Constr. Build. Mater. 299 (2021) 123942.

[200] G. Yuan, X. Li, P. Hao, D. Li, J. Pan, A. Li, Application of flat-joint contact model for uniaxial compression simulation of large stone porous asphalt Mixes, Constr. Build. Mater. 238 (2020) 117695.

[201] D.X. Lu, N.H.T. Nguyen, H.H. Bui, Highlights :, Int. J. Plast. (2022) 103391.

[202] J. Zhang, J. Zhang, D. Cao, Genetic algorithm optimization for cohesive zone modeling of viscoelastic asphalt mixture fracture based on SCB test, Eng. Fract. Mech. 271 (2022) 108663.